7-2015

Engineering the Ground State of Complex Oxides

Derek Joseph Meyers
University of Arkansas, Fayetteville

Engineering the Ground State of Complex Oxides

A dissertation submitted in partial fulfillment
of the requirements for the degree of
Doctor of Philosophy in Physics

By

Derek Joseph Meyers
Michigan Technological University
Bachelor of Science in Physics, 2009
University of Arkansas
Master of Science in Physics, 2012

July 2015
University of Arkansas

This dissertation is approved for recommendation to the Graduate Council

Prof. Jak Chakhalian
Dissertation Director:

Prof. Huaxiang Fu
Committee member

Prof. Douglas Spearot
Committee member

Prof. William Oliver III
Committee member

Abstract

Transition metal oxides featuring strong electron-electron interactions have been at the forefront of condensed matter physics research in the past few decades due to the myriad of novel and exciting phases derived from their competing interactions. Beyond their numerous intriguing properties displayed in the bulk they have also shown to be quite susceptible to externally applied perturbation in various forms. The dominant theme of this work is the exploration of three emerging methods for engineering the ground states of these materials to access both their applicability and their deficiencies.

The first of the three methods involves a relatively new set of compounds which adhere to a unique paradigm in chemical doping, a-site ordered perovskites. These compounds are iso-structural, i.e. constant symmetry, despite changing the dopant ions. We find that these materials, featuring Cu at the doped A-site, display the Zhang-Rice state, to varying degrees, found in high temperature superconducting cuprates, with the choice of B-site allowing "self-doping" within the material. Further, we find that within $CaCu_3Ir_4O_{12}$ the Cu gains a localized magnetic moment and leads to the experimentally observed heavy fermion state in the materials, one of only two such non-f-electron heavy fermion materials.

Next, epitaxial constraint is used to modify the ground state of the rare-earth nickelates in ultra thin film form. Application of compressive (tensile) strain is found to suppress (maintain) the temperature at which the material goes through a Mott metal-insulator transition. Further, while for $EuNiO_3$ thin films the typical bulk-like magnetic and charge ordering is found to occur, epitaxial strain is found to suppress the charge ordering in $NdNiO_3$ thin films due to pinning to the substrate and the relatively weak tendency to monoclinically distort.

Finally, the creation of superlattices of $EuNiO_3$ and $LaNiO_3$ was shown to not only allow the selection of the temperature at which the metal-insulator transition occurs, but through digital control the Ni site symmetry can be artificially broken leading to a previously unseen monoclinic metallic phase. Further, by creating a structure which does or does not match the bulk-like rock salt charge order pattern it was found this transition can be either strongly enhanced or removed entirely.

ACKNOWLEDGEMENTS

I begin by acknowledging my colleagues in the Laboratory for Artificial Quantum Materials at the University of Arkansas for all their support and guidance over the past several years. My senior fellow graduate students, Jian Liu and Benjamin Gray, trained and supported me throughout my early career, and I am eternally grateful for their assistance and I continue to seek their advice and counsel in my endeavors. As their guidance and experience significantly influenced my successes in my graduate career, I was honored to provide the same for Xiaoran Liu. Xiaoran's work ethic and unerring focus make him an asset to our laboratory and I look forward to his contributions to the community. I would also like to acknowledge the post doctoral researchers I have worked with in our laboratory. Yanwei Cao and Eun Ju Moon both helped guide me and were exceptional people to work alongside. Srimanta Middey and I worked together very closely during our time together and his experience and knowledge were always helpful. Much of my work at the Laboratory for Artificial Quantum Materials was assisted greatly by him and his input will be sorely missed. Finally, Misha Kareev has been a constant source of support in our laboratory, with his boundless knowledge of all of the equipment and the synthesis of all the materials contained within this thesis, his support has truly been without measure.

I would also like to thank the Doctoral Academy for their financial support during my time at the University of Arkansas.

X-ray techniques requiring national synchrotron facilities permeate this entire thesis. I gratefully acknowledge the support and guidance provided to me by these groups and their facilities. I would like to specifically acknowledge John Freeland, Phil Ryan, Daniel Haskel, Yongseong Choi, Jong-Woo Kim, and Padraic Shafer for their collaborations which directly lead to the contents of this thesis.

I also thank my family for their love, support, and encouragement to pursue my passion for science. For her love and support, I would also like to thank Kimberly Zoldak.

Finally, I would like to provide my sincerest thanks to my advisor, Jak Chakhalian. He has provided the guidance, motivation, and drive that brought me to this point in my career. Jak could always be counted on to support my endeavors and his enthusiasm for disentangling the underlying physics in complex materials will always inspire me.

TABLE OF CONTENTS

LIST OF FIGURES

LIST OF TABLES

1 Introduction

In this chapter the basic structural and electronic physics of transition metal oxides will be introduced in a broad scope. A brief overview of the specific materials investigated in this thesis will be given, and methods for engineering their properties, which form the central theme of this thesis, will be explored.

1.1 Transition Metal Oxides: Perovskites

Transition metal oxides (TMOs) encompass a vast array of materials, structurally and chemically, which display intriguing physical phenomena. Several areas of research have sprung up in the past several decades dedicated specifically to exploring an unusual property discovered in TMOs, such as high temperature superconductivity, colossal magneto-resistance, ferroelectricity, multi-ferroics, and myriad other exciting phases. Many of the exciting physics can be traced back to structural effects, a result of TMO's extensive ability to span numerous structural motifs that lead to anomalous coordinations and interactions. An exhaustive overview of transition metal oxides can be found here[1], and an in depth overview of the underlying physical mechanisms leading to the anomalous behaviors can be found in Ref. [2, 15].

1.1.1 Crystal Structure

Numerous unique structures belong to the TMO family, spanning all seven lattice systems. While numerous phenomena of significant general interest also span these different structures, an exhaustive overview is beyond the scope of this thesis, and has been covered elsewhere[1]. Within this thesis, only the perovskite structure will be encountered and thus the following discussion will be limited to this crystal type.

Perovskite was the original name for the mineral form of calcium titanate, with chemical structure $Ca^{2+}Ti^{4+}O_3^{2-}$, named after the Russian mineralogist Lev Perovski. The unit cell for this crystal contains O anions at the faces, Ca at the corners, and a Ti cation at the center, and in general can be written as ABO_3, Fig. 1.1(a). These materials consist of hexagonally close packed (HCP) planes in the (111) direction, with alternating AO_3 and B layers. The structural bonding is mostly ionic, with the metal-oxygen bonding providing a

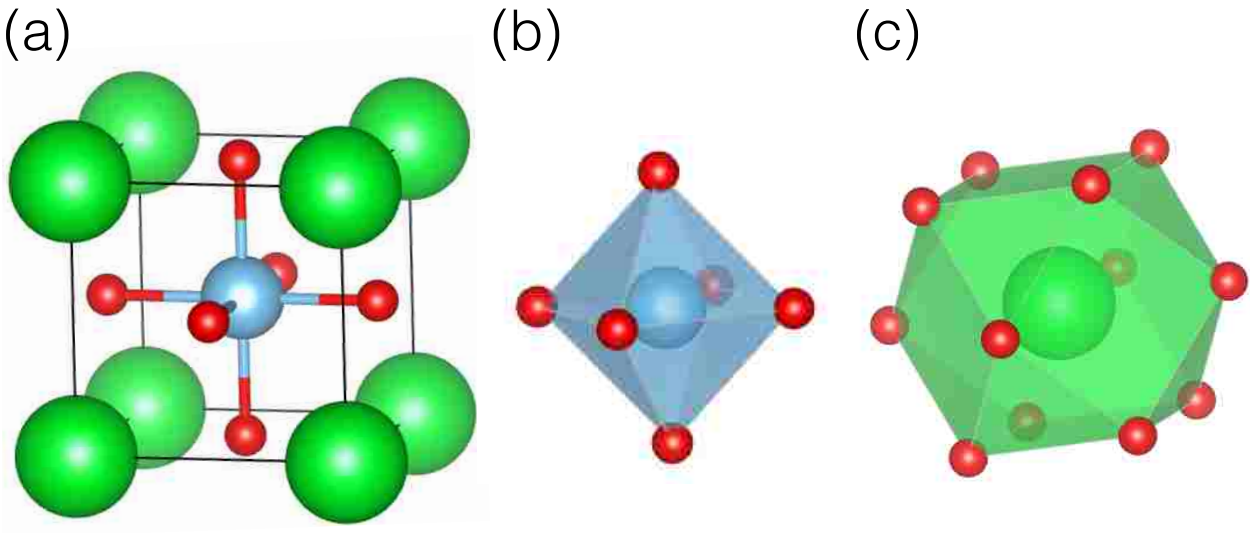

Figure 1.1: (a) Ideal ABO_3 structure, A-site B-site, and O are represented by green, blue, and red spheres respectively. (b) BO_6 octahedra. (c) AO_{12} polyhedra.

stable framework. Cohesive energy of a crystal in the simple ionic picture can be quantitively understood as point charges at lattice sites interacting by the Coulomb electro-static interaction. However, due to the Coulomb interaction being a long range force, the summation of the different ion-ion interactions can be a conditionally convergent series, thus special care must be taken. Typically, the interaction is written in terms of the Madelung energy, the largest contribution to the cohesive energy, for the electrostatic potential at the as in eq 1.1.

$$E_i^{Madelung} = -\sigma \frac{e^2 Q_i}{4\pi\epsilon_0 r_0} \tag{1.1}$$

where σ is known as Modeling constant and r_0 is the nearest neighbor distance. This is the electrostatic energy felt at the lattice site i with charge eQ_i; the Madelung constant for this site can be written as $\sigma = \sum_j \frac{Q_j * r_0}{r_{i,j}}$, where $r_{i,j}$ is the distance between the i^{th} site and the arbitrary j^{th} site. Thus, the Madelung constant renormalizes the equation to the nearest neighbor distance and the charges at all the sites. From this formalism, it is obvious the coordination geometry is very important to the ionic potential, which in the perovskite structure gives a 6-fold O coordination for the B-site and for the A-site a 12-fold O coordination, Fig. 1.1(b) and (c). This gives an octahedral oxygen geometry around the B-site, which connects with neighboring octahedra via corners. Within the ionic approximation, the coordination and the valence of the constituent elements have a

strong effect on the ionic radii and thus the structure. Further, covalency between $B-O$ tends to shorten the bond lengths which can further complicate the simpler ionic picture, especially in the charge-transfer insulators, where this covalency can be quite strong. Finally, distortions to the coordination geometry, such as the Jahn-Teller effect, can cause further deviations from a simple, ionic picture. Thus, finding the true structure of these materials is an experimental imperative before any meaningful conclusions can be drawn.

Interestingly, within the perovskites, the distortion of the general ABO_3, partially caused by these non-ionic contributions, structure away from ideal cubic, where the lattice constants and angles are inter-related by $a = b = c$ and $\alpha = \beta = \gamma = 90°$ respectively, can be conveniently indexed by the Goldschmidt tolerance factor[19], eq. 1.2.

$$t = \frac{r_A + r_O}{\sqrt{2}(r_B + r_O)} \tag{1.2}$$

where r_A, r_B, and r_O are the ionic radii of the A-site, B-site, and O-site respectively, though it should be noted the anion is not necessarily oxygen, but will be throughout this thesis. Typically this number allows us to roughly predict the crystal system of a perovskite, as shown in table 1.1[18]. In an ideal perovskite system, such as $SrTiO_3$, the symmetry group is $Pm\bar{3}m$ within the cubic crystal system. The 90° angles between each axis give a 180° $B-O-B$ bond angle, which puts the O directly in-between the two cations, and gives the highest possible $B-A$ cation seperation as well, forming a very stable structure. If the A-site size decreases, or B-site size increases, t decreases and A-site is no longer able to fill all of the space required to form the ideal cubic structure. When this happens the structure distorts to fill in the empty space, by rotating the octahedra which decreases the lattice size and the $B-O-B$ bond angle. Symmetry relations are also forfeited by this distortion of the structure, and the space group (crystal system) will change accordingly, typically first to $R\bar{3}C$ (Rhombohedral), then $Pbnm$ (Orthorhombic), then $P2_1/n$ (monoclinic). One of

Table 1.1: Tolerance factor and crystal system

Tolerance factor	Relative sizes	Crystal systems	Examples
$t > 1$	Large A or small B	Hexagonal	$BaNiO_3$ [16]
$\sim 0.9 < t < 1$	A and B ideal ratio	Cubic	$SrTiO_3$ [16]
$\sim 0.71 < t < 0.9$	A small	Rhombohedral - monoclinic	$LaNiO_3$, $NdNiO_3$ [17]
$t < 0.71$	$A \simeq B$	Varying, cation disorders	Corundum, Ilmenite, etc[18]

the myriad of effects of these changes is the reduction in structural stability as the cation - cation interactions are now stronger. This effect will be discussed in more detail in section 1.3.1 in relation to the rare earth nickelates. Finally, when $r_A \simeq r_B$ the structure can deviate entirely from perovskite, allowing corner-sharing octahedra to give way to edge or face sharing octahedra, changes in B-site oxygen coordination, i.e. tetrahedra. While these changes are significant, for a series of ABO_3 containing the same B-site anion and various A-sites typically spanning the Lanthanide group of the periodic table, t can remain relatively large thus giving a series of perovskites with subtly different structural parameters, yet stunningly different physical properties. Such effects point to not only the remarkable ability of the perovskite structure to incorporate different ions into the same structural motif, but also the significance of the crystal structure to the physical properties.

1.1.2 Electronic Properties

As previously discussed, even slight changes to perovskite structure can have drastic effects on the physical properties, and thus a thorough understanding of the underlying electronic phenomena associated with these distortions is in order. First, however, a general overview of the electronic structure of the perovskites is necessary to lay the framework for the forthcoming discussion in section 1.2.

Starting with a simple ionic view, we use MgO as a model system. When each component is considered as a free ion, we get the picture of Fig. 1.2(a). As discussed in the previous section, each of these ions will be subjected to an electrostatic Madelung potential when placed within the crystal lattice, forcing the O^{2-} states lower in energy and the Mg^{2+} states are pulled upward. Further, the polarizability of the medium will act to reduce the binding energies of the electrons, as in Fig. 1.2(c). Finally, hybridization between neighboring ion orbitals leads to a broadening of the states 1.2(d). However, this model's treatment of all orbitals as degenerate disregards important phenomena that occurs within the perovskites and thus further interactions must be included.

In simple atomic physics the energy for electrons is found using only the principle quantum number, n. Thus, in TMOs from the third row of the periodic table (i.e. Ti, Ni, etc) the energy of an electron in any of the $n = 3$ states is the same, there are $2+6+10 = 18$ (3s, 3p, or 3d) possible electron states which would imply a band with 18 electrons. Spin-orbit coupling reduces this by splitting the s, p, and d orbitals into separate bands, but for the $3d$

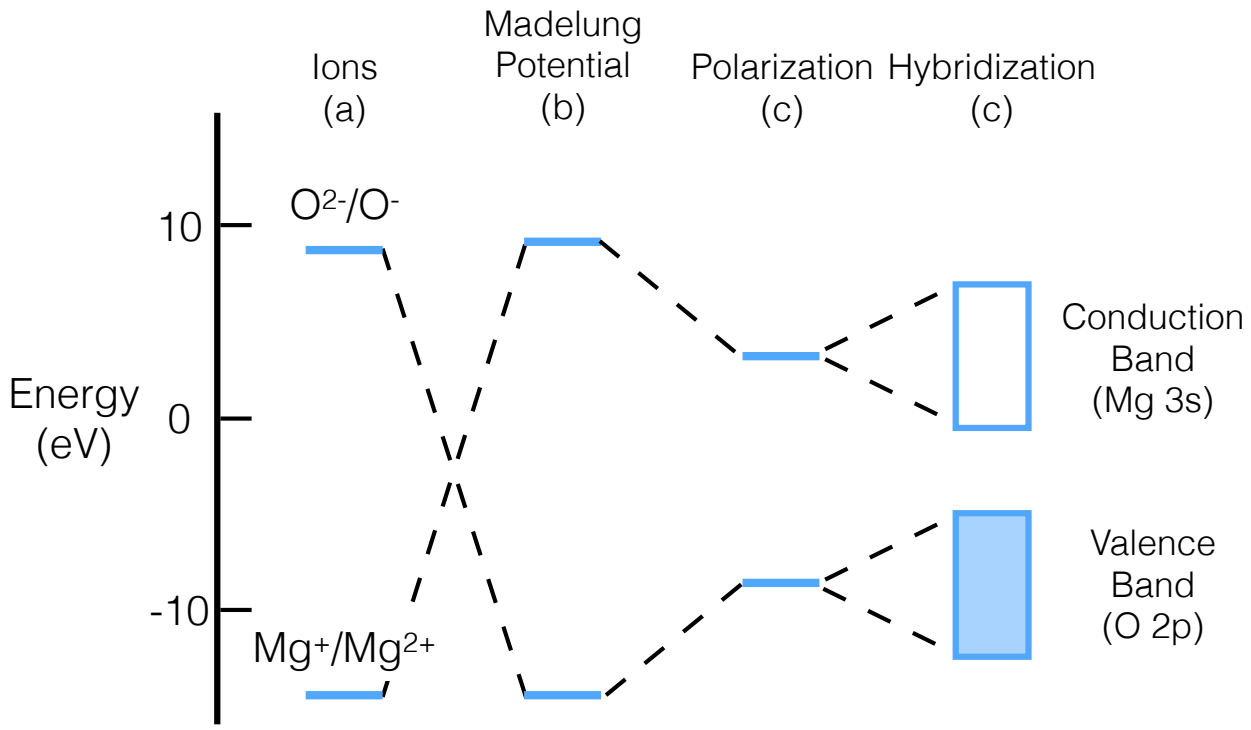

Figure 1.2: MgO ionic model, with (a) free ions (b) placed in the Madelung potential of the crystal lattice (c) polarization of the medium (d) broadening of the electric states due to hybridization. The filled in area represents occupied states. Figure adapted from Ref. [1]

band, which is typically the valence band in TMOs, there are still 10 degenerate states. The further breaking of the degeneracy requires attention to the crystal structure, implying that the splitting must be considered for each crystal structure. For perovskites the coordination of the B-site is always octahedral with O-sites, allowing a general description to be utilized.

Starting with 10 degenerate d-electron states, there will be 5 available orbitals corresponding to $m_l = \pm 2, \pm 1, 0$. These orbitals are denoted as $d_{z^2-r^2}$, $d_{x^2-y^2}$, d_{xy}, d_{xz}, and d_{yz}, as shown in Fig. 1.3(a). As previously discussed, the O anions form an octahedra around the B-site, and are in the O^{2-} valence state, $2p^6$. with orbitals lying along the x, y, and z axes. For the d-orbitals, only the d_{z^2} and $d_{x^2-y^2}$ orbitals lie along a principal axis, with the other three orbital's lobes lying at 45° angles to the axes. Thus, due to the Coulomb repulsion between the d and p electron orbitals, the d_{z^2} and $d_{x^2-y^2}$ orbitals, collectively referred to as the e_g band, will be at higher energy then the d_{xy}, d_{xz}, and d_{yz} orbitals, denoted as the t_{2g} band. This is known as crystal field (CF) splitting, with $E_{gap} \equiv \Delta_{CF}$ or $10Dq$, Fig. 1.3(b).

Electron filling of the d-orbitals is also directly effected by CF. In the 10-fold degen-

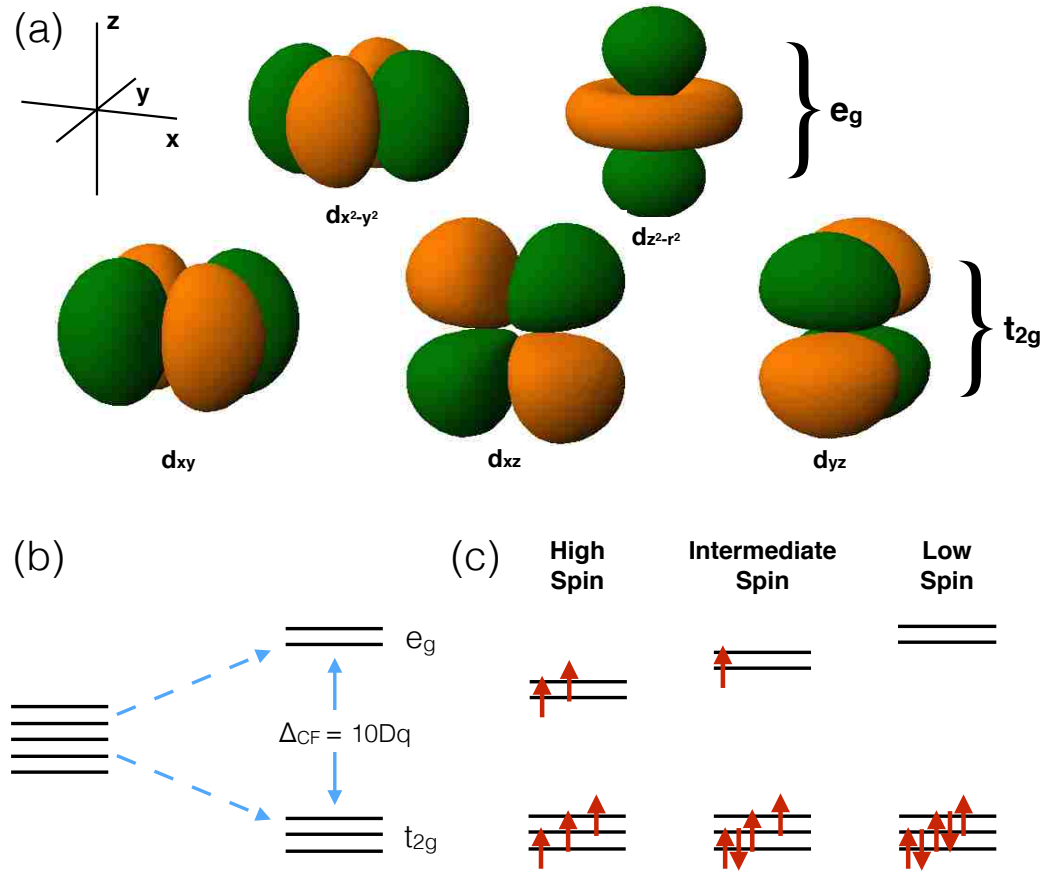

Figure 1.3: (a) The five 3*d*-orbitals. The two orbitals with lobes directed along principal axes are referred to as the e_g orbitals, and the remaining three with lobes in between the axes as t_{2g} orbitals. (b) Crystal field splitting of the d energy levels due to the repulsion of the O-p and the TM-d orbitals. (c) Three different possible fillings for the d^5 state depending on the relative strength of the Δ_{CF} and J_H.

erate case, the filling of electrons into the orbitals follows the Hund's rules: the electrons will fill to have (1) maximum total S, (2) maximum total L, (3) maximum J for less then half-filled, minimum J for more then half-filled. Thus, if the d-orbital is half-filled (5 electrons) each orbital would have exactly one electron (maximum S). However, e_g and t_{2g} bands with splitting Δ_{CF} do not always follow this rule, and can take on either high, low, or intermediate spin states depending on the value of Δ_{CF} compared to what is known as the Hund's rule coupling J_H, Fig. 1.3(c). The high spin state, for which $J_H > \Delta_{CF}$, the electron follows the Hund's rule with $S = 5/2$. However, when $J_H < \Delta_{CF}$, the five electrons will all lie within the t_{2g} band violating Hund's first rule, with $S = 1/2$. In the case where $J_H \simeq \Delta_{CF}$, an intermediate state can be obtained where four electrons occupy the t_{2g} with one in the e_g

band. Another important result occurs for filled t_{2g} with a partially filled e_g band. Both d_{z^2} and $d_{x^2-y^2}$ orbitals have an expectation value for m_l of 0, giving $L = 0$, thus $J = S$ which means the spin-orbit coupling $L \cdot S$ is quenched for e_g orbitals, a result which is important for the later TMOs.

While the CF splitting does lift the five-fold degeneracy, it does not lead to a totally non-degenerate ground state. In this regard, a theorem from 1937, which argued the only degeneracy allowed in the ground state is the spin degeneracy, called the Jahn-Teller theorem, describes how the system is able to further break the degeneracy[20]. In the case described so far, we have considered a crystal with all six B-site to O bonds being the same length. If, for example, the $B-O$ distance in the z-direction is greater than the $B-O$ distance in the x or y directions, then the d_{z^2} will interact less with the $O-p$ orbital, and the energy of this state will be lower than the $d_{x^2-y^2}$ orbital, and the e_g band is no longer degenerate. Likewise, the d_{xz} and d_{yz} orbitals will be lower in energy than the d_{xy} orbital, splitting the t_{2g} orbital, Fig. 1.9(a). This is the simple case of a tetragonal distortion, which occurs, for example, for Mn^{3+} (d^4) octahedra, but there are multiple possible distortions and combinations of distortions that can occur to break the degeneracy of the e_g and t_{2g} bands. Ions which display this type of behavior are referred to as Jahn-Teller active, and occur quite often for odd d-filling. The energetics of this are quite important, as any deformation of the octahedra, and hence the lattice, costs an energy $\frac{1}{2}Bu^2$, where B is the bulk modulus, and u is the distortion. Similarly the splitting of the energy levels caused by the distortion are linear in u, with a coupling constant g, thus we arrive at eq. 1.3:

$$E_{JT} = \pm gu + \frac{1}{2}Bu^2 \tag{1.3}$$

which, when minimized for E_{JT}, gives $u = \pm\frac{g}{B}$, and $E_{JT} = -\frac{g^2}{2B}$. Thus, distortions of the crystal are able to break the degeneracy and give a lower energy state. It should be noted that not all crystals break the degeneracy this way. In the particular case of Ni^{3+}, which was expected to be a strong Jahn-Teller active ion due to it's low spin d^7 state (one e_g electron), no such distortions were found for several of these materials. This atypical case will be discussed in section 1.4, and a significant portion of this thesis pertains to the mechanism found to break the degeneracy therein.

Finally, consideration must be made to the finite amount of orbital hybridization, or covalent bonding, that occurs in TMO perovskites. For $3d$ orbitals, which lie very close to the core levels spatially, this correction to the ionic approximation is very small, but the

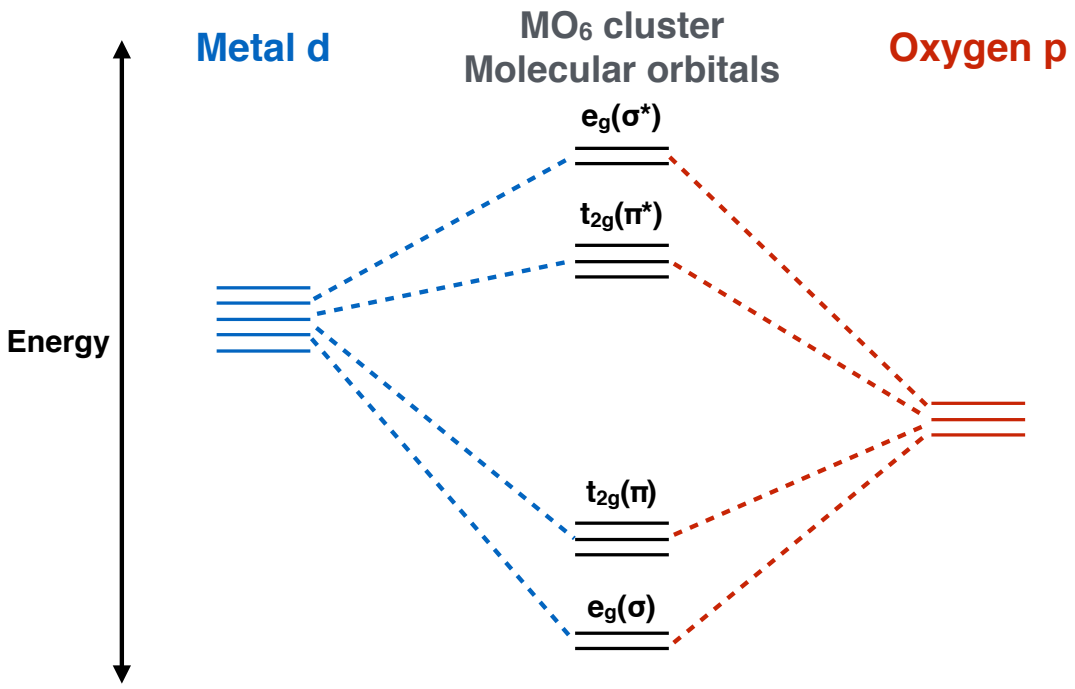

Figure 1.4: Formation of molecular orbitals from linear combinations of the atomic $3d$ and $2p$ states in an MO_6 octahedra. Figure adapted from Ref. [1].

$O-p$ orbitals are more extended and thus some hybridization does occur. Hybridization can be treated by the molecular orbital (MO) description, which utilizes linear combination of atomic orbitals, or LCAO. In this method, molecular orbitals are considered as linear combinations of the ionic atomic orbitals, or $\Psi = \sum_i c_i \psi_i$. Energy eigenvalues, ϵ and the coefficients are found by solving the secular equations, $Hc = \epsilon Sc$, where H is the Hamiltonian and S is the overlap matrix in the basis of the atomic orbitals with c_i weight. Then the MO orbitals can be written as shown in Fig. 1.4, adapted from reference[1]. The bonding can be grouped into σ-type, where the two atomic orbitals have lobes directed towards each other, and π-type where the lobes are perpendicularly oriented. Thus, utilizing our previous discussion, the e_g orbitals form σ bonds, and the t_{2g} orbitals form π bonds. Bonding and anti-bonding states, anti-bonding being indicated by $*$ in Fig. 1.4, are formed which split the energy as shown. The bonding states contain a much stronger $2p$ character due to the higher spatial extent of p orbitals, while the anti-bonding orbitals have more $3d$ character due to their more localized nature. As a perturbation, this MO splitting thus has the same, though smaller, effect as CF splitting, and is usually considered as an enhancement to Δ_{CF}. The main consideration of MO LCAO, however, is the lowering of the energy of the bonding

states with mostly p character, and the increase of the energy of the bands with d character. These bands are much more localized at the atomic sites giving small bandwidth, and thus small hopping t, due to their small spatial overlap and metal-metal hopping occurring via the hybridized orbitals with O. Typically, these higher energy orbitals make up the valence and conduction bands of the crystal. This lays the basis for our understanding of the orbitals in perovskites, but has not yet addressed the important point of the electronic behavior of these systems.

Electron movement within solids has been a focus of experimental and theoretical research for over a century. The first milestone in this understanding was put forth in 1940 by Felix Bloch[21]. In this view, the periodic arrangement of atoms creates a periodic potential well, with lowest energy at the positively charged atomic centers; the electrons are seen as totally non-interacting in this viewpoint. Each electron orbital within the atom can hold two electrons, by the Pauli principle, and with N atoms this means we can consider a band with $k_n = \frac{2\pi n}{N}$ allowed states, where $n = -\frac{1}{2}N, ..., \frac{1}{2}N$. Each band is separated from another by some energy, which follows from the preceding discussion. In this picture, metallic versus insulating behavior is quite straightforward to understand. If we have exactly $2N$ electrons in the highest occupied band, there are no empty states in this band and any electron moving through the system would have to go to the lowest unoccupied band, which is at some energy, E_{gap} above the occupied level, leading to insulating behavior. Then in order to drive electrons through the system E_{gap} must be supplied. Further, at higher temperatures, where the thermal energies of the electrons are high, the energy required to drive the electrons becomes less. This can be easily seen in transport measurements, where insulators show a characteristic increase in resistance as the temperature is lowered.

In the case where there are $<$ then $2N$ electrons, the situation is quite different. The electrons are now free to move between sites, as the unoccupied and occupied states have the same energy, thus there is no energy gap to overcome, and the material is metallic. Despite the relative simplicity of this model, it has been shown to be quite powerful since its inception and can explain the behavior of many solid state systems quite satisfactorily. However, this theory relies on the assumption of ionic centers with no overlap of wave functions between the atoms severely limiting its utility, as from the preceding discussion it is obvious such hybridization cannot be ignored.

A common correction to compensate for the non-zero overlap of atomic orbitals is known as the tight-binding approximation or LCAO approximation. Here, tunneling of

the electrons between two neighboring sites is allowed, which causes the band to split into bonding and anti-bonding configurations, which then form broadened bands throughout the crystal, as discussed previously. At large atomic separations the overlap goes to zero and simple band theory is again applicable.

While, as stated, band theory can be a very powerful technique, the underlying assumption of no electron-electron interactions is often incorrect. For s and p metals the band picture combined with the tight-binding approximation can be sufficient owing to their large bandwidth. However, for orbitals with smaller bandwidth, d and f bands, the interaction between valence electrons can be quite large.

To account for the electron-electron interactions, the hamiltonian for electrons in a solid must be modified. In the simple band picture, we can write the Hamiltonian of an electron hopping between sites as eq. 1.4, known as the Hubbard Hamiltonian.

$$H = -t \sum_{(i,j),\sigma} c^{\dagger}_{i\sigma} c_{j\sigma} \tag{1.4}$$

where t is the hopping matrix element between states i and j, σ is the spin, $c_{k\sigma}$ and $c^{\dagger}_{k\sigma}$ are the annihilation and creation operators respectively. Where a Fourier transform to k-space will give $H_{Band} = \sum_{(k,\sigma)} \epsilon(k) c^{\dagger}_{k\sigma} c_{k\sigma}$, where $\epsilon(k)$ is the band spectrum. Interestingly, eq. 1.3 has no dependence on the distance between the ions. Thus, as long as the uppermost occupied band is not fully occupied, $2N$ electrons, then the system will be metallic with hopping t. With large interatomic distances this is not a reasonable picture, but the inclusion of electron-electron interaction rectifies the situation. If we quantify the Coulomb repulsion between two electrons on the same site as U and then the total hamiltonian is written as eq. 1.4.

$$H = -t \sum_{(i,j),\sigma} c^{\dagger}_{i\sigma} c_{j\sigma} + U \sum_{i} n_{i\uparrow} n_{i\downarrow} \tag{1.5}$$

where $n_{i\uparrow}$ and $n_{i\downarrow}$ are the up and down spin electron densities. Thus if each site has one electron in the highest occupied band, it will cost an energy U to move the electron from site j to site i or in terms of an excitation, $d^n \rightarrow d^{n+1}$ costs energy U. This seemingly very simple equation is known as the Hubbard model, and it is very important to understanding the physics of d and f electrons.

This overview is obviously oversimplified, as in real crystals there will be multiple available states to jump to, $t_{i,j}$, and each orbital within an atom has it's own U value, which,

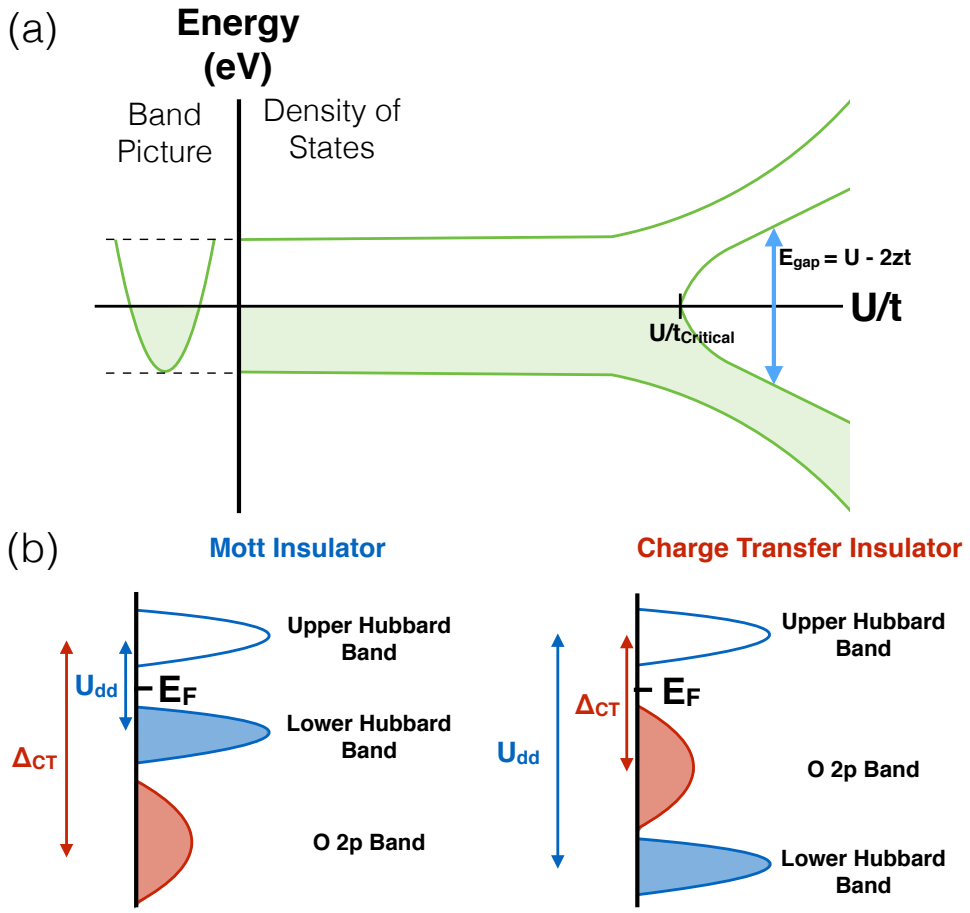

Figure 1.5: (a) Left: Half filling in band theory, giving a metallic state. Right: Density of states, with $U \ll 2zt$ at left. As U increases the band eventually splits at $U_{Critical}$, opening an insulating gap, E_{gap}. Adapted from Khomskii[2]. (b) Left: Mott insulating state, lowest lying excitation is from occupied d states to the unoccupied d states. Right: Charge transfer insulating state, lowest lying excitation is from occupied $2p$ states to the unoccupied d states.

in TMO perovskites, usually gives U_d and U_p for the TMO ion and O respectively. However, some basic cases can be explored. In the case where the filling of the band goes to $2N$ or 0, the state is fully occupied or empty, a Bloch-Wilson band insulator is obtained. However, the system is no longer always a metal when the valence band is not entirely filled. Instead $E_{gap} \sim U - 2zt$, where z is the number of nearest neighbors and t is the hopping matrix element, $2zt$ is the bandwidth.Thus, when $U < 2zt$ the system is a metal, and when U is greater, an insulator is formed. This is known as a Mott insulator, and as shown, is due to the strong electron-electron correlations which band theory ignores. As mentioned, while for band theory unrealistic interatomic distances can still give a metallic state, in the Hubbard model the reduction of the hopping integral t will eventually give $U > 2zt$ and bring the

system to an insulating state, often times even with realistic lattice sizes. If we consider a fixed lattice, $U = 0$ and some fixed t with one valence electron, the picture is simply the same as in band theory. The effect of then increasing U/t is shown by Fig. 1.5(a), adapted from [2]. Initially, the effect is to simply slightly widen the band. However, when $U/2zt \simeq 1$, the band is split. As U/t is further increased the splitting between these bands becomes $E_{gap} \simeq U - 2zt$ and an insulating state is obtained after some critical value U/t. The unoccupied and occupied bands are then referred to as the *upper* (UHB) and *lower* (LHB) Hubbard bands respectively, and the system has undergone a so-called Mott metal-insulator transition (MIT). The above case is referred to this as a bandwidth controlled MIT, as typically the bandwidth t is changed by manipulating the lattice, and thus the interatomic distance. If the system sits in the Mott insulating state at half-filling, as in Fig. 1.5(a) with $U/t > U/t_{Critical}$, a metallic state can also be obtained by electron or hole doping. In the case of electron doping, the added electrons must go to the upper Hubbard band, and thus do not suffer the U energy penalty. Likewise, when holes are doped the electrons in the lower Hubbard band can then hop to the hole sites at the same energy and an itinerant state is again obtained.

An important consideration to this model, which follows from the preceding discussion involving the hybridization of atomic orbitals, is how the inclusion of hopping between the B-site and O alters the model. It is, in fact, quite important for TMOs with more then half-filled d-shells, where the O $2p$ states can be close to the Fermi level. Including all the possible hopping matrixes and Hubbard U values gives a far more complicated model, which the interested reader can find in Ref. [2]. In this model, excitations can take the form, $d^n p^m + d^n p^m \rightarrow d^{n+1} p^m + d^{n-1} p^m$ or $d^n p^m \rightarrow d^{n+1} p^{m-1} \equiv d^{n+1}\underline{L}$, where $\underline{\text{L}}$ denotes a ligand hole. There are then two possible excitations, an electron hopping from $d - d$ or from $p - d$ bands. The energies associated with each transition are U_{dd} and Δ_{CT}, with $\Delta_{CT} = \epsilon_d - \epsilon_p$ for transitions to an empty d-band and $\Delta_{CT} = (\epsilon_d + U_{dd}) - \epsilon_p$ for a half filled d-band. Schematically this can be qualitatively understood as in Fig. 1.5(b). If the $O - p$ band lies between the *upper* and *lower* Hubbard band, the lowest energy excitation is to transfer an electron from the $O - p$ band into the *upper* Hubbard band. In this situation the material is referred to as a charge-transfer (CT) insulator. In the case where the p band lies below the d bands, a typical Mott insulator is observed. These findings are summarized well by the Zaanen-Sawatzky-Allen phase diagram, Fig. 1.6[3]. The Mott insulating regime occurs for $\Delta_{CT}/t > U_{dd}/t > 1$. Keeping Δ_{CT} constant, when $U_{dd}/t \simeq 1$ a transition occurs

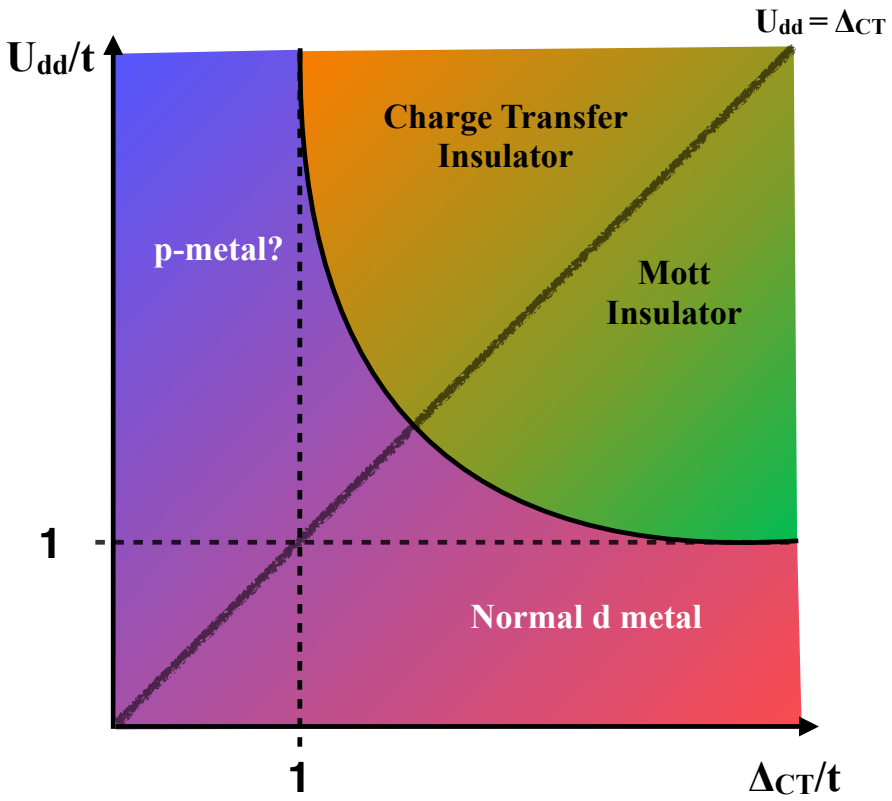

Figure 1.6: Sawatzkl - Allen - Zaneen phase diagram adapted from Ref. [3]. Left Panel: Half filling in band theory, giving a metallic state. Right panel: Density of states, with $U \ll 2zt$ at left. As U increases the band eventually splits at $U_{Critical}$, opening an insulating gap, E_{gap}.

to a typical d metal state, where the bandwidth overcomes the electron-electron repulsion. Likewise, if $U_{dd}/t > \Delta_{CT}/t > 1$ a charge transfer insulator is obtained. However, if we now hold U_{dd} constant, and reduce Δ_{CT} we eventually end up in a regime with strong $d-d$ electron correlations, but small Δ_{CT}/t which can be thought of as a p-metal on O bands with strongly localized $d-electrons$, which could give heavy fermion behavior similar to f-electron systems, or an anomalous insulating state such as Kondo insulators[2]. Typically, TMOs showing CT behavior have a higher d filling, Ni^{3+} (d^7) and Cu^{2+} (d^9), while lower d filling, such as Ti^{3+} (d^0), are Mott insulators. The source of this behavior is the larger atomic charge, or Z, in the heavier TMOs which raises the binding energy of the d states, lowering them closer to the static p states. Similarly, when increasing oxidation state for a particular ion, or lowering the d filling, U_{dd} will decrease, as there are fewer d-electrons to interact with. When Δ_{CT} becomes quite small compared with the p and d bandwidth the

hybridization strongly increases and the ionic model of $O-2p^6$ configuration is no longer valid. Typically in this case an electron is partially transferred to the $M-d$ band from the $O-p$ band and the ground state is some mixture of the $d^n p^6$ and $d^{n+1}p^5$ or $d^{n+1}\underline{L}$ state.

1.2 A-site ordered perovskites: Ordered doping

The typical perovskite structure discussed so far covers an enormous field of research and encompasses numerous physical properties, some unique to these systems. An enormous amount of work has gone into studying the basic ABO_3 materials, and numerous variants exist that further push the boundaries of physical phenomena. A relatively new variant, originally synthesized in 1967 by Deschanvres *et al*, the A-site ordered perovskites (AOPs) take the chemical formula $AA'_3B_4O_{12}$, or $(A_{1/4}A'_{3/4})BO_3$[22]. Relatively little work was undertaken until the discovery of an enormous dielectric constant in $CaCu_3Ti_4O_{12}$ by Subramanian *et al* in 2000[23]. Following this development, the these materials have displayed numerous exciting phases and properties that show promise for future work[24, 25, 26].

1.2.1 Crystal Structure

Doping of the A-site is an extensively utilized tool in the TMOs that can thoroughly modulate the available phase space for a material, with CMR manganite $La_xCa_{(1-x)}MnO_3$ as a prime example. Varying x from one to zero encompasses ferromagnetic metallic and insulating states, an antiferromagnetic charge ordered state, and canted anti ferromagnetism[27]. However, careful attention must be given to how the doping effects change the crystal structurally. Phonon modes can be activated due to symmetry lowering that can lead to the observed physical property modulation. More worryingly, defect density can dramatically rise which can be very difficult to quantify and compensate for when analyzing property changes. Finally, non-uniformity in doping can be a serious problem and can also be difficult to detect and understand.

Alleviating these issues, ordered A-site doping introduced a new paradigm in doping where the relative amount of A and A' are fixed and the A, A', or B-site ions can all be varied. Limitations, as with any doping regime, exist, such as the relatively limited dopants available, as in the case where B is chosen to be Mn. The $La_xCa_{(1-x)}MnO_3$ series has been heavily studied and very precise control of the amount of dopant ion can be done, giving a very detailed phase space. With $B = Mn$ in the AOPs, different A and A' sites may be

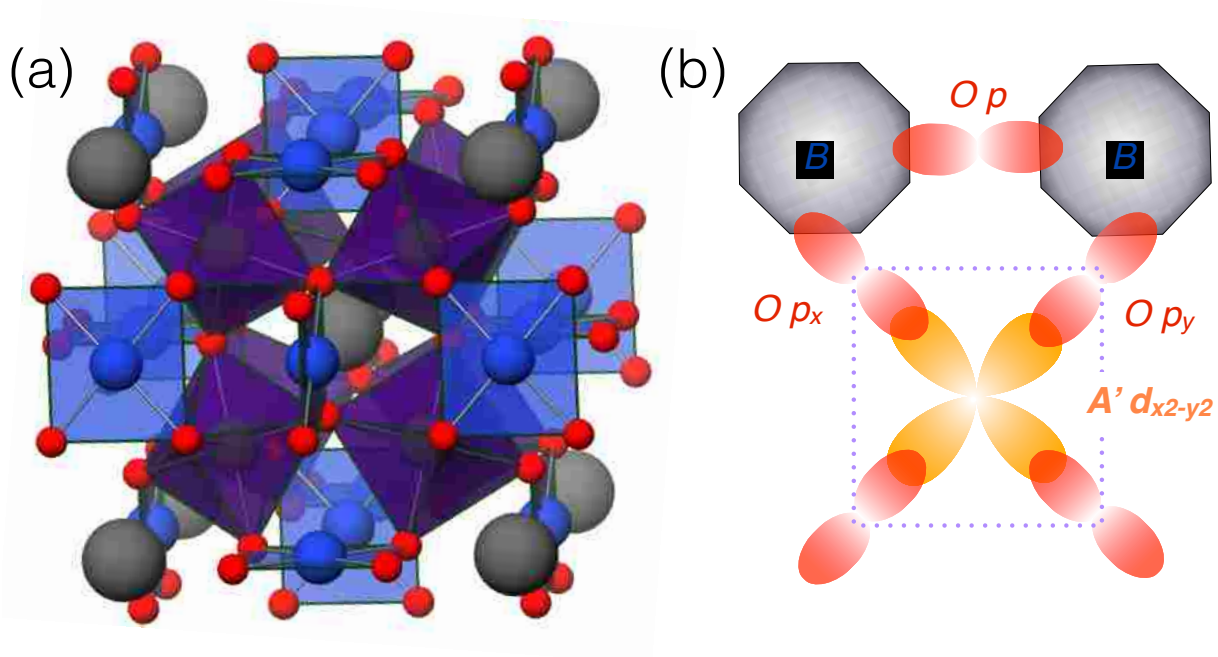

Figure 1.7: (a) Crystal structure of A-site ordered perovskites, the A-site represented by dark grey, A' by blue spheres (planes), B by purple spheres (octahedra), and O by red. (b) Orientation of O-p orbitals and resultant bonding with A' and B-sites.

chosen, but there is no guarantee that a stable structure will be obtained, thus a limited set of A and A' ions can be utilized. Despite these issues, there are several advantages to this new doping regime.

As mentioned, a key issue in random doping revolves around the various structural disorder, i.e. defects, lattice changes, non-uniformity, etc. The $AA'_3B_4O_{12}$ immediately addresses the issues of non-uniformity and precise percentage of doping. Structurally, displayed in Fig. 1.7(a), the system takes on $Im3$ symmetry and consists of the typical perovskite octahedrally coordinated B-site and an alternating planar coordinated A'-site, each separated by the A-site, typically a rare-earth ion. It is this planar coordination that preferentially selects the Jahn-Teller ion for occupation, which prevents intermixing of the A' and B-site. This is a key limitation for the available materials for the two sites. However, it is also a sizable advantage as well, giving precise ordering that numerous studies have been able to confirm through Rietvald refinement of power diffraction, examples are shown elsewhere[10]. One of the most unique features of this crystal system is the conservation of the $Im3$ symmetry no matter what ions are chosen for each site. This is in strong contrast to doping, where symmetry changes are common as certain critical doping percentages are crossed. Instead,

the different sizes and bonding of the ions cause the lattice constants and trigonal distortion of the BO_6 octahedra to change.

1.2.2 Electronic Structure

Electronically, the unusual arrangement of TMO ions within two distinct sublattices and the ability of the structure to accommodate different TMO ions leads to an extremely broad range of electronic phenomena including the previously mentioned high dielectric constant, ferromagnetism, Zhang-Rice physics, etc[10, 11, 23, 24, 28, 29]. As shown in Fig. 1.7(b), there are then O-sites which connect two B-sites and connecting a B-site and an A'-site giving different exchange pathways. With the caveat that the A'-site is a strong JT ion, the numerous possible ions and the complicated interactions make a comprehensive overview beyond the scope of this thesis. A subset of this broad field, AOPs with A = Ca and A' = Cu include a large number of interesting phenomena.

Cu^2+ ions are an extreme case of a JT ion, with 9 d electrons or a 1 d hole as is sometimes a more convenient convention, that generally form a planar O coordination, with the apical O-Ni distance being much greater then the in-plane O-Ni distance. In the optimally doped high T_c superconducting cuprates, for example, such as $YBa_3Cu_4O_{7-\delta}$ ($\delta \sim 0.07$), there is only one apical O for the planar coordinated Cu. In the case of the A-site ordered perovskites the Cu is entirely planar (i.e. no apical O) but also lacks the psuedo-infinite 2D structure of the cuprates, due to the alternating orientation of each plane. One of the key features of the cuprates is the Zhang-Rice state, which is formed when holes are doped in the planar O and a singlet state is formed between these doped hole states and the single hole in the Cu d-band, this is a key component of high temperature superconducting cuprates and as such has undergone extensive study[30]. In the cuprates it is typically necessary to change stoichiometry to achieve this hole doping on O, which carries with it, as discussed previously, complications for the structure and defect analysis. Within the AOPs, O deficiency is not used, but the unique bonding with the Cu-O-B, and the lesser π-bonding directly between the B-site and Cu, suggests the choice of B-site can alter the electronic structure of the Cu-O planes, possibly leading to a Zhang-Rice state analogous to what is observed for cuprates.

Finally, the B-site being unrestricted allows investigation of a myriad of possible ground states. While, ionically at least, we typically take Cu and Ca as having a 2+ valence,

and O with 2-, the chemical formula takes the form $Ca^{2+}Cu_3^{2+}B_4^{4+}O_{12}^{2-}$. However, when considering the strong JT nature of Cu and the discussion from the previous paragraph, it is evident that Cu and O can deviate from their ionic valences. From the self-doping of the Cu-O planes standpoint, changing B-sites to an element that does not typically take on the 4+ valence state could allow an avenue to dope holes into the plane, which could conceivably be controlled by increasing the Z value of the B-site, which, as discussed in section 1.1.2, increases the overlap of the B-site and O orbitals. Even more intriguing, elements featuring unfilled 4 or 5d shells, instead of the more typical 3d, have been used which allows the mixing of not only 3d and 2p orbitals, but also 4 or 5d orbitals with strong spin-orbit interaction all within the same lattice making these systems a true curiosity and leading to unexpected, emergent behavior[11, 31]. The investigation of a small subset of these materials, featuring strong Zhang-Rice and an emergent heavy fermion state, is covered in Chapter 3.

1.2.3 Ordered doping

As discussed thus far, the AOPs allow replacement of the various ions within the same structure without symmetry changes and with no accompanying defects. In this thesis, we only consider the cases where A = Ca and A' = Cu, where the B-site will be changed to electronically dope the Cu ions. This method has proven to be a powerful tool for engineering the ground state of these systems, the effects on the Cu ground state and the physical properties of the compound are quite intriguing[10, 11]. The utility of this technique is, however, not restricted to these restricted cases and this new doping paradigm could emerge as a very powerful method in the coming decade.

1.3 Rare-earth Nickelates: Epitaxial and digital engineering

Among the perovskites, materials sharing common B-sites but different A-sites are typically grouped and referred to by the corresponding B-site. Originally synthesized as bulk crystals in 1971 by Demazeau *et al* and further characterized by Lacorre and Torrance *et al*, the rare-earth nickelates are a robust perovskite system with myriad ground states and order parameters[5, 32, 33]. Renewed interest in this system is owed to the emergence of anomalous phases in similar 3d TMOs, the manganites featuring colossal magnetoresistance and the cuprates showing high temperature superconductivity. Additionally, the prediction of an artificial high temperature superconducting state by Chaloupka *et al* in 2008 further

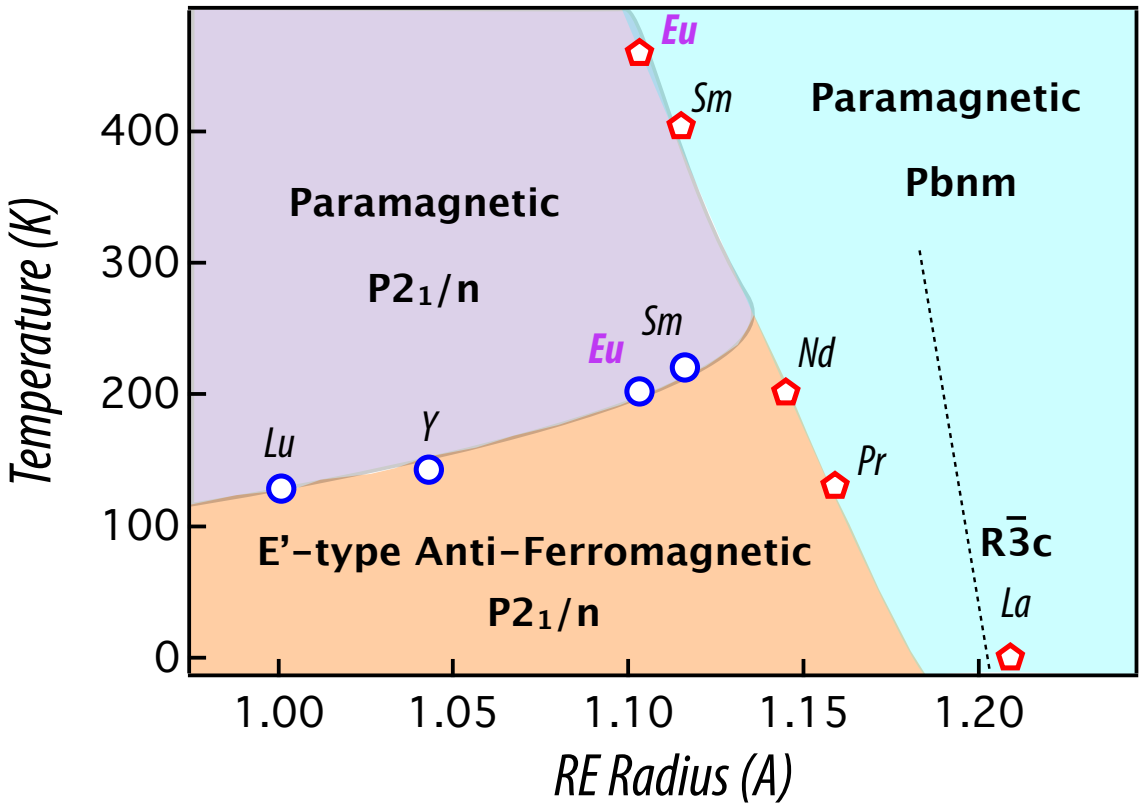

Figure 1.8: Rare earth nickelate phase diagram, originally published here[4]. As the rare-earth radius decreases, the symmetry progressively lowers due to steric effects and several transitions occur[5].

spurred interest and, in particular, motivated intense work on heteroepitaxial thin films of nickelates[34].

1.3.1 Crystal Structure

Rare-earth nickelates belong to the TMO perovskites when stabilizing Ni in the 3+ valence state, as opposed to the more stable Ni 2+ state in common to NiO with edge sharing octahedra allowing the lower oxidation state. Early synthesis of bulk powders required high oxygen pressure and temperature to stabilize Ni^{3+} and production of the NiO impurity phase is very energetically favorable when growth conditions do not fit the proper criteria[32, 33, 5, 35]. Thus, the nickelates present a formidable challenge for not only bulk synthesis but for thin film synthesis as well.

Despite these synthesis issues, a wide range of A-sites have been stabilized within the structure, spanning nearly the entire Lanthanide group and allowing a detailed phase diagram to be obtained as a function of the RE radius, or similarly the tolerance factor, t, Fig. 1.8. Structurally, the highest symmetry material created has been $LaNiO_3$, which belongs to the rhombohedral crystal system, $R\bar{3}c$ group, which can be viewed as a small stretching of a cubic lattice along the (111) direction. La is nearly the ideal A-site size in comparison to Ni, giving a large t of 0.94[5, 17]. As the A-site's Z is decreased several changes occur. Structurally, the smaller ionic radius leads to lowering of t as the A-site moves further from the ideal size, and steric effects cause the symmetry to lower changing the crystal system to orthorhombic, $Pbnm$ group at high temperature and a further lowering to the monoclinic system, $P2_1/c$ at low temperature, Fig. 1.8 left. The degree of the monoclinic distortion at the ground state, which can be quantized as the divergence of β away from 90°, at low T increases as the ionic radius is further lowered. The increase in the monoclinic distortion is accompanied by decrease in the lattice volume, and hence a decrease in the Ni-O-Ni bond angle. This buckling of the bond angle can be linked to several properties in the nickelates, as the overlap in the Ni-d and O-p orbitals contributes significantly to the t and hence the bandwidth, as discussed earlier. Interestingly, the average Ni-O distance is nearly identical between compounds, suggesting the NiO_6 octahedra act as rigid bodies which tilt and rotate to fill in the voids created by the smaller rare earth ions. Further complicating matters however, when t becomes very small, as for RE = Lu, Y, etc, a static Jahn-Teller (JT) distortion of the octahedra is observed, while for lower t compounds this has not been observed, but a dynamic JT polaronic mode is possible[36]. However, resonant scattering experiments have not found a signature of this mode in $NdNiO_3$ and further work is still needed.

When considering a particular compound among the rare earth nickelates ($RENiO_3$), the symmetry change from $Pbnm$ to $P2_1/c$ as the temperature is decreased for all the nickelates, except for $LaNiO_3$, is coincident with the metal-to-insulator transition in these compounds, discussed in the next section. Contained within the symmetry change, several structural changes become important. Foremost, from structural data it is clear there is also a coincident, abrupt volume compression of about 0.2%[37]. This indicates the transition is first-order, and a clear hysteresis is also observed. A buckling of the Ni-O-Ni bond angle results, changing the overlap, and thus the bandwidth, of the Ni and O orbitals. This is also commonly linked to the MIT, though the entire story is far more complicated.

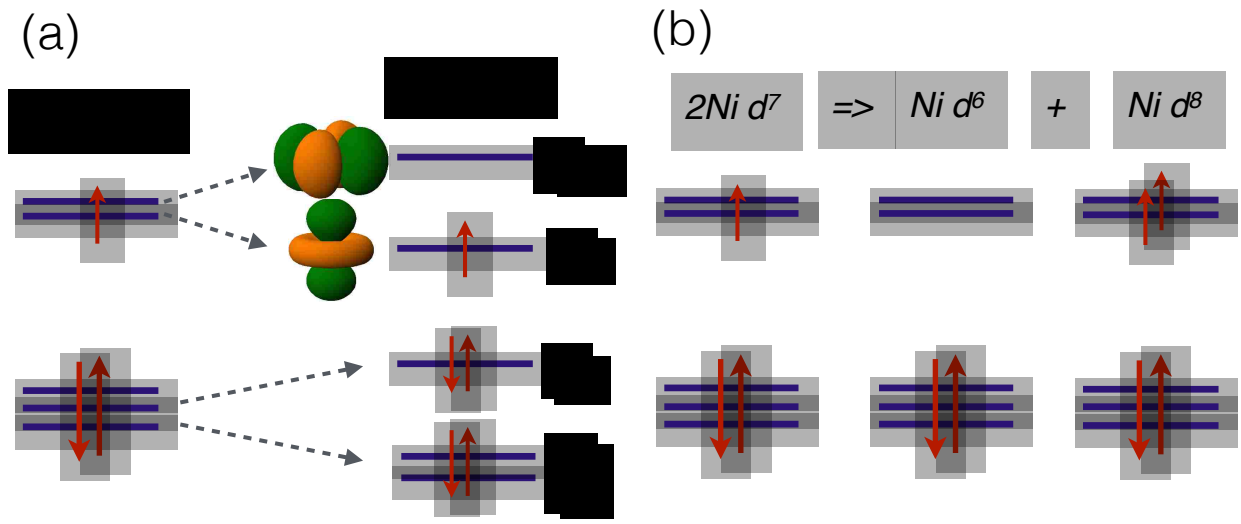

Figure 1.9: (a) A possible tetragonal JT distortion of the nickelates. JT only observed thus far in highly distorted systems. (b) Charge disproportionation, another mechanism of avoiding a degenerate ground state.

1.3.2 Electronic Structure

Electronically, the rare earth nickelates encompass a diverse and intriguing phase space. However, the basic electronic structure is of great importance in addition to the previously discussed structural and, resulting, bandwidth changes. Ionically, rare earth nickelates all take the form $RE^{3+}Ni^{3+}O^{2-}$, with the low-spin d^7 state for Ni, electronic configuration $t_{2g}^6 e_g^1$. As mentioned previously, the nickelates were predicted to harbor a superconducting state, which was theorized due to the single electron in e_g band, analogous to the single hole state in high temperature cuprates[34]. One key difference between these two materials is while both are predicted to be strong JT ions (Cu^{2+} and Ni^{3+}), in the cuprates the JT effect is so strong that the Cu can be considered as nearly planar with O, while the nickelates show either no JT or are a very small one in the highly distorted cases (low t), Fig. 1.9(a)[36]. From the electronic structure point of view, this violates the Jahn-Teller theorem as the two e_g states available to the single electron are then degenerate in energy, which creates a large entropy in the system going to 0 K. Resolving this issue, a charge disproportionation occurs at the MIT and lifts the degeneracy as shown in Fig. 1.9(b). The Ni d^6 and d^8 state have either two fully unoccupied orbitals or two half-filled

orbitals. As shown in Fig. 1.8, this CO has been seen to occur commensurate with the MIT in all of the nickelates, though the methods used were varied[38]. However, this simple ionic explanation is not entirely accurate, as numerous studies show the ground state has a significant contribution of the $d^8\underline{L}$ state, which is no surprise due to large Z value for Ni lowering the energy of the d-states leading to a strong mixing with O near the Fermi level, as discussed in section 1.1.2. Due to this, the O-p orbitals must also be considered, and theoretical studies have found that a CO shared between the Ni and O ions is likely[39, 40]. Unfortunately, due in part to the relatively low energy of the O K-edge, discussed in chapter 2, finding this ordering on O is extremely difficult and has not been undertaken thus far.

In the insulating state, magnetic moments are formed by the localized electrons. In the more distorted nickelates, a paramagnetic insulating state is first stabilized below the MIT with a transition to anti-ferromagnetic behavior at a lower temperature, denoted T_N, as seen in Fig. 1.8. This ordering is of E' type, which consists of (111)-oriented ferromagnetically-coupled planes with neighboring planes ferromagnetically- (in one direction) and anti-ferromagnetically-coupled (in the other), giving an up-up-down-down repeated pattern in the (111) direction, Fig. 4.5 and 4.8. Neutron studies have shown the magnetic moments are around 0.8 - 0.9 μ_β[41]. Interestingly, more detailed x-ray resonant scattering measurements were interpreted, at least for $NdNiO_3$, to give a complicated non-collinear structure involving the Nd ions[14]. However, due to the strong magnetic properties of Nd in general, such a complicated magnetic structure cannot be assumed for other rare-earth nickelates. The unusual E'-type ordering is attributed to Fermi surface nesting, where large parallel regions of the Ferm surface are connected by the $(\frac{1}{4}\ \frac{1}{4}\ \frac{1}{4})$ psuedocubic vector in reciprocal space, leading to the observed spin density wave[39].

The metal-insulator transition itself is of great interest and practical importance, generating numerous research studies over the past two decades on nickelates, vanadates, and etc[42]. In the nickelates, the origin of the MIT is still hotly debated and numerous theories abound, despite the extensive experimental and theoretical work done[38]. Despite the lack of a consensus understanding of the MIT, manipulation of it's temperature and magnitude is readily done through various means, as shown in Fig. 1.8 for different rare-earth radii. In this case, the change in MIT was attributed to a gradual reduction in bandwidth as the Ni-O-Ni bond angle is decreased. Likewise, hydrostatic pressure has been extensively utilized to tune the MIT temperature, however the required pressure can be quite high[43, 44, 38]. Thermal hysteresis, compatible with the first-order nature of the MIT drawn from structural effects,

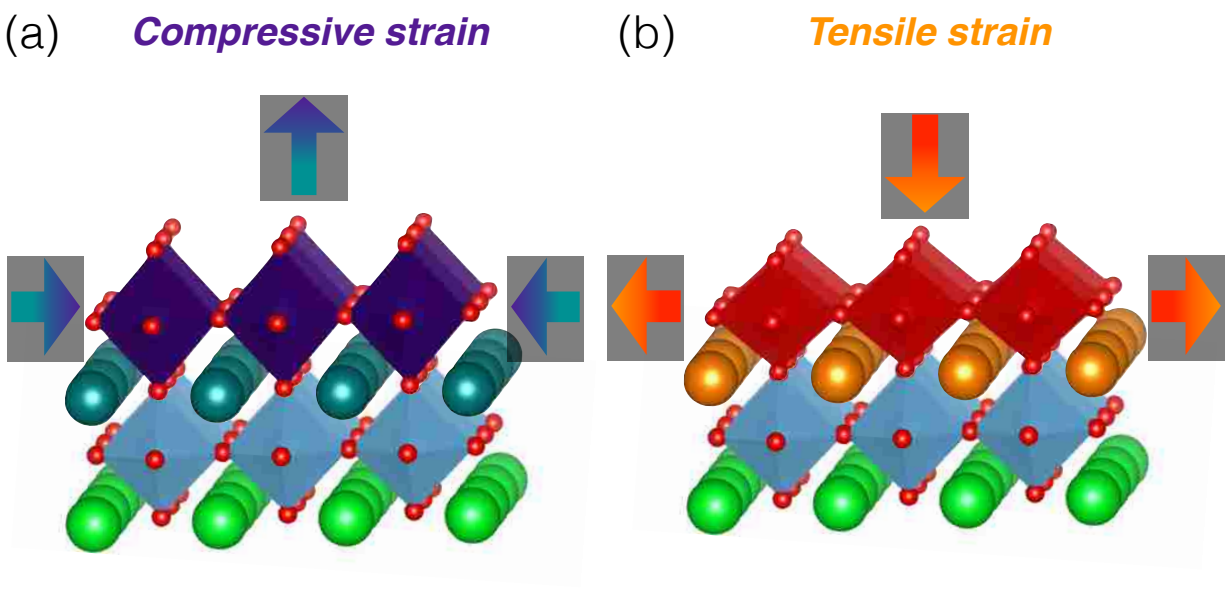

Figure 1.10: (a) A compressively strained epitaxial film, represented by purple octahedra and teal A-sites, grown on a substrate, represented by blue octahedra and green A-sites. (b) Tensile strained film, represented by red octahedra and orange A-sites, grown on same substrate. Arrows indicate the in-plane and out-of-plane responses of the films lattice to the applied strain within the Possion picture.

is present for RE = Pr, Nd, where there is no intermeadiate paramagnetic, insulating phase. However, for the nickelates with lower tolerance factor the thermal hysteresis is not present, and the lack of the coupled magnetic transition at the same temperature is believed to cause a weakening of the effect[38]. However, structural measurements still show a sudden volume expansion for these materials, thus the first-order nature cannot be ignored[37]. Investigation of the MIT in nickelates forms a central theme in this thesis and will be discussed at length in chapters 4 and 5.

1.3.3 Lattice mismatch engineering

Among the most heavily studied of the emerging methods for engineering materials properties is the use of lattice mismatch as a tool to artificially distort the material's lattice in a controllable way[4, 12, 45, 46, 47, 48, 49, 50, 51]. This effect is in fact a necessity to consider for any work utilizing thin films as, except for the case of homoepitaxy (growing a thin film of a material on a substrate composed of the same material), there is always some difference between the size of the two lattices. Generally speaking, this leads to two

outcomes: 1) the film stabilizes itself on the surface of the substrate with only weak coupling to the surface, Van Der Waals forces, where there is no direct correlation between the atomic positions of the substrate's atoms and the film's, and 2) the film is stabilized on the surface with strong bonding, ionic or covalent, between the substrate's atoms and the film's, giving a direct correlation between atomic positions of the substrate and film. When the film's lattice-sites line up with the substrate's, as seen looking in the growth direction, we say the film is fully epitaxially strained. Except for the case of homoepitaxy, i.e. the growth of a thin film of a compound on a substrate consisting the same compound, the grown material's bulk lattice constants do not exactly match the substrate's, leading to a distortion of the unit cell. In the previous two sections the importance of the crystal lattice to the materials properties has been expounded, and this distortion, referred to as lattice mismatch or strain effects, can have a dramatic effect on materials properties.

Two distinct regions exist, one where the grown film has a larger lattice constant, referred to as compressive strain, and one where the lattice constant is smaller, tensile strain, Fig. 1.9. While compressive strain is somewhat similar to externally applied isotropic pressure, though by no means equivalent, tensile strain has no external analog apart from chemical pressure induced by doping, which, as discussed earlier, carries it's own issues. Possion's ratio relates the biaxial compression (stretching) with stretching (compression) in the other direction, as shown. The strain applied to the film can be quantified by a simple formula, eq. 1.6.

$$\epsilon = \frac{a_{substrate} - a_{film}}{a_{film}} \tag{1.6}$$

where $a_{substrate}$ and a_{film} are the psuedcubic lattice constants of the substrate and film respectively. The main effect which has importance to the physical properties of the material is the distortion of the BO_6 octahedra, which acts as a tetragonal-type distortion leading to the breaking of the orbital degeneracy as shown Fig. 1.9(a) (for compressive strain). Increased orbital overlap of the in-plane orbitals and decreased overlap in the out-of-plane direction causes the shifting of the energy levels, with tensile strain having the opposite effect. However, this rather simple view on strain response is often incorrect, and caution must be utilized when interpreting results as it was shown that tilting, rotation, and breathing modes of the octahedra can also absorb the strain and keep the out-of-plane constant nearly identical to what is expected in bulk[52]. Further, another consideration is strain relaxation, which is dependent on not only the amount of strain and the thickness

of the film, but also intrinsic properties of the material[35]. Typically, the strain is slowly relaxed through multiple layers of material, and this can lead to thickness dependence which can easily be misunderstood. Abrupt symmetry changes across the interface between the materials can also modulate properties and effect the quality of the growth[53]. Finally, the charge of individual atomic layers can also cause quite dramatic effects. For instance, in the case of a (001)-oriented $SrTiO_3$ substrate terminating with a $Sr^{2+}O^{2-}$ or $Ti^{4+}O_2^{2-}$ layer, both will be charge neutral. When $LaAlO_3$ is grown epitaxially on these surfaces, the first layer is either $La^{3+}O^{2-}$ or $Al^{3+}O_2^{2-}$, having charges of +1 and -1 respectively. This leads to the so-called polar catastrophe, or a potential that diverges as the thickness of the film increases due to the uncompensated charge at the interface. Typically, the charge is compensated by add on atoms, an impurity phase, or screened by conduction electrons in metallic films[54].

For the nickelates, strain engineering has been a highly successful, if somewhat controversial, method for manipulating the phase space[38]. Numerous studies exist on $NdNiO_3$ in particular, including the first of it's kind strain-phase diagram for nickelates[4, 12, 45, 46, 47, 48, 49]. These studies expound the extraordinary ability of the nickelates to incorporate large amounts of strain and the significant electronic reconstructions that this problem results in. Due to issues with increased destability in more distorted nickelates, only the RE = La, Pr, Nd, and Sm materials were grown in epitaxial form until relatively recently. While several interesting and important phenomena were learned through these materials, the lack of the intermediate paramagnetic, insulating state and the entanglement of all the transitions at the same temperature makes it difficult to understand the results thoroughly and does not always give a complete picture of the underlying physics. A relatively new movement towards stabilization of the most distorted, lower t, members of the nickelate family has emerged, and the first realization of $EuNiO_3$ epitaxial films is covered in Chapter 4.

1.3.4 Digital control

Another interaction which can prove quite important for epitaxial films is the coupling of charge, spin, and orbital degrees of freedom that occurs between the substrate and the film via the interface. Typically, however, the substrates used are wide band gap insulators to avoid easy charge transfer to or from the film and the to minimize the hybridization, so these effects are ignored without compromising the physical interpretation to a good

degree of accuracy. However, if a small-band gap insulating or metallic substrate is used, these effects cannot be ignored. While the interface with the substrate is important to consider, the interface with vacuum can also be of importance for very thin films where the under-coordinated surface can markedly change the electronic bonding to compensate. Interestingly, the introduction of a band-gap insulator on top of the film, to remove the uncoordinated surface, can change the properties significantly[55]. Going further, repeating this stacking pattern, i.e. superlatticing, of two disparate materials can give rise to interesting properties which are not necessarily shared by the constituent layers[56]. Transfer of charge, coupling of spin degrees of freedom, and symmetry breaking all can occur within the same superlattice giving these artificial quantum materials great promise for use to realize designer phases of materials. Theoretical studies have predicted several anomalous phases to appear in this regime, and the nickelates in particular have been predicted to harbor high temperature superconducting phases and topological insulating phases, with both cases involving a band-gap insulating inactive layer in-between the active nickelate layers[34, 57].

Another potential avenue of exploring digital control, a natural extension of the RE phase diagram, nickelates with doped A-sites have also been extensively studied[38, 58, 59, 60]. This allows a very precise movement along the phase diagram, but carries the usual caveats of doping, i.e. structural issues. Heterostructuring offers the ability to create layer-by-layer structures of undoped nickelates, which when repeated multiple times could behave as a doped system with fractional A-site ordering. We refer to this method as digital control, and such an avenue for manipulation of the nickelate phase space is explored in Chapter 5.

2 Experimental techniques

In this chapter we will examine the principal techniques utilized in this thesis to explore the phase space of correlated oxides. First, an in depth look at the utility of both x-ray absorption spectroscopy and resonant scattering for determining both charge, orbital, spin, and structural orderings is explored which forms the basis of our investigation of the effects of creating designer materials. Further, a detailed description of our in-house synthesis technique, pulsed laser deposition, describes how to create ultra thin films of complex oxides. Finally, the stabilization of the first ultra thin, single-crystals of $EuNiO_3$ via this synthesis method is inspected, and a general nickelate growth phase diagram is revealed based upon our lab's growth of rare earth nickelates, $RENiO_3$ (RE = La, Pr, Nd, Eu, Y) thin films.

2.1 Interaction of light with matter

Understanding the interaction of electromagnetic radiation with matter was one of the greatest scientific breakthroughs in physics, and, indeed, the 1921 Nobel prize in physics was awarded to Einstein for his observation that metals illuminated with light emit photo-electrons only when a certain threshold frequency (or energy) was surpassed. It took several such experimental breakthroughs and rigorous theoretical insight to truly understand this interaction.

For our work, we are only interested in the interaction between light and the electrons in a solid, further interactions are ignored within this approximation, and the interested reader can find them elsewhere[61]. More detailed descriptions of the following discussion can be found in Refs. [62, 63, 64, 65]. We start with the hamiltonian of a free electron,

$$H_{f.e.} = \sum_n \frac{\rho_n^2}{2m} \tag{2.1}$$

where ρ_n is the momentum of the n^th electron and m is the electron mass. The introduction of light, which carries momentum quantifiable by the vector field $\hat{A}(r,t)$, then alters the momentum of the hamiltonian giving,

$$H_{\text{total}} = \sum_n \frac{(\rho_n - e\hat{A}/c)^2}{2m} \tag{2.2}$$

or,

$$H_{total} = \sum_n (\frac{\rho_n^2}{2m} - \frac{e}{mc}\rho_n \cdot \hat{A} + \frac{e^2}{2mc^2}\hat{A} \cdot \hat{A}) \tag{2.3}$$

where the assumption of a transverse light wave was utilized so that $\hat{A} \cdot \rho_n = \rho_n \cdot \hat{A}$ which is violated for only very special cases[66]. Utilizing second quantization, the vector field $\hat{A}$ can be expressed in terms of photon creation and annihilation operators,

$$\hat{A}(r,t) = \sqrt{\frac{2\pi\hbar c}{V}} \sum_{k,i} \frac{1}{\sqrt{k}} e_i (a_{k,i}^-(t) e^{ik\cdot r} + a_{k,i}^+(t) e^{-ik\cdot r}) \tag{2.4}$$

where $a_{k,i}^+(t)$ and $a_{k,i}^-(t)$ are the creation and annihilation operators respectively for photons of wave vector k and polarization e_i. Thus, ignoring the first term of 2.3 (which is just the free electron term) we see that the second term, being linear in $\hat{A}$ corresponds to either the creation of annihilation of one photon, while the third term, quadratic in $\hat{A}$, can either create 2 photons, annihilate 2, or annihilate 1 and create 1, not changing the total photon count.

Thus we can classify interaction events into two types, type 1) corresponds to the linear term in 2.3, creating or annihilating a photon, and type 2) corresponding to the quadratic term in 2.3 which can either create 2, annihilate 2, or leave the total photon count unchanged. The second and third terms of 2.3 can be treated separately as perturbations to the original $H_{f.e.}$. For our measurement methods we detect photons, so we are interested in first order pertubations, $\mathrm{W}_1 = \langle G| \hat{A} \cdot \hat{A} |G\rangle$ involving only the quadratic term where one photon is destroyed and one is created (for us to detect), and we can also detect second order perturbations involving the linear term applied twice, $\mathrm{W}_2 = \langle G| (\rho \cdot \hat{A})^+ |I\rangle \langle I| (\rho \cdot \hat{A})^- |G\rangle$, where $|G\rangle$ is the ground (unperturbed) state and $|I\rangle$ is the intermediate state. In the second order perturbation the process first annihilates and then creates a photon, with the intermediate state having no photon. It should be noted that while for our purposes we only discuss these terms, other powerful techniques utilize the terms not discussed here[61].Using these two terms, the probability that an incoming photon will be scattered into a a given solid angle can be expressed by the differential cross section, eq 2.5.

$$\frac{d\sigma}{d\Omega} = r_0^2 \left| \mathbf{e} \cdot \mathbf{e}' \langle G| \hat{A} \cdot \hat{A} |G\rangle - m \sum_I \frac{\langle G| (\rho \cdot \hat{A})^+ |I\rangle \langle I| (\rho \cdot \hat{A})^- |G\rangle}{E_I - E_G - \hbar\omega - i\Gamma_l/2} \right|^2 \tag{2.5}$$

Here $\mathbf{e}$ and $\mathbf{e}'$ are the polarizations of the absorbed and emitted photons respectively,

r_0 is the classical electron radius, and Γ_l is the lifetime of the intermediate state. The differential cross section also defines the scattering length $\frac{d\sigma}{d\Omega} = |f|$. We can then write this equation representing the scattering of light from an atom in a crystal in simplified terms as in 2.6.

$$f(\mathbf{E},\mathbf{Q},\mathbf{e},\mathbf{e}') = f_{Th}(\mathbf{Q},\mathbf{e},\mathbf{e}') + f_{Dis}((\mathbf{E},\mathbf{Q},\mathbf{e},\mathbf{e}') \tag{2.6}$$

Where $\mathbf{Q} = k - k'$, the difference of the absorbed and emitted light's wave vector (Th = Thompson scattering, Dis = Dispersion correction). The most important consequence one can draw from this equation is that the first term, often referred to as the Thompson scattering term, depends on $\mathbf{Q}$ and the polarization of the light ($\mathbf{e}$), but not on the energy of the incoming light. The second term, referred to as the anomalous dispersion correction or resonant scattering length, depends strongly on the E, as can be seen from eq. 2.5, and becomes *extremely* important near an absorption edge (where the denominator, $E_I - E_G - \hbar\omega - i\Gamma_l/2$, diverges).

The resonant scattering length comes from a step-process involving the annihilation and then creation of photon. This annihilation event is the absorption of an x-ray by a core level electron, which is the source of x-ray absorption spectroscopy. Thus we expect there to be a relation between the resonant scattering length and the x-ray absorption cross section. We start with the transition probability per unit time given by the Fermi's golden rule.

$$\omega_{abs} = \frac{2\pi}{\hbar} \sum_F |\langle I| H |G\rangle|^2 \delta(E_I - E_G - \hbar\omega) \tag{2.7}$$

The absorption cross section, $\frac{d\sigma_{abs}}{d\Omega}$, is equal to $\frac{\omega_{abs}}{\Phi}$, where Φ is the photon flux. H is then the second term in equation 2.3 applied only once. This leads to the final simplified form for the absorption cross section, eq. 2.8.

$$\frac{d\sigma_{abs}}{d\Omega} = \frac{4\pi}{k} Im[f_{Dispersion}] \tag{2.8}$$

This equation is quite important as it shows that: i) x-ray absorption contributes only to the imaginary part of the resonant scattering length and ii) utilizing Kramers-Kronig relations the real part, which contributes to the scattering but not the absorption, can be found. Thus the total interaction can be broken into three parts, typically written as in eq. 2.9.

Table 2.1: Relation between the more widely used atomic notation and X-ray notation

Atomic notation	$1s_{1/2}$	$2s_{1/2}$	$2p_{1/2}$	$2p_{3/2}$	$3s_{1/2}$
X-ray notation	K_1	L_1	L_2	L_3	M_1

$$f = f_{Th} + Re[f_{Dis}] + i * Im[f_{Dis}] \tag{2.9}$$

Measuring the emitted light due to these three terms we can ascertain several different parameters for the crystal, which can be broadly grouped into two different characterization techniques.The first two terms contribute what is referred to as x-ray scattering and will be discussed in section 2.3. First, we will discuss the contribution due to the third term, known as x-ray absorption spectroscopy.

2.2 X-ray Absorption Spectroscopy

First, let us examine the second order perturbation term which contributes the interaction leading to what is referred to as resonant x-ray absorption spectroscopy (XAS)[62]. As discussed in 2.1, for an absorption process one photon is absorbed by an electron, which means the momentum and energy of the photon must be transferred to the electron. This means a core-level electron excited by a photon to another discrete state must change its angular momentum, thus s-s, p-p, d-d, and f-f transitions, which have orbital angular momentum L = 0,1,2, and 3 respectively, are forbidden to the first approximation. Transitions are then classified as dipole (E1) type for $\Delta L = \pm 1$ (s-p, p-d, etc), quadrapole (E2) for $\Delta L = \pm 2$ and octapole (E3) for $\Delta L = \pm 3$. Typically, the lowest order term is significantly more likely to occur and throughout this thesis we will only encounter dipole-type, $\Delta L = \pm 1$, transitions. There are several possible dipole transitions, the x-ray notations for the more commonly studied transitions are shown in table 2.1, where each atomic core level corresponds to a particular absorption edge. Throughout this thesis we will heavily utilize the K_1, L_3, and L_2 transitions, which range from as low as 500 eV to 23 keV x-rays, requiring the use of both soft x-ray (300 eV to 3 keV) and hard x-ray (5 keV to 30 keV) spectroscopy.

For any given transition each element will have characteristic excitation energies, and for a specific edge, such as for example the L_1 edge, this energy increases as a function of the atomic number Z, which is due to the increasing potential as the atomic nucleus becomes

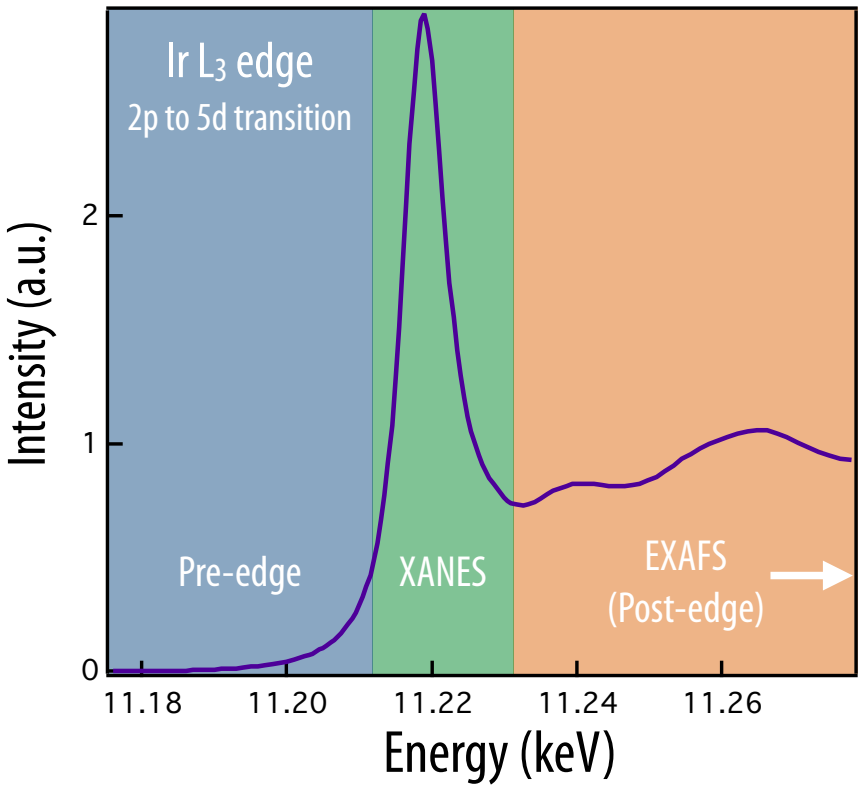

Figure 2.1: Example of an XAS scan of the Ir L_3 edge. The pre-edge, XANES, and EXAFS regions are highlighted, with the EXAFS region extending far beyond our measurement.

more positively charged while the screening due to the other electrons does not change; as can be seen in our example there is always one electron between the $2s_{1/2}$ electron and the nucleus, in the $1s_{1/2}$ state.

When measuring an absorption edge the x-ray energy is scanned from several eV below the characteristic energy across the transition and well above the edge. Three regions are then distinguished, each of which can give unique information about the material, FIg. 2.1. The first region, which is typically called the pre-edge region, encompasses the area with lower energy then the absorption edge. Quadrapolar transitions (E3) typically occur in this region, and can give useful information for some materials that will not appear in this thesis. The middle region, encompassing the transition energy and 10 to 100 eV above it is referred to as the x-ray absorption near edge structure or XANES, this is the principal region we will investigate in this thesis. We are most interested in the absorption threshold, where the main dipole (E2) transition occurs. This energy is extremely sensitive to the local coordination of the element being investigated, it's valence, and the unoccupied density of

states of the material. Above the threshold, low-energy electrons are also excited which are subject to large backscattering and lead to multiple scattering giving an oscillation as a function of energy. These peaks can then give information on the valence, local coordination, and distortions. The final region encompasses energies starting at about 150 eV to 2 keV above the absorption edge and is typically referred to as the extended x-ray absorption fine structure (EXAFS) region. The higher energy photoelectrons created highly likely to only be scattered by one neighboring atom, which gives oscillations that can be subjected to a Fourier transform from reciprocal to real space to give very detailed information about the nearest neighbor distances and structure.

2.2.1 Single electron picture

The simplest model of the XAS absorption edge involves considering only the excited electron, with a static background density of states (DOS) and no interactions with other electrons, the core hole, or further complications. We take as an example the L_3 and L_2-edge which is heavily studied in transition metal oxides. The 2p level where the electrons are excited from is a fully filled core-level shell with n = 2, l = $\pm$1, 0 and s = $\pm$ 1/2, thus we have 6 degenerate states. However, spin-orbit coupling can be quite strong for this shell, and thus we have to consider the j-j coupling effects. With total angular momentum j = $|l + s|$ - $|l - s|$ we have possible states of j = 3/2 or 1/2. The magnetic quantum number is then m_j = j,j-1,...,-j. Thus for the j = 3/2 angular momentum we have m_j = 3/2, 1/2, -1/2, -3/2 and for j = 1/2, m_j = 1/2, -1/2. In table 2.1 we identified the L_3-edge as the j = 3/2 level and L_2 edge as being the j = 1/2 level, and based upon the available electron states it is clear that, with a non-infracting excited electron, the L_3 edge should be twice as intense as the L_2, as there are twice as many electrons available to excite. The energy gap between these two resonant edges increases with increasing atomic number, as the spin-orbit interaction goes as a function of $\sim Z^4$. When we excite one of these electrons to the unoccupied states (valence shells above the Fermi level), shown schematically in Fig. 2.2(a), we produce a prototypical absorption edge which we will encounter throughout this thesis. As Fig. 2.2(a) demonstrates, the core levels are delta functions, having no bandwidth, whilst the occupied and unoccupied DOS near the Fermi level are broad, and in reality do not have the shown simplistic shapes. Thus the XAS spectrum will reveal information about the unoccupied DOS near the Fermi level if the dipole selection rule allows the transition. In our case, for

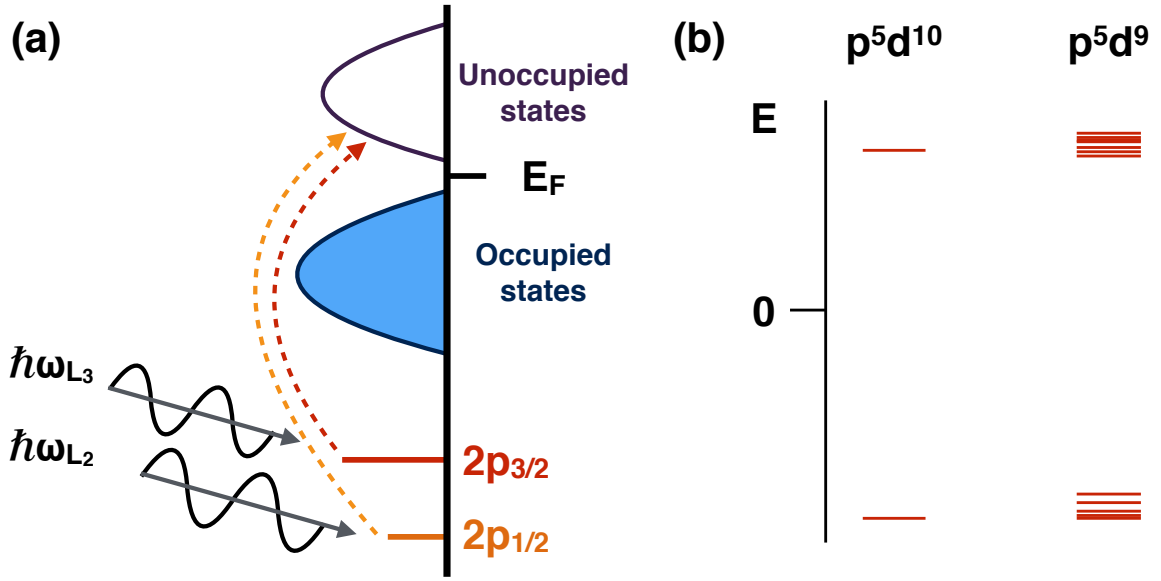

Figure 2.2: (a) Simple one-electron picture model. An incoming photon with either ω_{L_3} or ω_{L_2}, and correspondingly E_{L_3} or E_{L_2}, excites the corresponding electron to the unoccupied density of states. The separation of $2p_{3/2}$ and $2p_{1/2}$ is due to spin-orbit coupling. (b) Two possible intermediate states showing the drastic increase in available states as the d-count goes from d^9 to d^8.

transition metal oxides the unoccupied DOS near the Fermi level are almost exclusively the $3d$ states, typically with some hybridization with O p-orbitals, which means the L_3 and L_2 edges are typically the most informative, and the bulk of this thesis concerns these edges.

2.2.2 Excitons and multiplets

In reality, the single electron picture is rarely applicable and only in systems with very weak electron correlations, whereas in complex oxides electron correlations are key contributors to the underlying physics, and thus a more in-depth model of XAS must be taken into account. One of the most important interactions that occurs when a core hole is created and an electron is put in the valence band is their mutual attraction. While the system is in the intermediate state, due to the core-hole interaction, an exciton is formed. In this event, a single-particle theory is no longer of use and a many particle representation must be used. This can become quite cumbersome, as the possible intermediate states can become very numerous, especially in the case of excitations to the d orbitals with multiple unoccupied states. For examples, if we take the case of the L-edge for Cu^{2+} with ground state $2p^63d^9$, or only one unoccupied state in the d-band, for the excited state $2p^53d^{10}$, there are 6 possible

Table 2.2: Selection rules for dipole transitions

Δl	Δm_l	Δj	Δm_s	ΔL	ΔS	ΔJ
$\pm$ 1	0, $\pm$ 1	0, $\pm$ 1	0	0, $\pm$ 1	0	0, $\pm$ 1

final state configurations, as there are 6 available orbitals for the core hole. However, going just one step further to the $2p^6 3d^8$ ground state, we see that the excited state, $2p^5 3d^9$, still has 6 available orbitals for the core hole, but now the excited electron has 10 possible orbitals for the hole in the d-band to occupy, giving *60* possible final states. Due to the orbitals in the p- and d-bands all having different spatial orientations, the interaction strength between the core hole and electron are different in each case, resulting in each possible intermediate state having a distinct energy. This is referred to as the multiplet effect and this rapid expansion of the possible excited states means the XAS spectrum should be very smeared and difficult to interpret in all but very particular cases, Fig. 2.2(b). However, further selection rules can be found that greatly reduce the total number of final states available to the system, and in practice this leads to XAS spectrums which can be quantitatively understood.

From Fermi's golden rule, eq. 2.7, the transition probability is proportional to $\langle\Psi|_f T |\Psi\rangle_i$. As discussed earlier, we only need to consider the dipole transitions, so T is simply the dipole operator. Since this term is integrated over all possible states, the function must be even, or it will be odd and the probability will be 0. The dipole operator itself is odd, thus the transition must be between an even and odd state. s and d orbitals have even parity, while p orbitals have odd parity. From these symmetry arguments the selection rules given in table 2.2 are derived. These selection rules determine what final state configurations are allowed based upon which ground state the system is in. Thus, *we can determine the ground state quite accurately, making XAS an excellent probe of the electronic ground state of the specific element.*

2.2.3 Experimental details

In order to measure XAS, an x-ray source which allows the photon energy to be controllably varied across absorption edges. Third generation synchrotrons are ideal for measurements on ultra thin films. These facilities utilize insertion devices, or wigglers, which use a periodic magnetic field to undulate a stored electron beam which causes the emission of highly intense x-rays. The energy range for these undulators can go from approximately

0.3 - 50 keV. However, they are separated into two regions, the soft and hard x-ray regime. In the soft regime, approximately 0.3 - 3 keV, the photons have a wavelength in the tens of angstroms, allowing the use of spherical gratings to resolve the beam energy. However this low energy also means the scattering in air is very significant, and thus x-ray experiments must be done in-situ in ultra-high vacuum. XAS measurements in this regime are performed at the 4-ID-C beam line of the Advanced Photon Source at Argonne National Laboratory. This encompasses several edges important to the studies conducted in this thesis, including the O K-edge ($\sim$ 530 eV), Cr L-edge ($\sim$ 572 eV), Co L-edge ($\sim$ 782 eV), Ni L-edge ($\sim$ 855 eV), and the Cu L-edge ($\sim$ 930 eV). These lower energy x-rays have a much smaller penetration depth and do not allow for transmission mode measurements, where the incident and transmitted beam are measured, and the absorption edges appear as a sudden drop in transmitted intensity. Conventionally, the two modes utilized for soft XAS are total electron yield (TEY) and total fluorescent yield (TFY). TEY is measured by applying a bias voltage to the sample and measuring the current produced as a function of the x-ray energy. As electrons are excited to the valence band by x-ray absorption the increased occupation increases the current flowing from the surface into the electrical contacts. This has two major short-comings: i) it is extremely surface sensitive, typically $\leq$ 10 nm, as the excited electrons are strongly scattered and absorbed as they travel through the sample, and ii) insulating samples can become charged by the excited electrons which then causes strong background effects. In TFY mode a fluorescence detector measures the emitted x-rays as valence electrons recombine with the core-hole. This technique is much more bulk-sensitive then TEY mode, but also suffers from self-absorption effects which can severely distort the line shapes of the absorption edges. Thus, both techniques are measured simultaneously and are usually considered together to discern depth characteristics and to compensate for the weaknesses of both.

Finally, hard XAS is measured at the 4-ID-D beam line of the Advanced Photon Source. With hard x-rays the smaller wavelengths of around $<$ 4 Angstroms require the use of a Si (111) oriented crystal plates to monochromate the incident beam to an energy resolution of $\Delta E/E = 1.4 * 10^{-4}$. The x-ray energy range here encompasses several edges utilized in this thesis including the Ni K-edge ($\sim$ 8.34 keV), Rh K-edge ($\sim$ 23.23 keV), and the Ir L-edge ($\sim$ 11.22 keV). Due to the higher penetration depth of hard x-rays, transmission mode is utilized for these edges, which does not suffer from self-absorption or charging issues.

2.3 X-ray scattering

Continuing the discussion from section 2.1, the first two terms of eq. 1.9 contribute the energy-independent Thompson scattering and -dependent resonant scattering. We will discuss how these terms are measured and what information can be gathered in 2.3.1 and 2.3.2.

2.3.1 Thompson scattering

Thompson scattering is responsible for the more heavily utilized aspect of x-ray scattering, typically referred to as x-ray diffraction[65]. As discussed previously this type of scattering results from the $\hat{A} \cdot \hat{A}$ interaction, and it was shown that this term depends upon the polarization of the incident and scattered light, $\mathbf{e}$ and $\mathbf{e}'$, and it was assumed it was also dependent upon the scattering vector, $\mathbf{Q}$. This dependence is of great importance and forms the basis of x-ray diffraction.

Starting with a single scatterer, as in 2.1, we consider a beam of light incident upon a point scatterer. The scattered light is then projected in all directions, thus the scattering event can be thought of as taking a light beam with frequency ν and amplitude A propagating in a particular direction and radiating it in all directions. If we consider an arbitrary point P at distance D from the scatterer, the displacement of the wave is given by eq. 2.10.

$$Y(P) = f\frac{A}{D}e^{(2\pi i\nu(t-D/c)-i\phi)} \tag{2.10}$$

where f is the scattering length, which is a function of the angle between the direction of the incident light's propagation and the vector from the scatterer to P, and ϕ is a phase shift induced by the scattering event. The two important results are: i) the displacement is proportional to A/D, which is due to the intensity obeying the inverse square law for distance D, ii) the phase of the scattered wave is a function of the distance away from the scatterer and ϕ which will typically be fixed for a group of scatterers. We can then define the amplitude of this function as $\eta = f\frac{A}{D}$ and the intensity (power per unit solid angle) of the scattered beam as $I_{scatt} = f^2 I_0$.

When introducing a second scatterer, we make an important assumption: the point, P, at which we are observing the scattered intensity, is at a distance D much greater then $|\vec{r}|$, the distance between the two scatterers. This allows us to assume the scattered light traveling to point P is parallel. Then the most important consequence will be the phase difference

between the two separate scattered beams. We define a vector $\vec{s}$ as the difference of the unit vectors of the incident and scattered beam (to point P) divided by the wavelength of the light. The phase difference will then be $2\pi\vec{r}\cdot\vec{s}$. Thus when we consider the displacement or the amplitude of the total scattered wave at point P we find a new term must be included, Eq. 2.11.

$$Y(P) = f\frac{A}{D}e^{(2\pi i\nu(t-D/c)-i\phi))}[1+e^{(2\pi\vec{r}\cdot\vec{s})}] \tag{2.11}$$

with a resultant amplitude of $\eta = f\frac{A}{D}[1+exp(2\pi\vec{r}\cdot\vec{s})]$. This can then easily be generalized to an arbitrary group of equivalent point scatterers (still subject to the $D \gg |\vec{r}|$ restriction), eq 2.12.

$$\eta = f\frac{A}{D}\sum_j [e^{(2\pi i\vec{r}_j\cdot\vec{s})}] \tag{2.12}$$

So far, we have discussed the case of point scatterers, where the scattering length f is not known. Thompson scattering is this general description applied to the specific case of free electron scatterers, for which we can find f. This electron will respond to the light wave's oscillating electric field causes it to have an oscillating acceleration with the same frequency as the incoming light wave. Since the electron is a charged particle it radiates light upon acceleration, such that at a point P the electric field vector will be : $\vec{E} = \frac{e\vec{a}sin(\phi)}{4\pi\epsilon_0 rc^2}$, where e is the electron charge, a is the acceleration due to the incident light's electric field, r is the distance to the point P, and ϵ_0 is the permittivity at vacuum. The the acceleration has the form $\vec{a} = \frac{e\vec{E}}{m}$. An important consideration, however, is that the point P is at some angle, referred to as 2θ, so we can break down the vector into a perpendicular to and in the scattering plane, defined as the plane containing the incident light and the point P. Then the perpendicular component of the incident and scattered wave will be the same, while the in-plane component will have a factor $cos(2\theta)$. This allows us to then find the intensity of the scattered light, power per unit solid angle, as in eq. 2.13.

$$I_{sca} = \frac{1}{2}\left|\frac{e^2}{4\pi\epsilon_0 c^2 m}\right|^2 (1+cos^2(2\theta))I_0 \tag{2.13}$$

This is the general equation for a free electron scatter, but it should be noted it would work equally well for any charged particle. The factor of $(1/m)^2$, however, means the electron is by far the most important atomic scatterer, as $m_e \ll$ mass of the proton, neutron, etc. Even so, for typical crystals with lengths in the 10^{-3} m range, only 2% of the incident beam

is scattered. This is actually very important to this discussion as we are working within the kinematic approximation of scattering, which assumes there are no multiple scattering events, which is only valid while $I_{sca} \ll I_0$.

The application of Thompson scattering to atoms is the basis for x-ray diffraction, and it requires us to consider the effect of scattering from bound electrons instead of free ones. An important consequence of this is the electron can no longer be thought of as a point particle, but as a charge distribution denoted $\rho(r)$, where we assume it has spherical symmetry (i.e. no θ or ϕ dependence). We then utilize eq. 2.12, but instead of a summation over point scatterers we integrate over the entire electron volume and write the amplitude as some constant, dependent on the scattering vector $\vec{s}$, times the charge. We then obtain the general equation for the amplitude, 2.14.

$$\eta = C \int_0^{\infty} \int_0^{\pi} \int_0^{2\pi} \rho(r) r^2 exp(2\pi \vec{r} \cdot \vec{s}) sin(\psi) dr d\psi d\phi \tag{2.14}$$

,which is simply the integration in spherical polar coordinates over the charge distribution of the electron and it's contribution to the scattered wave and C represents the $\vec{s}$ dependent scattering factor. Integrating over ϕ and ψ gives eq 2.15.

$$\eta = 4\pi C \int_0^{\infty} \rho(r) r^2 \frac{sin(2\pi rs)}{2\pi rs} dr \tag{2.15}$$

From here we can consider two different cases, where we consider a point charge, r $\to 0$, will simply give us $\eta = C$ and where we consider the actual electron distribution of the atom. Thus f can be written as $4\pi \int_0^{\infty} \rho(r) r^2 \frac{sin(2\pi rs)}{2\pi rs} dr$ and is known as the atomic scattering length, which is simply a constant for an atom which will adjust the point scattering amplitude based upon the real electronic distribution.

With the Thompson scattering of an atom now worked out, we can apply the analysis to n (odd) atoms distributed in a crystal lattice with $\vec{a}$ as the distance between neighboring atoms, starting with a row of atoms along $\vec{a}$ for simplicity We can then use the center atom as the origin and write the the amplitude of the scattered wave as in eq. 2.16.

$$\eta_n = f \sum_m cos(2\pi m \vec{a} \cdot \vec{s}) \tag{2.16}$$

where m $= \pm n - 1/2(n-1)$ for integer n. Inserting $fracsin(\pi \vec{a} \cdot \vec{s}) sin(\pi \vec{a} \cdot \vec{s})$ to obtain $cos(2\pi m \vec{a} \cdot \vec{s}) sin(\pi \vec{a} \cdot \vec{s})$ in the summation and simplifying, it can be shown that the

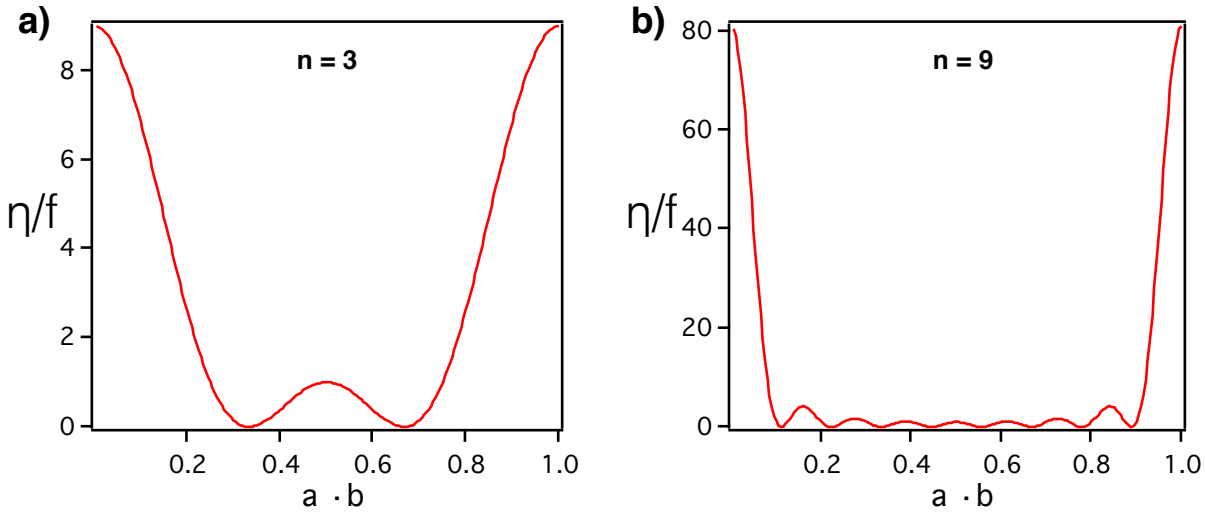

Figure 2.3: (a) With n = 3, maximums occur at $\vec{a} \cdot \vec{s}$ = 0,1 (integer). Two minima and one minor maximum are observed. (b) With n = 9, maximums again occur at 0,1, but now 8 minima and 7 minor maxima occur.

only terms that do not cancel are the first and last terms, giving eq. 2.17.

$$\eta_n = f \frac{sin(2\pi n\vec{a} \cdot \vec{s})}{sin(\pi\vec{a} \cdot \vec{s})} \tag{2.17}$$

then the intensity if just the square of this quantity. If we take values of $\vec{a} \cdot \vec{s}$ as integers, both of the sin functions go to zero. In the limit as they approach 0, $\frac{sin(2\pi n\vec{a}\cdot\vec{s})}{sin(\pi\vec{a}\cdot\vec{s})}$ goes to n^2. The properties of this function become obvious when graphed, Fig. 2.3. Some general conclusions for this equation are: i) there are $n-1$ minima, ii) there are $n-2$ minor maxima, iii) major maxima occur at integer values of $\vec{a} \cdot \vec{s}$, iv) the ratio of major to the minor maxima increases rapidly as n increases. Thus with large n peaks only occur at integer values for $\vec{a} \cdot \vec{s}$. The integer condition on $\vec{a} \cdot \vec{s}$ will be satisfied for a cone of constant angle relative to the row of n atoms, as $\vec{a}$ lies along the row and $\vec{s}$ can lie in any directions. This one-dimensional result is very important, as it is valid when considering rows of atoms along all three directions simultaneously, as in a crystal. In this case centered around every axis are cones with angles corresponding only to integer values of $\vec{a_p} \cdot \vec{s}$, where p can be either x, y, or z. Then only when we have a simultaneous intersection of three cones, one corresponding to each direction, will there by any diffracted intensity. Thus we have three conditions which must be satisfied at once for there to be an observed peak, eq. 2.18(a-c).

$$\vec{a}_x \cdot \vec{s} = h \tag{2.18a}$$

$$\vec{a}_y \cdot \vec{s} = k \tag{2.18b}$$

$$\vec{a}_z \cdot \vec{s} = l \tag{2.18c}$$

with h, k, and l integers. These conditions are known as the Laue conditions or equations, and are used in conjunction with the concept of the reciprocal lattice to describe x-ray diffraction. Defining the lattice as having three vectors, as used above, $\vec{a}_x, \vec{a}_y, \vec{a}_z$, we can also define three vectors as $\vec{a}_x^*, \vec{a}_y^*, \vec{a}_z^*$ which satisfy the following condition, eq. 2.19.

$$\vec{a_i^*} \cdot \vec{a_j} = \begin{cases} 1, & \text{if i=j.} \\ 0, & \text{i} \neq \text{j.} \end{cases} \tag{2.19}$$

this collection of three vectors forms the reciprocal lattice which has great utility in describing x-ray difraction. If we take a vector consisting of integer multiples of the reciprocal lattice, h, k, l as used above, and then take the dot product with $\vec{a}_x, \vec{a}_y, \vec{a}_z$ we get h, k, l respectively, which is the condition required for a diffracted peak from eq. 2.18. Thus, when $\vec{s} = h\vec{a}_x + k\vec{a}_y + l\vec{a}_z$ a diffraction peak is obtained.

If we now look to a real crystal, such as the ABO_3 perovskites described in section 1.2, there can be several different types of atoms contributing to the scattered intensity, thus we must generalize our description to a 3-dimensional array of scatterers, which are non-equivalent. Utilizing the unit-cell description of crystals found in section 1.2, we must denote the contribution to the scattered amplitude from each non-equivalent atom in the unit cell separately, as in eq. 2.20 for the case of three atoms making up the unit cell.

$$f_A exp(2\pi i \vec{r_A} \cdot \vec{s}) + f_B exp(2\pi i \vec{r_B} \cdot \vec{s}) + f_C exp(2\pi i \vec{r_C} \cdot \vec{s}) \tag{2.20}$$

where $f_{A,B,C}$ are the corresponding atomic scattering lengths for each non-equivalent atom. It should be noted that even atoms of the same element can be non-equivalent within the crystal, different charges at different sites, for example, which will alter the atomic scattering length. This equation can be written compactly and in a well-known form as in eq. 2.21.

$$F_{hkl} = \sum_{1}^{N} f_j exp(2\pi i \vec{r_j} \cdot \vec{s}) \tag{2.21}$$

where N is the number of non-equivalent atoms within each unit cell. F_{hkl} is referred to as the structure factor for the indices of reflection hkl. Notice this is just an extension of equation 2.16, applied to different atoms and with $\vec{a}$ replaced with the corresponding vector $\vec{r_j}$ for each atom's position within the crystal lattice. Then the scattered wave intensity is given by eq, 2.22.

$$I_{sca} = |F_{hkl}|^2 = \sum_1^N \sum_1^N f_j f_i cos(2\pi(\vec{r_j} - \vec{r_i}) \cdot \vec{s}) \tag{2.22}$$

Of great importance is the term $(\vec{r_j} - \vec{r_i})$, which shows that the distance between the scattering centers is the only relevant Typically, the non-real part of the $exp(...)$ is dropped in 2.21, as in a centrosymmetric crystal, which is the only type encountered throughout this thesis, the imaginary part goes to zero, and we are left with $F_{hkl} = \sum_1^N f_j cos(2\pi\vec{r_j} \cdot \vec{s})$. Going further, if we write $\vec{r_j}$ and $\vec{s}$ in terms of the x,y, and z positions of the scatterer and the reciprocal lattice vectors respectively, we get the following expressions, eq. 2.23(a) and (b).

$$F_{hkl} = \sum_1^N f_j cos(2\pi(x_j\vec{a_x} + y_j\vec{a_y} + z_j\vec{a_z}) \cdot (h\vec{a_x}^* + k\vec{a_y}^* + l\vec{a_z}^*)) \tag{2.23a}$$

$$F_{hkl} = \sum_1^N f_j cos(2\pi(hx_j + ky_j + lx_j)) \tag{2.23b}$$

This then allows us to rewrite 2.22 as eq. 2.24.

$$I_{sca} = |F_{hkl}|^2 = \sum_1^N \sum_1^N f_j f_i cos(2\pi(h(x_j - x_i) + k(y_j - y_i) + l(z_j - z_i)) \tag{2.24}$$

Thus with the atomic scattering lengths and positions of all of the scatterers within the unit cell we can find the intensity of any reflection, indexed by (hkl).

For a final note, equation 2.23(b) is the general equation for any structure factor which can then be used to find the scattered intensity at any reflection, (hkl). However, when measuring diffraction on real materials, especially in the case of thin films or superlattices, the atomic scattering lengths and exact positions within the unit cell are not typically known with much certainity. Thus, in order to understand a typical diffraction pattern, a much simpler relation is helpful to extract useful information, known as Bragg's law.

The essence of Bragg's law is to simply consider a crystal as planes of atoms, note this may contain non-equivalent atoms thus having different f but we simply ignore this

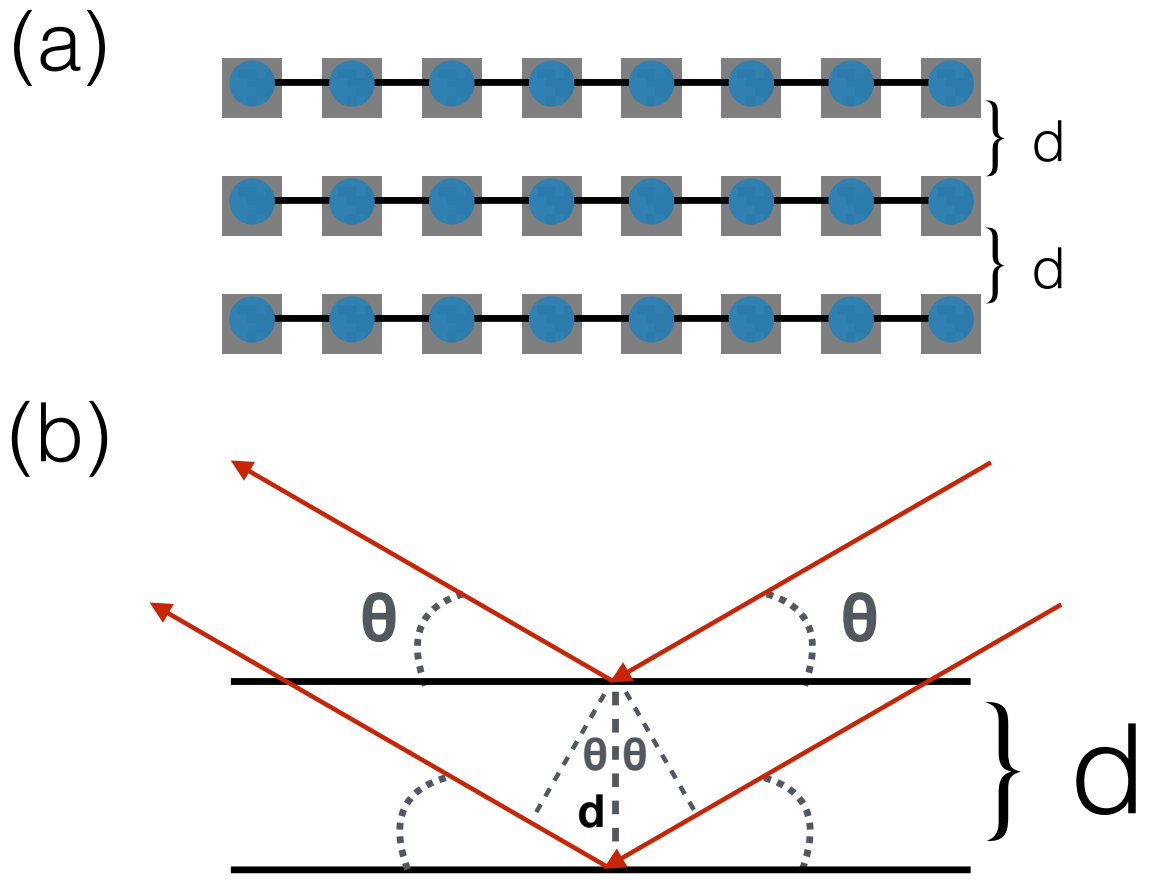

Figure 2.4: (a) Several atomic planes of a crystal separated by a distance d. (b) Reflected light, incident at angle θ above the horizontal, from two planes separated by distance d. The total path length difference is then $2dsin(\theta)$.

distinction for now, Fig. 2.4(a). We then shine monochromatic (i.e. single wavelength) light upon upon this at some angle θ above the horizontal and detect the scattered wave at θ above the horizontal. It is obvious that if there is one plane to reflect the light, the path length for light hitting any part of the crystal from the source to the detector is the same. This means the scattered light is all of the same phase, and will interfere constructively. However, as discussed previously, for a typical crystal size only 2% of the incident light is scattered, so if we consider the crystal as consisting of multiple of these planes we must consider the scattering from the layers lying below the surface. Considering just the top two layers, we can find the path-length difference for the two different scattered beams as $2dsin(\theta)$, Fig. 2.4(b). Thus the scattered beams are not guaranteed to be in-phase, and when averaged over several layers the total reflected beam goes to zero. However, if the path-length difference is an exact integer multiple of the light's wavelength then the scattered waves from each successive layer

will interfere constructively and give a reflected peak. This relation is known as Bragg's law and is typically written in the form of eq. 2.25.

$$2dsin(\theta_n) = n\lambda \tag{2.25}$$

with n integer. Thus, for a monochromatic x-ray source with known λ we can predict the angles θ_n which will give so-called Bragg peaks. Bragg's law is generally of much more utility then 2.23(b), and it will be extensively utilized throughout the thesis, however it should be noted Bragg's law can be found via 2.23(b) as they describe the same phenomena in different approaches.

2.3.2 Resonant scattering

Returning to eq. 2.6, we discussed the origin of the f_{TH} term in 2.3., and we discussed the origin of the imaginary part of the the f_{Dis} term in 2.2, which leads to x-ray absorption spectroscopy. The only remaining term, in this approximation, is the real part of the dispersion term. This term contributes what is known resonant x-ray scattering (RXS). This term depends upon the energy, E, scattering vector, $\vec{Q}$, and the polarizations $\mathbf{e}$ and $\mathbf{e}'$. As previously discussed, the exact form can be found directly via the Kramers-Kronig relation, however this method requires very detailed XAS experiments with a minimum of nine polarizations with respect to the crystal axes to determine the full resonant scattering matrix. Further insight can be gained from considering the relation between the scattering length and the index of refraction. The index of refraction may in general be written as $n(\omega) = 1 - \delta = 1 - \sigma - i\beta$. When a wave propagates in a medium with $n(\omega)$, the imaginary part leads to a exponential decay term in the wave's propagation equation, this term, β is due to absorption and is due to the imaginary part of f_{Dis} (XAS) while σ comes from the real part of f_{Dis}. Some general observations can help understand the general properties of resonant scattering[63, 64].

The Q-dependence, which can be thought of as the θ dependence, is very small for this term as the core levels that absorb the incoming light are much smaller then the outer shells which contribute to the Thompson scattering, which falls off rapidly as θ is increased. This can be simply understood by the fact that the Fourier transform of the electron density (i. e. the atomic scattering length or form factor) means the scattering from the entire electron distribution (i.e. Thompson scattering) is very narrow in reciprocal, or Q, space

whereas scattering from the core shell, having a much smaller spatial distribution, is much wider in reciprocal space. Thus higher Q-values, or equivalently higher (hkl) values, tend to be better for resolving the resonant contribution against more typical Thompson scattering. In terms of the energy dependence, as the imaginary part of $f_{Dispersion}$ has a strong response at the absorption edge, the real part, i.e. resonant scattering, also has a strong variation here by the Kramers-Kronig relation.

For the most general case the resonant scattering factor can be written as a rank 2 tensor with $N = 3$ for the three spatial dimensions, eq. 2.26, defining $\mathbf{e} \cdot f^*_{Dispersion} \cdot \mathbf{e}' = f_{Dispersion}$.

$$f^*_{Dispersion} = \begin{pmatrix} R_{xx} & R_{xy} & R_{xz} \\ R_{yx} & R_{yy} & R_{yz} \\ R_{zx} & R_{zy} & R_{zz} \end{pmatrix} \tag{2.26}$$

which reflects the fact that the polarization can be dependent on all three directions, and each of these terms has E-dependence. In a perfectly spherical charge distribution, with no magnetism, all terms except for the diagonal go to zero, and $R_{x,x} = R_{y,y} = R_{z,z}$ and we are left with simply a scalar resonant term. If we consider the perovskite unit cell typically encountered throughout this thesis, we will be interested in the TM B-site which is surrounded by an oxygen octahedra. In this case if we consider a distortion of the octahedra where along one direction the B - O bond is slightly different than the other two directions. This means that the energy dependence of the scattering factor corresponding to this direction will be slightly different, and so-called dichroic terms can arise in the matrix.

If we consider the special cases of polarizations of the incoming beam either parallel or perpendicular to the scattering plane, denoted σ and π respectively, we can then measure the polarization of the scattered beam to find the polarization dependent resonant scattering matrix, eq. 2.27.

$$\vec{S} = \begin{pmatrix} \mathbf{e}_\sigma \cdot f^* \cdot \mathbf{e}'_\sigma & \mathbf{e}_\sigma \cdot f^* \cdot \mathbf{e}'_\pi \\ \mathbf{e}_\pi \cdot f^* \cdot \mathbf{e}'_\sigma & \mathbf{e}_\pi \cdot f^* \cdot \mathbf{e}'_\pi \end{pmatrix} \tag{2.27}$$

By measuring these terms quite detailed information about the scatterer can be deduced, including charge and magnetic ordering, and the local environment. This can be useful, as often the total scattered beam cannot distinguish between these effects.

2.3.3 Experimental details

As with XAS, both soft and hard x-rays can be utilized for x-ray scattering. For hard x-ray scattering, the 6-ID-B beam line of the Advanced Photon Source utilizes a 6-circle diffractometer allowing the investigation of a very large portion of reciprocal space, i.e. both extremely small (hkl) and large (hkl), which is further expanded by the ability to change the incoming x-ray energy. Furthermore, resonant scattering is measurable by tuning to absorption edges, specifically in this thesis the Ni K-edge will be utilized.

For soft x-ray scattering, the 4.0.2 beam line of the Advanced Light Source at Lawrence-Berkeley National Laboratory allows resonant scattering at several TMO L-edges. Due to the strong air scattering of soft x-rays, the measurements must be done in-situ which presents a significant challenge for scattering measurements which require the ability to reorient the incident and exit angles of the x-rays beam, which is fixed, on the sample. Horizontal scattering chambers, such as that at the 4.0.2, allow x-ray scattering to be measured with some limitations. The most glaring issue with this technique is that the larger wavelength of soft x-rays means the extent of reciprocal space that can measured is typically very small. In this thesis, measurements on the Ni L-edge at the $(\frac{1}{4}\frac{1}{4}\frac{1}{4})$ are performed, which is possible even at this low energy, but, for example, even the $\vec{Q} = (\frac{1}{2}\frac{1}{2}\frac{1}{2})$ reflection is not obtainable.

This concludes the discussion of the synchrotron x-ray techniques utilized in this thesis, more in-depth descriptions can be found elsewhere[67].

2.4 Thin film growth

Thin films have garnered considered attention in recent decades due to the development of novel techniques to stabilize various crystals. Practically, this field is of high importance due to the ability to pattern devices on such films, but it also has significant scientific importance. Many TMOs do not easily lend themselves to single crystal growth beyond the micrometer scale resulting in polycrystalline materials, which severely hinders characterization of these materials. Beyond this, the introduction of a lattice mismatch between the grown film and material it is deposited upon, referred to as the substrate, can be utilized to modulate the material's properties, as described in chapter 4. Here, we discuss the particular thin-film growth technique utilized in the Laboratory for Artificial Quantum Materials and reveal how this technique is able to stabilize the rare-earth nickelates, whose high Ni^{3+} valence has prevented single crystal formation from being realized using more

conventional solid-state synthesis.

2.4.1 Pulsed laser deposition

With the advent of the laser in 1960, it was soon utilized as a way to deposit materials. By shining highly focused laser light on a material high energy ions are ejected from the surface, these ions can then be captured by a substrate. Initially, laser growth was not well understood and did not create films of particularly high quality. As the plume dynamics became more well understood and the availability of lasers more well-suited to the task were developed, the technique became more popular. A major paradigm shift occurred in 1987 with the creation of high quality films of the high temperature superconductor $YBa_2Cu_3O_{7-\delta}$. From there, continued advancements in laser technology, in-situ characterization tools, and a rise in popularity have elevated pulsed laser deposition (PLD) to one of the most advanced and versatile thin film growth techniques.

Pulsed laser deposition at the Laboratory for Artificial Quantum Materials uses a KrF excimer laser, with wavelength 248 nm. This beam is focused into a spot size of about 5 x 1 mm, giving an energy density around 2 J/cm^2. The laser gives pulses of about 20 ns at a repetition rate of up to 18 Hz. Typical target material is made from ceramic powder which has been pressed and sintered into a solid 1/8th inch thick disc. When the laser pulse strikes the surface electronic excitations occur within the first several femtoseconds, followed by rapid thermalization and ionization within a few thousand femtoseconds. This rapid heating creates an ionized gas which then absorbs the remainder of the laser pulse creating a high temperature and pressure plume. This process is known as ablation. The plume then interacts with the background gas pressure, which lowers the kinetic energy of the plume's ions and compensates for the loss of O that occurs during plume propagation and prevent defect formation in the film due to high energy collisions. Further, in order to obtain stoichiometric films the plume must thermalize to some degree, which the background O assists by lowering the plume's kinetic energy allowing it to interact with the background O and substrate surface. Thus the substrate to target distance, background O pressure, and laser power density can all be utilized to control the dynamics of growth to suit different materials.

When the ionized material of the plume reaches the substrate surface, several processes can occur. The dynamics of film growth are quite complex and a detailed overview of

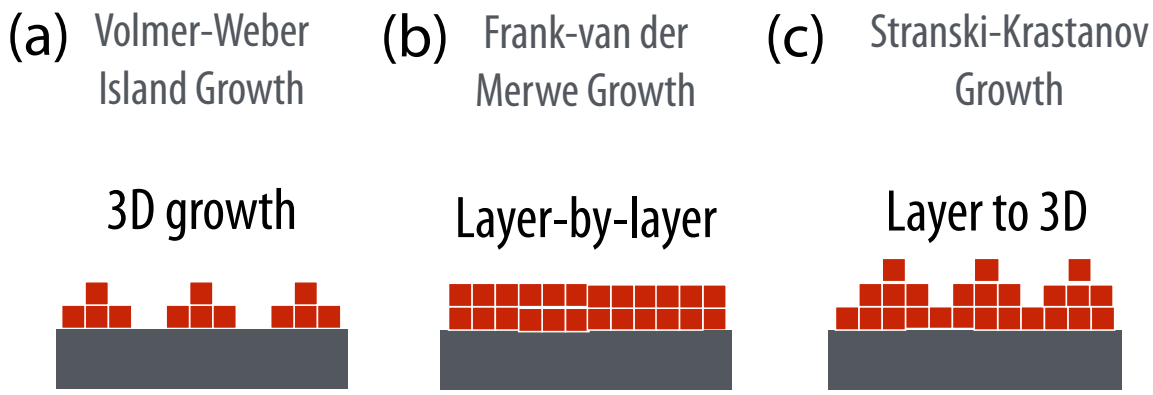

Figure 2.5: (a) Volmer-Weber island growth. (b) Frank-van der Merwe layer-by-layer growth. (c) Sttanski-Krastanov growth mode, where layer-by-layer growth give way to 3D growth at some critical thickness.

the subject can be found here[68]. From the PLD growth standpoint, we are able to control only a few aspects of this process. As previously discussed, by varying O pressure, substrate to target distance, and power density the energy of the ionized gas in the plume can be controlled. Once the deposited material, or adatoms, reach the substrate surface they can diffuse along the surface or be ejected back to the vacuum, a process called desorption. This is determined by both the energetics of the plume, and the temperature of the substrate, which determines the diffusivity of the adatoms. When the diffusitivity is very large the desorption process becomes much more favorable and stoichimetry can deviate significantly from the target. When the diffusitivity is within a certain threshold, which is different for different materials, the ionized materials will remain on the surface and be mobile, allowing them to be captured at energetically favorable sites. The substrates used for this growth are typically cut so that the surface is the psuedcubic (001) plane, however there is always some miscut angle due to the inability to perfectly cut along the surface. Thus, the substrate surface consists of terraces whose edges are separated by a distance $D \simeq \frac{c}{\sigma}$, with c being the lattice constant in the (001) direction and σ being the miscut angle (typical values in perovskites of c = .38 nm, $\sigma = 0.3°$, giving a terrace separation of 1.3 nm). At these edges, the increased density of the unoccupied sites available to the adatoms are energetically favorable and can lead to thin film growth along the edges of the terraces. This is known as the step-flow growth mode and it is common for several materials[69].

When the diffusitivity is too low to freely move across the entire surface several different growth modes are possible, Fig. 2.5. The key to these modes is that initially island formation is more energetically favorable then step-flow. When this occurs a characteristic spacing λ is found between the nucleation sites, which must be smaller then D, the spacing between terraces, otherwise step-flow would occur. When the adatoms nucleate at random sites the further adatoms can then attach to these sites. This leads to three-dimensional island formation, or Volmer-Weber island growth. This occurs when the adatom - adatom interaction is strong compared to the adatom - substrate interaction. When the adaptor - substrate interaction is stronger, Frank-van der Merwe layer-by-layer growth can be achieved. In this mode the additional adatoms prefer to attach to the substrate, and as long as the diffusion is sufficient, they will eventually form a single monolayer. An extension of this mode, Stranski-Krastanov, growth occurs when layer-by-layer growth is initially achieved, but after a characteristic number of layers three-dimensional island growth becomes favorable. This is typically due to the substrate-induced strain on the film, which can make non-strained island growth more favorable.

The Laboratory for Artificial Quantum Materials specializes in utilizing the relatively new layer-by-layer (LBL) growth mode, also known as "interrupted" deposition. While this mode can be achieved by a constant flux of adatoms for some materials, for the sometimes highly thermodynamically unstable oxides an interrupted LBL is often favorable[70]. The essence of this process is to very rapidly ($<$ 1s) deposit enough adatoms to form one unit cell of the material, followed by an interruption of typically $\sim$ 60 s to allow the thermal diffusion to anneal and fill in any gaps not filled during the deposition period. However, in-between pulses when an entire layer is not yet formed, this same diffusion will allow these well distributed islands to migrate and form larger islands with larger separation[71]. Then adatoms deposited in subsequent steps are more likely to form new nucleation sites on top of the existing larger islands, as the density of step-edges is strongly decreased. Thus, the unit cell layer must be deposited as quickly as possible, typically a repetition rates of 18 Hz is utilized. Then the extended annealing time allows any adatoms deposited on top of large islands to diffuse to fill in the gaps and create one continuous layer.

2.4.2 Reflection high energy electron diffraction

As discussed in the previous section there are multiple control parameters within PLD and multiple growth processes that can occur. Material properties can depend strongly on the type of growth mode and chemical phase, or phases, stabilized. Thus in-situ monitoring of the growth is essential for ensuring quality and consistency. The first real *in-situ* monitoring tool for thin film growth, reflection high energy electron diffraction or RHEED, was developed for molecular-beam epitaxy chambers in 1969 by Arthur and LePore for GaAs[72]. Since then it has become a key tool for thin film growth in MBE. In PLD the development was hindered by the need for background O during growth, as RHEED requires high vacuum to operate. The advent of the high pressure (HP) RHEED system, which utilizes a double differential pumping to maintain high vacuum at the RHEED system while exposed to the growth chamber, brought this highly valuable growth tool to PLD systems.

As a diffraction technique, the same general ideas from section 2.3 still hold. The difference here is the incident beam consists of electrons, with an energy of 25 keV giving a relativistically corrected de Broglie wavelength of $\lambda = \frac{h}{\sqrt{2m_0eU}} \frac{1}{\sqrt{1+\frac{eU}{2m_0c^2}}} = 0.0766$ Å, which is much less then lattice spacings in crystals. This means that very low angles can be used, due to $\frac{\lambda}{d} \ll 1$. The low angle and very shallow penetration depth of electrons in a crystal, typically of the order of several Angstroms, makes RHEED a very surface sensitive technique. Likewise the diffraction is essentially two-dimensional, which means the conditions in eq. 2.18 are reduced from three to two, and we only require two cones to intersect instead of three. This reduction allows the simplified use of the Ewald's sphere construction, in which we define a sphere with radius $\left|\vec{k_i}\right|$, the wave vector of the incident electrons, and represent the reciprocal lattice as a series of rods along the $\vec{k_z}$ direction, instead of discrete points as in the three-dimensional case discussed in 2.3. When these rods cross the Edwald sphere, a diffraction peak is obtained, as then $\left|\vec{k_f}\right| = \left|\vec{k_i}\right|$ and $\vec{Q} = \left|\vec{k_f}\right| - \left|\vec{k_i}\right|$, i.e. the elastic scattering condition is satisfied. $\vec{Q}$ then links two crossings of the Ewald's sphere, i.e. two reciprocal lattice points. This ensures that $\vec{Q}$ is itself a reciprocal lattice vector, as we know from section 2.3 that we define $\vec{Q} = h\vec{a}_x^* + k\vec{a}_y^*$, with h and k integer, thus subtracting any two reciprocal lattice vectors will give another reciprocal lattice vector.

Periodic rods crossing a sphere create circles of intersections called Laue zones. The lowest lying, or smallest $\vec{Q}$, of these is referred to as the 0th Laue zone. Each subsequent circle, as $\vec{Q}$ is increased, is then labeled as the next integer. The scattering crystal is typically

oriented so that the incident beam lies along a reciprocal lattice vector, so that we can denote the peaks as in Fig. 2.6(b). However, while when dealing with x-rays we were able to assume the kinematic approximation owing to $I_0 \gg I_{scatt}$. Due to the much stronger interactions of the incident electrons with the crystal, this approximation is no longer valid and dynamical scattering effects occur, such as Kikuchi lines and I_{sca} is no longer as simple as was found for section 2.3. Thus extracting quantitative data from RHEED requires advanced modeling and is beyond the scope of this thesis. Despite this, RHEED is still a powerful *qualitative tool* for growth monitoring and sample quality comparisons.

In order to detect the reflections, a phosphorus screen, shown in 2.4(a), is used, which fluoresces when impacted by the scattered electrons. By using a large screen, ~ 3 inches in diameter, the entire 0th Laue Zone can be measured. Depending on the geometry of the setup higher order Laue Zones can also be measured, however in HP-RHEED the lower intensity of these peaks coupled with the strong diffuse scattering due to the background pressure required for growth precludes practical use of the peaks. A KSA digital camera then records the image in real-time, allowing the changing intensity of the reflections to be analyzed during growth. This specular intensity was found to give periodic oscillations which coincided with the number of GaAs monolayers[73]. With MBE, the constant flux of deposited material gives a damped oscillator pattern. With PLD, due to the flux of material being a function of laser pulses, this cannot be exactly replicated, but slow repetition rates (typically 2-4 Hz) give similar results. With high repetition rates such as those used at the Laboratory for Artificial Quantum Materials, the oscillations are very different, as shall be demonstrated in the next section.

The pattern given by a typical growth is shown in the next section, but several other patterns can emerge due to various deviations from the preferred layer-by-layer growth. As mentioned previously, if step-flow growth becomes preferable, the RHEED pattern does not oscillate and the ability to directly monitor each layer is lost. Further, a smearing of the diffraction spots into streaks indicates high levels of defects which causes the correlation length to decrease, as a single continuous surface is no longer the source of the diffracted electrons. If either Volmer-Weber (3D islands) or Stranski-Krastanov (3D islands after N 2D layers) occurs, the electrons will be transmitted through the islands, which have a width less then the penetration depth, and give a transmission pattern which appears as a regularly spaced 2D array of spots.

In the following sections, the techniques discussed thus far in this chapter are applied

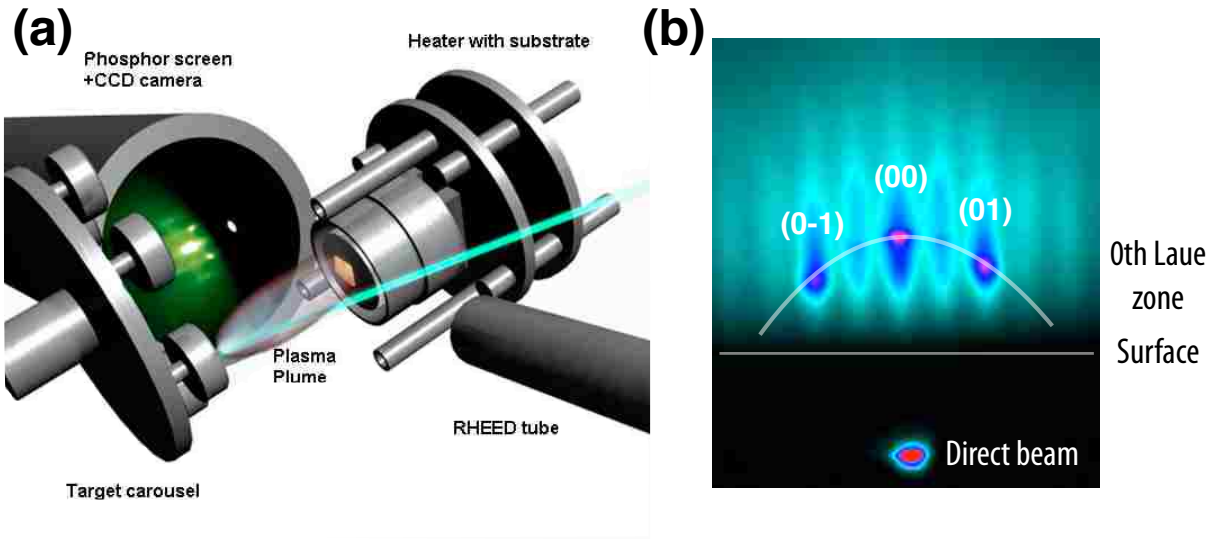

Figure 2.6: (a) In-situ PLD setup. The pulsed laser, cyan line, ablates the target creating a highly ionzed gas plume which is then incident upon the substrate. The RHEED gun and screen sit at grazing incidence to the substrate surface. (b) A post-growth RHEED image for $EuNiO_3$ sample. The 0^{th} Laue Zone is resolved with the (00), (01), and $(0-1)$ reflections labeled. The bright spot at the bottom of the image is the direct beam that bypassed the sample surface.

to the growth of rare-earth nickelates, most of which have never been stabilized in single crystal form previously.

2.4.3 Epitaxial synthesis of $EuNiO_3$

The following section is adapted from our publication found in Ref. [74].

From the growth perspective, owing to the low thermodynamic stability of the nickelates, conventional solid state chemical synthesis requires very high oxygen pressure and temperatures and yields only micron sized single crystals [5, 33, 75]. This has severely limited our understanding of the physics of these interesting compounds. Due to the lack of macroscopic size crystal growth, thin film synthesis is a promising avenue to overcome this obstacle. However, even in the thin film form these materials have thus far proven difficult to fabricate in a layer-by-layer fashion, becoming arduous upon application of strain[35]. Several recent publications detail the attempted growth of thin film nickelates by metal-organic chemical vapor deposition and sputtering[76, 48, 49]; for example, thick (∼210 nm) ENO films have been grown by rf magnetron sputtering resulting in an essentially textured

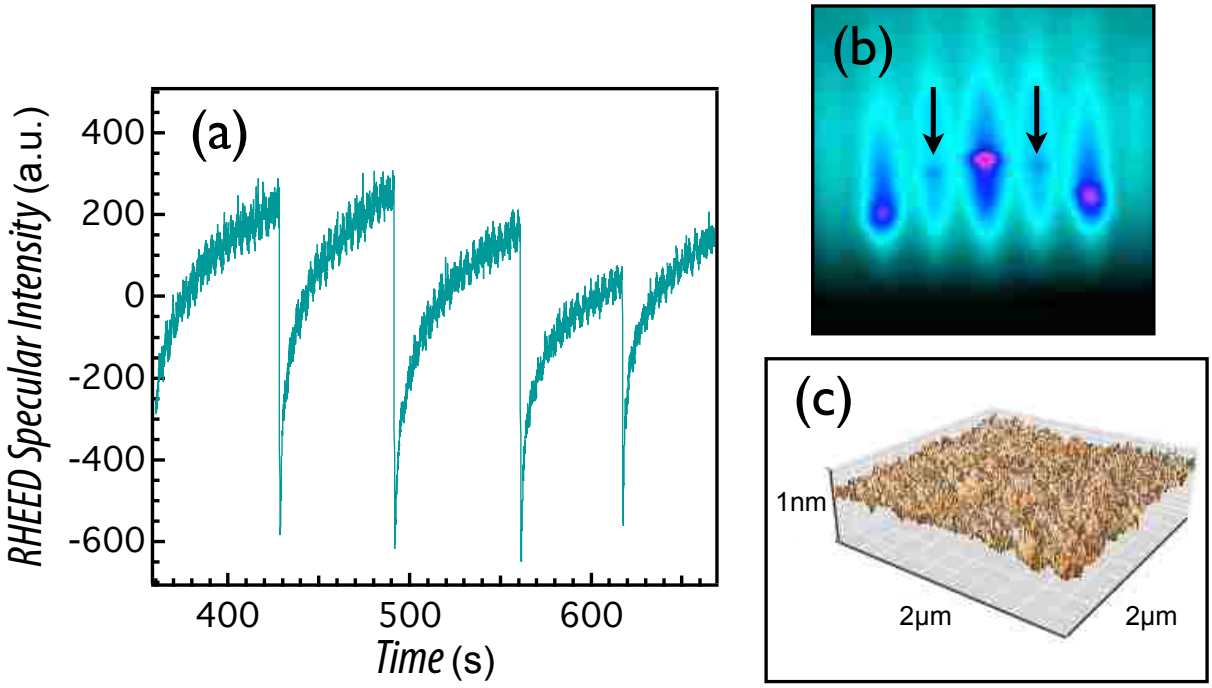

Figure 2.7: (a) RHEED specular intensity taken during growth of 15 uc ENO on YAO. (b) RHEED pattern of the 0th Laue circle on the same ENO sample, black arrows indicate the half-order peaks. (c) AFM image for same sample.

morphology[77] likely due to the relatively large size ($\sim$ 210 nm).

Here, we report on our results of the growth of high quality, fully strained ultrathin films (15 unit cells (uc) or 5.86 nm) of ENO on $YAlO_3$ (YAO) substrates grown in a layer-by-layer mode in order to epitaxially stabilize the nickelate films. Several characterization techniques revealed high quality, epitaxially strained ultra thin films of ENO were obtained for the first time to the author's knowledge.

ENO (bulk lattice constant (BLC) = 3.80 Å) was grown on YAO (110) oriented, BLC = 3.71 Å; lattice mismatch -2.4%) by interrupted pulse laser epitaxy method using a KrF excimer laser (λ = 248 nm) with rapid pulse cycling of 18 Hz with typical pulse trains of 18 shots ($\sim$ 1 s per unit cell); details of this growth mode can be found elsewhere[78, 70]. This approach allows for layer-by-layer growth which was confirmed by the presence of sharp specular intensity drops (during the pulse train) followed by total recovery monitored in-situ by high pressure reflection high energy electron diffraction (HP-RHEED). After deposition films were annealed in 1 atm of ultra-pure oxygen for 30 minutes. The conditions best suited for layer-by-layer growth and high morphological quality for ENO were found to be $\sim$ 610

°C, P_{O_2} = 100 $\sim$ 150 mTorr, and a laser power density varied between 2.2 $\sim$ 2.4 J/cm^2. The film quality was investigated with reflection high energy electron diffraction (RHEED), atomic force microscopy (AFM), X-ray diffraction (XRD), reciprocal space mapping (RSM), and synchrotron based resonant X-ray absorption spectroscopy (XAS).

Fig. 2.7(a) shows the characteristic time dependent specular intensity. As seen, during the rapid pulse sequence (typically $\sim$ 1 second) the RHEED intensity sharply drops and then rapidly recovers within a prolonged dwell time, characteristic of layer-by-layer growth. The lack of significant overall dampening of the intensity after multiple layers attests to the high quality of the growing layers. The electron diffraction pattern was taken after annealing to ensure proper morphological quality, and is shown in Fig. 2.7(b). The specular, (0 0), and off-specular, (0 1), (0 -1), and half order (indicated by arrows), (0 $\frac{1}{2}$), (0 -$\frac{1}{2}$), Bragg reflections are evident with a streaking pattern characteristic of excellent surface morphology. The half-order peaks are due to the expected structural distortion of the orthorhombic structure[79]. For films of such small thickness, $\sim$ 6 nm, AFM imaging is necessary to confirm the sample has grown with a uniform surface, as any deviation from 2D growth will lead to a drastically higher surface to volume ratio which could have an adverse effect on materials properties. Fig. 2.7(c) displays a 2 x 2 μm^2 AFM scan, showing the high morphological quality of these films, yielding an average surface roughness of $<$ 0.7 Å, well below the 3.8 Å BLC.

In addition, the structural properties were investigated by x-ray scattering in the X-ray Diffraction Facility at Northwestern University using Cu $K\alpha_1$ focused radiation with a 4-circle diffractometer; Fig. 2.8 displays the X-ray diffraction along the (00L) crystal truncation rod obtained in the vicinity of the YAO (220) Bragg peak. The sharp peak at Q_z = 3.384 Å^{-1} is the YAO (220) substrate Bragg peak and the broad feature at Q_z = 3.24 Å^{-1} is the (220) peak for the ENO film. The analysis of the Bragg peaks from the ENO epitaxial film yields the c-axis lattice constant of ENO to be 3.878 Å; in very good agreement with the expected tetragonal expansion from the bi-axial strain and confirms the 15 uc thickness, corroborating the RHEED intensity oscillations for layer-by-layer growth (15 pulse trains yielding 15 dips and subsequent recoveries were observed). Additionally, thickness fringes testify for the excellent flatness of the film interfaces and confirm the thickness calculated from the Bragg peak. The reciprocal space map around the off-specular (103) Bragg intensity for the film and the substrate is also shown in the inset of Fig. 2.8. The position of the weak ENO (103) peak relative to the YAO (103) peak confirms that the ENO epitaxial

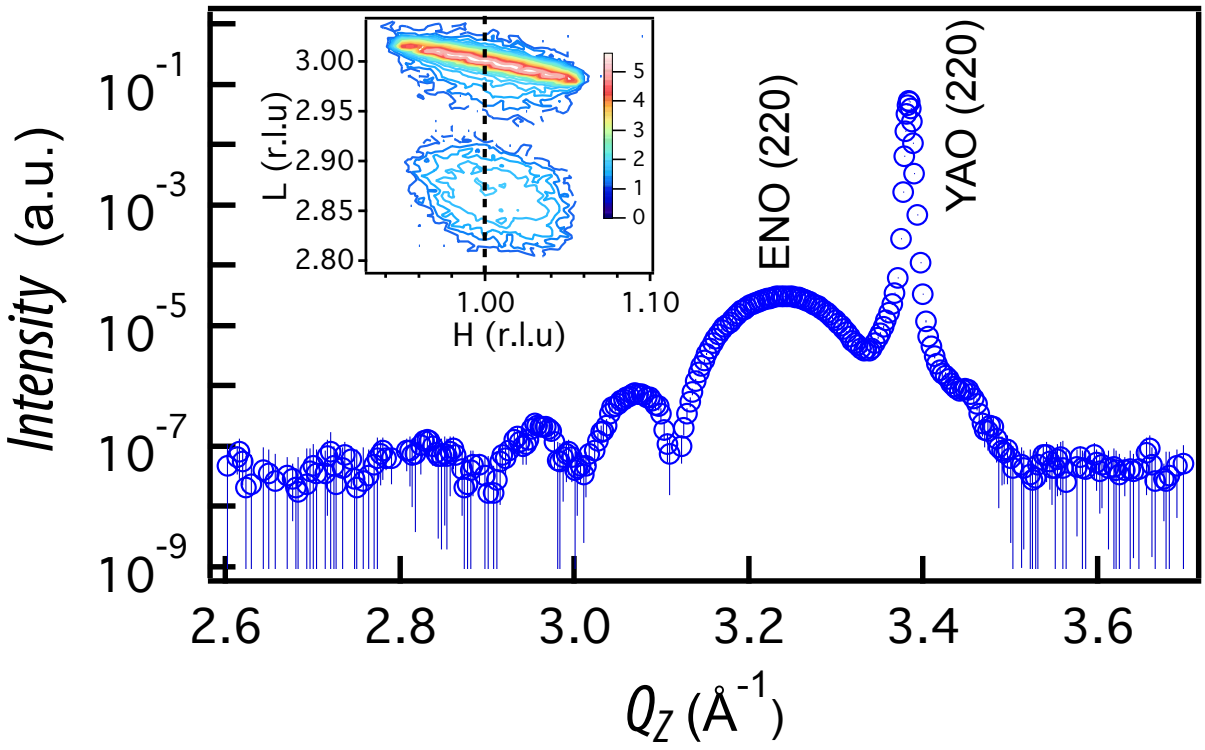

Figure 2.8: XRD around the (002) truncation rod of YAO. ENO film peak with thickness fringes is present at lower Q_z. Inset displays the RSM around the (103) truncation rod, showing the film is fully coherent with the substrate.

thin film is coherently strained to the substrate. XRD survey scans did not reveal the presence of any impurity peaks, such as the typically problematic and thermodynamically more stable NiO (not shown). However, for such thin films detection of a small amount impurity, especially considering it has no reason to preferentially oriented relative to the substrate, is very difficult. In order to confirm the lack of NiO impurity and confirm the Ni 3+ valence necessary for material properties spectroscopic measurements were needed.

To investigate the electronic and chemical structure of these films, XAS measurements on the Ni L-edge were obtained in both total electron yield (TEY) and total fluorescence yield (TFY) modes in the soft X-ray branch at the 4-ID-C beamline at the Advanced Photon Source in Argonne National Laboratory. The penetration depth of x-rays in TEY mode ($\sim$ 12 nm) is larger then the film thickness ($\sim$ 6 nm) allowing it to be used with ambiguity between the surface and bulk signal. The results of the experiment are shown in Fig. 2.9 along with absorption on the reference bulk NNO powder. As seen, the line-shape and position of the Ni L_2-edge located at 870.5 eV very closely resembles that of the NNO powder, which shares the Ni 3+ state, testifying that the 3+ valence state of Ni was obtained, confirming that the

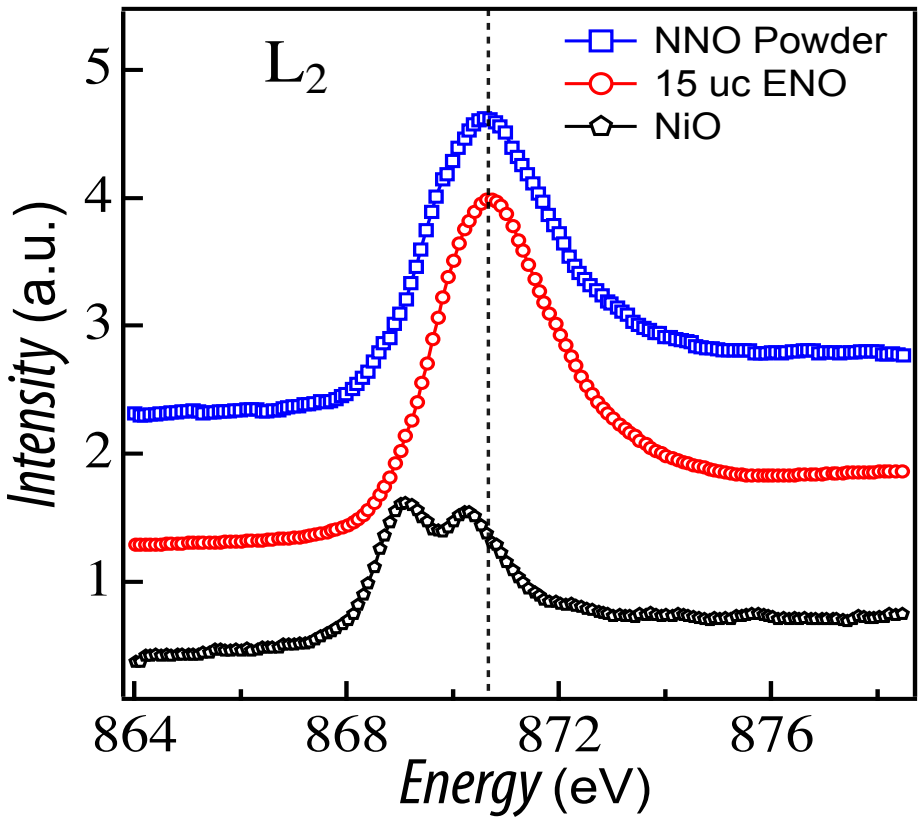

Figure 2.9: XAS data for ENO sample along with NNO bulk powder and a NiO reference. The strong white line around $\sim$ 871 eV indicates Ni 3+ was obtained. NiO, featuring Ni 2+, shows a very dissimilar line shape with a strong peak occurring around $\sim$ 869 eV.

proper ENO stoichiometry crucial for materials quality was achieved[80]. This measurement also excludes the possibility of any low concentration NiO impurity phase not detectable by XRD, as the Ni valence is 2+ in this state which would give a separate peak shifted to lower energy on the L_2-edge with a characteristic multiplet structure, a reference NiO is shown. This confirms ENO films with the required Ni 3+ valence and with an absence of the problematic NiO impurity phase were obtained.

In conclusion, ultra thin ENO films were grown via pulsed laser deposition on YAO substrates. Several characterization tools, including RHEED, AFM, XRD, RSM, and XAS were used to investigate sample quality. These measurements revealed the samples exhibited high morphological quality, high structural quality, full epitaxial strain, proper stoichiometry, and no impurity phases. The ability to grow the more highly distorted nickelates opens a promising avenue in the study of the physics of the correlated oxide nickelates, allowing

separate study of the MIT and AFM, thus disentangling the spin and charge ordering.

2.4.4 General trends in epitaxial synthesis of $RENiO_3$

In the previous section we discussed the specific case of ENO growth. Our group had previously succeeded in stabilizing both $LaNiO_3$ (LNO) and $NdNiO_3$ (NNO) ultra thin films. After establishing the growth conditions of ENO and comparing with the corresponding conditions for LNO and NNO some important relations were found. Within PLD, there are several tunable conditions that can be controlled, namely background oxygen pressure, substrate temperature, and energy density of the laser. While for all nickelates grown a background O_2 pressure of 50 - 150 mTorr and a laser energy density around ~ 2.4 J/cm^2 gives good results, different substrate temperatures were required to stabilize different RE ions. In fact, when these temperatures were compared an interesting dependence was uncovered. The following can also be found on the archive[81].

Further insight can be gained from the comparison of the optimal temperatures to the Goldschmidt tolerance factor ($t = [r_A - r_O]/[\sqrt{2}(r_B - r_O)]$, where r_A is the rare earth ionic radius, r_B is the transition metal ionic radius, r_O is the oxygen ionic radius) for several members of the rare-earth nickelate family (A = La, Nd, and Eu)[5]. For perovskites, the tolerance factor, t, is a measure of structural distortion. As seen in Fig. 2.10(a), graphing these three temperatures vs. the tolerance factor revealed a surprisingly linear trend. The linear fit yields the scaling factor $\Delta T/\Delta t \sim 2166$ °C. The cone in Fig. 2.10(a) represents an approximate range of empirical uncertainty showing the range of growth temperatures that can be varied without completely degrading film quality. To verify the significance of the the scaling dependence, we synthesized films of PNO based on the tolerance factor, marked as a red circle in Fig. 2.10(a). A combination of RHEED, AFM, and XRR showed that high quality films were obtained. As a further test we synthesized one of the most distorted members of the family, YNO, from a target composed of NiO and Y_2O_3 precursor materials at the growth temperature specifically *predicted* from Fig. 2.10(a) (~ 565 °C). The resulting films demonstrate the same high morphological quality as the rest of the rare-earth nickelate family of materials. The supporting AFM and RHEED data are shown in Fig. 2.11(a-h).

In order to explain this empirical trend, we consider the model of epitaxial stabilization of thin films[35, 82]. In this phenomenological framework, the relative difference

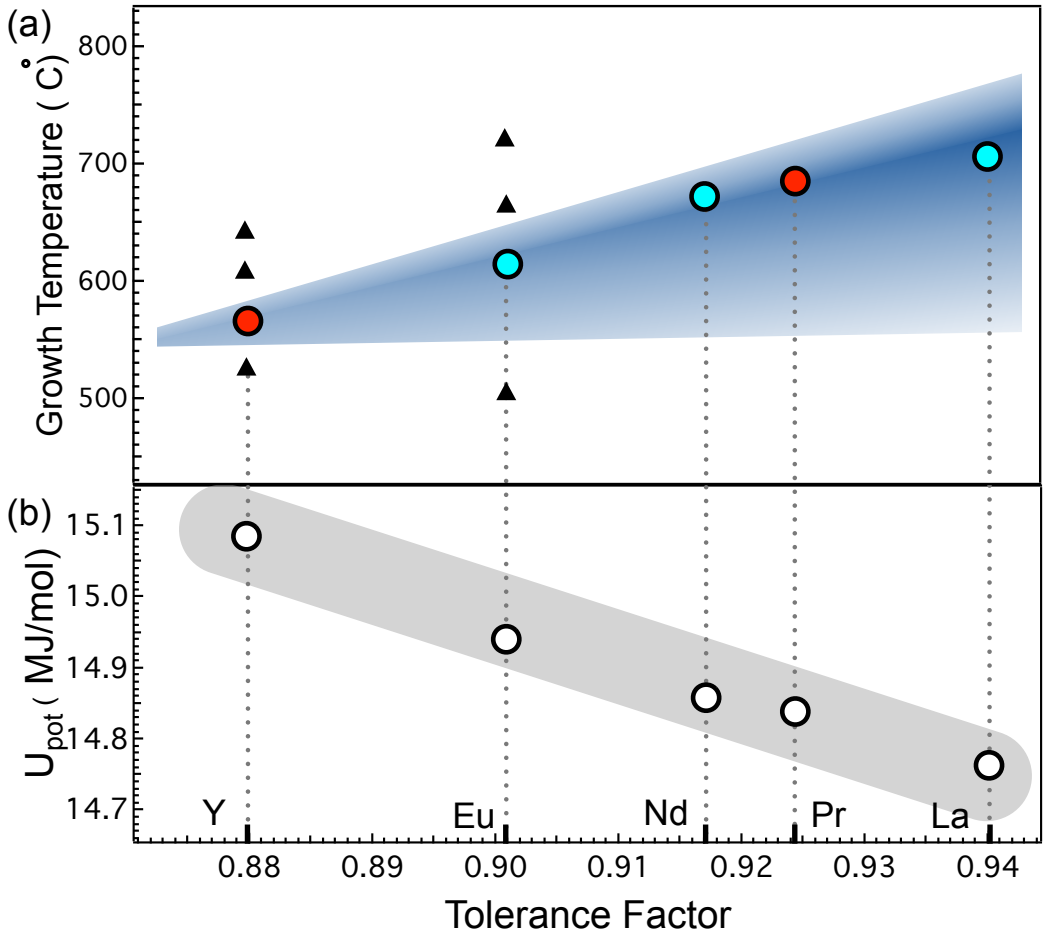

Figure 2.10: (a) Dependence of growth temperature on tolerance factor for nickelates, the dots (green) indicate the data used to obtain the trend, while the red dots were used to synthesize PNO and YNO films. Black triangles signify films grown outside the window. (b) Lattice energies vs. tolerance factor calculated.

between the energies for the relaxed and epitaxially stabilized phases is given by:

$$\Delta G''_f - \Delta G'_f = \Delta G = h[(\Delta g''_v - \Delta g'_v) - \frac{\mu}{1-\nu}\epsilon^2] + [\sigma''_s - \sigma'_s] \tag{2.28}$$

where $''$ and $'$ indicate the relaxed and epitaxial phases respectively, h is the film thickness, Δg_v is the Gibb's free energy per unit volume, μ is the shear modulus, ν is the Possion's ratio, ϵ is the lattice mismatch, and σ_s is the surface tension. Eq. (1) can be further simplified given that (i) all the rare-earth nickelates have the same relaxed chemical phase (i.e. $2RNiO_3 \rightleftharpoons 2NiO + R_2O_3 + 1/2O_2$) implying that $\Delta g''_v$ is practically constant across the series, (ii) so is σ''_s because $\sigma''_s \gg \sigma'_s$, and (iii) the third term is negated by the appropriate lattice mismatch. Under these assumptions Eq. (1) simplifies to: $\Delta G(T,t) \approx A - \Delta g'_v(T,t)$, where A is constant with respect to temperature and tolerance factor. This behavior is naturally

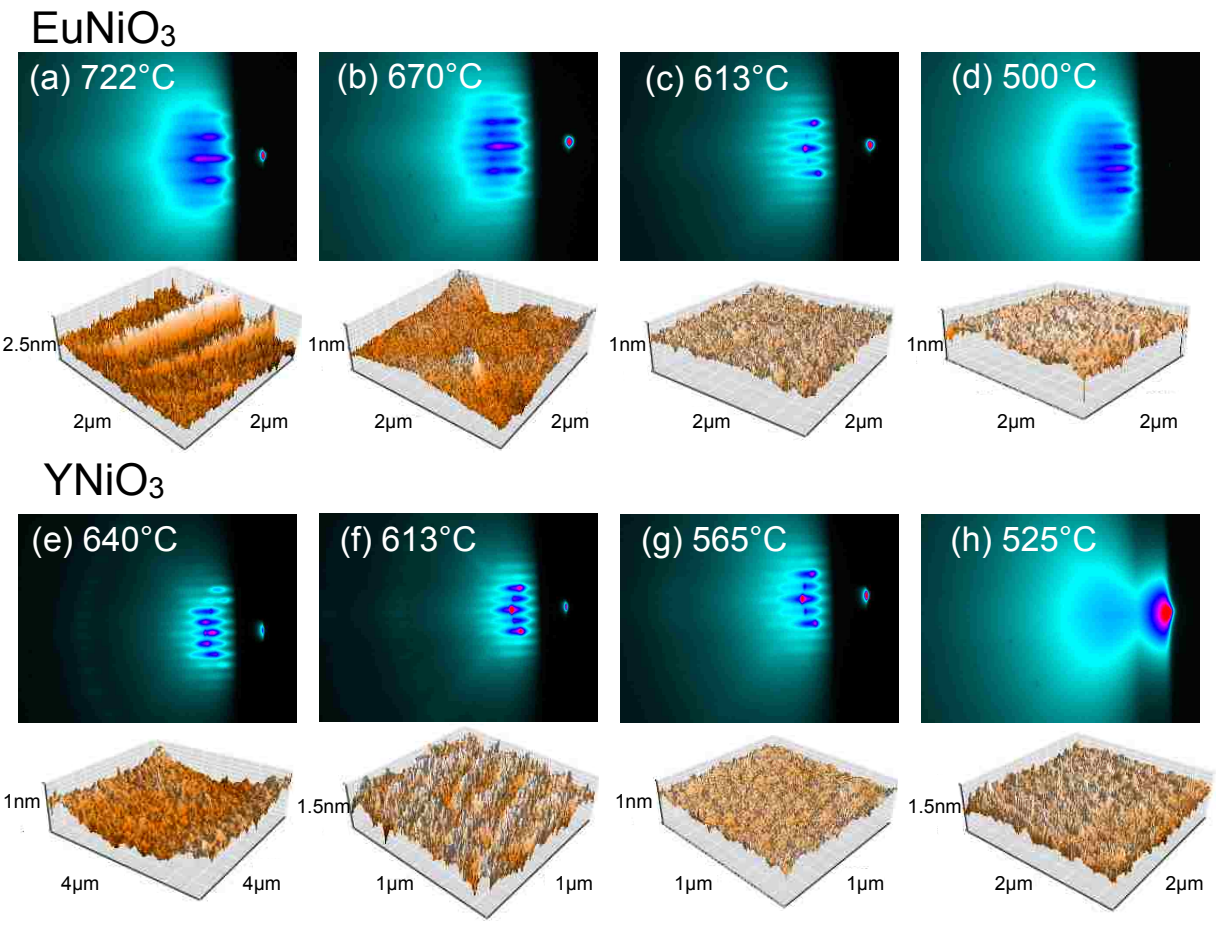

Figure 2.11: (a-d) RHEED and AFM images for ENO at various temperatures. (e-h) RHEED and AFM images for YNO at various temperatures.

related to the observation that as the tolerance factor is reduced the total energy of the lattice increases because of the reduced symmetry in cation-anion bond positions; the calculated lattice energies, U_{pot}, plotted against tolerance factor are shown in Fig. 2.10(b)[83]; this in turn raises the magnitude of $\Delta g_v'$[84].

To understand the relationship between the growth temperature and the tolerance factor, we plot $\Delta g_v'$ vs. T for several representative films of the family using the linear dependence of the Gibb's energy on T [see Fig. 2.12][85]. This also implies that there would be some T dependence for $\Delta g_v''$, but due to the supersaturation being greater for the perovskite phase, it can be disregarded. As seen, increasing the tolerance factor shifts the phase line lower (due to the lower lattice energy), which in turn causes an increase of the critical temperature T^* at which the transition from epitaxial to relaxed phases occurs. Each nickelate will then have the specific temperature, T^*, above which the perovskite

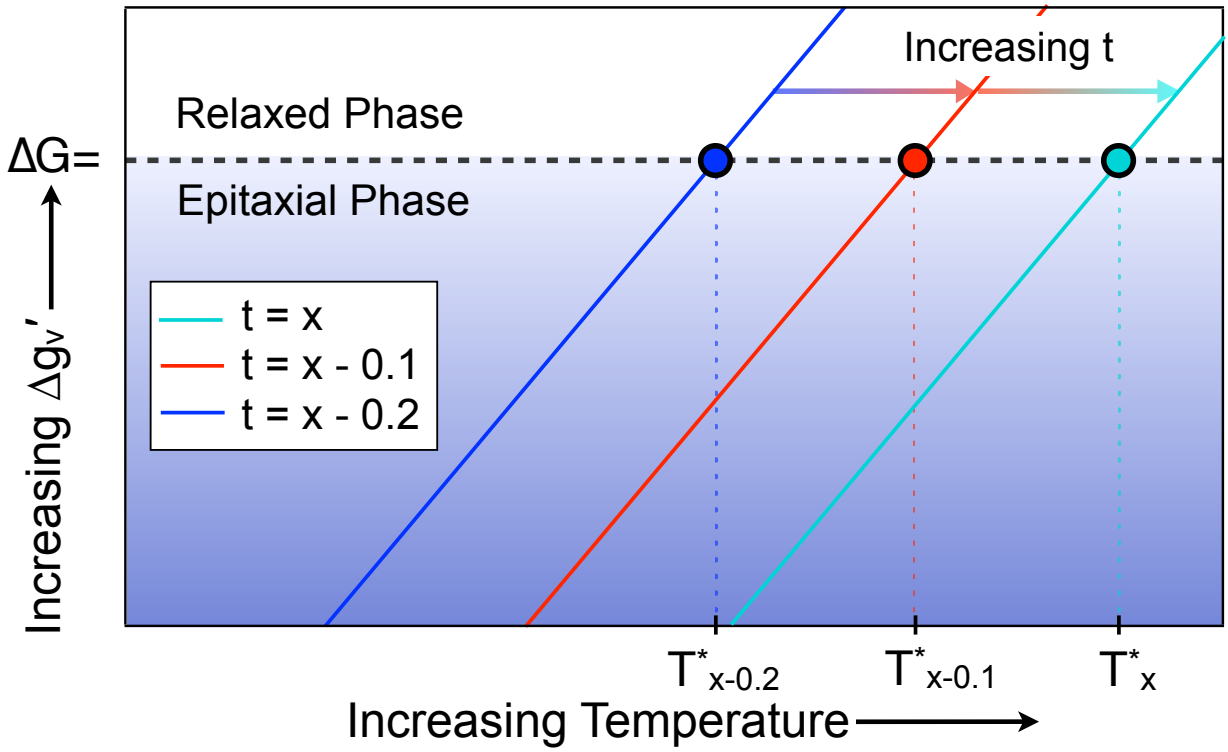

Figure 2.12: Gibb's volume energy versus growth temperature showing the increase in cut-off temperature as tolerance factor is increased.

phase is chemically unstable (approximated by the top of the cone in Fig. 2.10(a)). The final consideration is the adatom diffusion $D(T)$; as the temperature is lowered the diffusion is exponentially retarded leading to further increases in surface roughness (approximated by the bottom of the cone, Fig. 2.10(a))[70]. The combination of these factors rationalizes the existence of a set of optimal growth parameters within a progressively narrowing window below T^*.

To summarize, investigation of the growth temperature as a function of the tolerance factor for several nickelates revealed a surprising linear trend that was used to *predict synthesis conditions* for PNO and YNO films. This scaling behavior was explained in terms of epitaxial stabilization in good agreement with the empirical observations. These findings are certainly not restricted to rare earth nickelates and could be applied to growth of other perovskite-structured families of materials.

3 Anomalous magnetic and charge states in $(CaCu_3)B_4O_{12}$: Isostructural doping

3.1 Introduction

The original method for engineering the phases of a given material which is still the most popularly utilized method today, chemical doping. This has lead to the discovery of many exciting novel phases of matter. The most famous of which is high temperature superconductivity (HTSC). Historically, by creating the doped compound $Ba_xLa_{5-x}Cu_5O_{5(3-y)}$ (BLCO), it was found that the material has a superconducting transition around 30 K[6]. This was the first emergence of the type-2 HTSCs, and lead to an enormous field of research that has seen continued expansion to low dimensional materials including the Iron-penticide superconductors, heavy-fermion materials, etc[6, 7, 8, 9, 86]. However, the bulk of the research in this area still revolves around the cuprates, materials incorporating Cu in the perovskite lattice, and, specifically, $YBa_2Cu_3O_{7-\delta}$ (YBCO; T_c = 93 K)[86, 87]. This is due to many factors, but a large motivator and source of applied interest has been in the application of superconductors with a T_c above the liquid nitrogen temperature (77K). Due to the abundance of nitrogen in the air and the relative ease of cooling it to achieve the liquid state, high T_c superconductivity in YBCO has found numerous practical applications heavily utilized today. While this practicality was a huge leap forward, numerous issues still exist. Liquid nitrogen is relatively cheap, but the need for the proper equipment to utilize it, the continuous cost of upkeep and resupply, and the costly result when a system malfunctions has severely limited potential applications. In order to truly revolutionize the future of HTSC in electronics and everyday applications a material must be found that exhibits a T_c above room temperature[87].

At the same time, despite the decades of intense research in this area the microscopic mechanism of HTSC is still unknown, while numerous theories have been proposed, none have been accepted as the final theory of HTSC[86]. In fact, most of HTSC known today were created essentially from best guesses and rough "recipes" for HTSCs. This has lead to relative stagnation, as the highest known T_c rose steadily through the late 80's and early 90's, but very slowly over the past several decades[6, 7, 8, 9]. Due to the rise of various new physical properties investigative techniques and the advancement and improvement

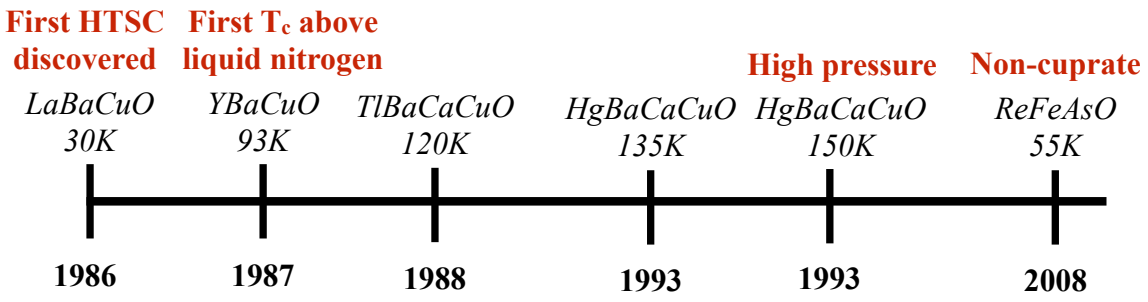

Figure 3.1: Timeline of the progress of increasing T_c in HTSCs. As can be seen, since 1993 no increase in T_c has been made, despite the advent of several new HTSC materials [6, 7, 8, 9].

of previous techniques, a new push towards more precise understanding of the microscopic mechanism leading to HTSC has been pursued. To this end, a novel type of TMO perovskite material has been synthesized with a unique structural motif. Known as the A-site ordered perovskites (AOPs), these materials feature Cu in the A-site and another TMO in the B-site, as previously discussed in Section 1.2. This is not a new concept, as similar results can be had via traditional chemical doping in ABO_3 pervskites via B-site doping, i.e. $AB_xCu_{1-x}O_3$. The issue arises in the effect of random doping of impurity atoms, as structural changes with accompanying crystalline defects are common. In this respect, the AOP materials have the unique property of having a constant structural symmetry no matter what TMO is placed at the B-site, as discussed in 2.2.1. This in turn enables a vast array of interactions which can be well understood without interference from structural effects. With the Cu valence playing an integral role in HTSC, these materials allow another dimension to further understand the microscopic mechanism behind this scientifically and technologically important phase.

For this investigation we were provided AOP ceramic samples synthesized by J. G. Cheng, J. S. Zhou, and J. B. Goodenough of UT Austin utilizing Cr, Co, Rh, and Ir at the B-site. This gave us an ideal set of samples including: two materials with 3d TMOs at the B-site which have been well-studied in their typical perovskite form (ABO_3) and they span the 9^{th} column of the periodic table (Co, Rh, Ir) allowing isoelectronic investigation with the only change being the n value of the orbitals (n= 3, 4, 5). We began with the $n = 3$

(Cr, Co) materials.

3.2 Zhang-rice physics and anomalous copper states

3.2.1 Valence states on TMO ions

The following section was rewritten from our publication[10].

While changing the B-site ion does not change the crystal symmetry of these materials, it does have a profound effect on the overall electronic structure. As previously mentioned, the chemical state and planar (2D) coordination of Cu is extremely important to superconductivity, as the superconducting carriers are a combination of the doped holes on O and the d^9 electron of Cu (coupled anti-ferromagnetically). XAS is an extremely effective technique for determining valence of individual ions, as it will observe all possible transitions around an absorption edge making it particularly effective at identifying mixed valencies. Indeed, extensive work was done on the HTSC cuprates due to the mixed valency of the Cu and O ions. Thus, we began our investigation of these compounds with this technique.

For the B = Cr and Co materials the absorption edges we are interested in are all within the soft X-ray energy range (Cu; 920 - 960 eV, O; 520 - 560 eV, Cr; 570 - 600 eV, Co; 770 -810 eV), thus we acquired time at the 4-ID-C beam line of the Advanced Photon Source at Argonne National Laboratory. This beamline has a usable energy range from 400 eV to 2500 eV which easily encompasses the O K-edge and the Cu, Cr, and Co L-edges.

Fig. 3.2 displays the results of these measurements on the B = Cr and Co AOPs for the Cu L and O K edges. For clarity, reference samples of YBCO (Cu^{2+}) and $LaCuO_3$ (LCO; Cu^{3+}) were also measured and graphed alongside. These compounds contain Cu 2+ (majority d^9 configuration) and Cu 3+ (majority $d^9\underline{L}$, where $\underline{L}$ refers to a doped ligand hole on O) respectively, allowing comparison for the AOPs. As can be seen in the left panel of Fig. 3.2, the change in B-site ion had a significant effect on the Cu valency. The white line for LCO and $CaCu_3Co_4O_{12}$ (CCCoO) at $\sim$ 932 eV corresponds to the Cu $d^9\underline{L}$ state, ionically Cu 3+. A small peak appears as a low energy shoulder on the white line, which corresponds to the Cu d^9 state (discussed below). A dotted line spectrum here represents the original raw data, which contains a significant peak at around 928 eV. This peak is due to CuO impurities left over from the synthesis, and was subtracted for clarity. Several previous studies have shown similar results, and this peak, which also represents the Cu d^9 state can be easily distinguished from the Cu d^9 state in CCCoO due to the very significant difference

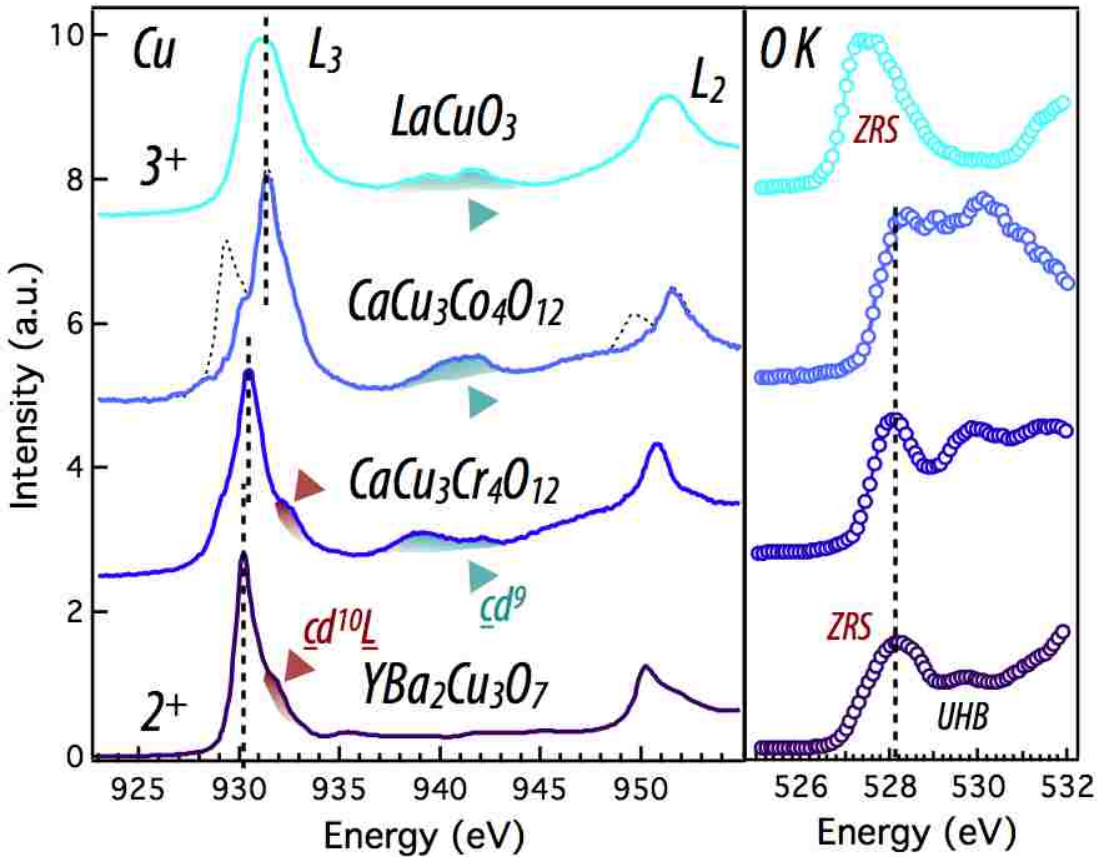

Figure 3.2: Electronic structure measurements of the AOPs and YBCO (d^9; 2+) and LCO (d^8; 3+) reference samples. In the left and right panels the Cu-L edge and the O-K edge are shown respectively. The upper dotted line in the left panel shows the energy position of the Cu $d^9\underline{L}$ (2+) state and the lower dotted line shows the same for the Cu d^9 (2+) state. The higher energy small peaks at $\sim$ show the ionic d^8 (3+) state. The dotted line in the right hand panel shows the energy position of the doped hole on oxygen. Figure originally published in Ref. [10].

in Madelung energies in the materials. Finally, a small high energy peak around 940 eV (highlighted) has been linked previously to the Cu d^8 state[88, 89, 90, 91, 92, 93]. Taken as a whole, this spectrum indicates CCCoO contains a strong majority of Cu 3+ ions, with a small weight of the more typical Cu d^9 state. In contrast, the CCCrO spectrum is very similar to YBCO, with the white lines well-aligned to each other. However, there is still a small peak around 940 eV, again indicating a small Cu d^8 component. Most interestingly, the small high-energy shoulder on the white line present for YBCO, the signature of the Zhang-rice state discussed in section 3.2.2, is also present. Overall, this spectrum suggests a Cu 2+ majority for CCCrO.

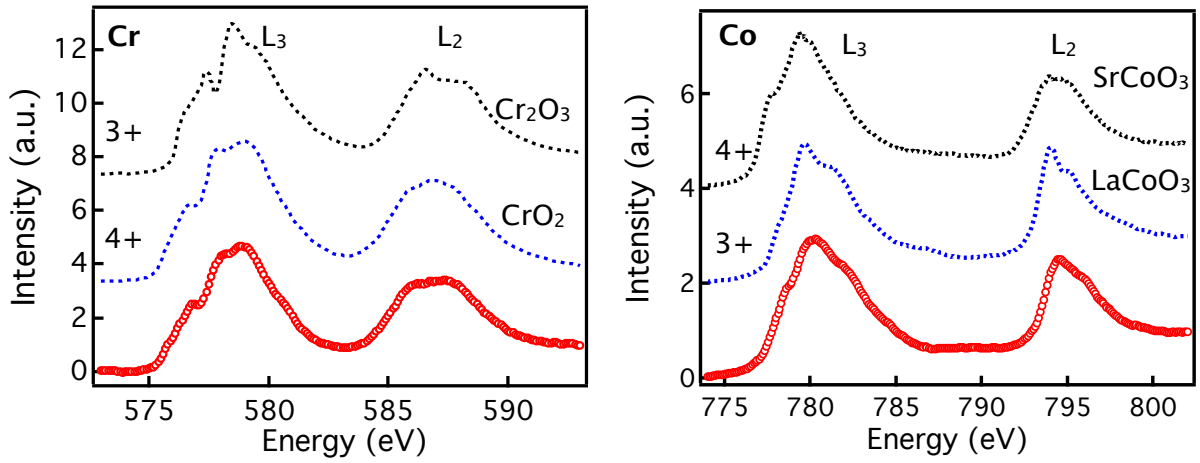

Figure 3.3: Electronic structure measurements of the AOPs at the Cr and Co L-edges. Reference samples are shown for comparison of valence state. Figure originally published in Ref. [10].

The importance of O to the physics of TMOs cannot be understated, and this is particularly true in the CTM of which the cuprates are a prime example[94, 95, 96, 97]. Thus, the O K-edge spectra can reveal important details about the electronic structure. Our results, Fig. 3.2 right panel, are again shown alongside the results for LCO and YBCO. As can be seen, all materials have a significant low energy peak around 528 eV, a peak that has been rigorously studied in the past and linked to a doped hole on the O p-band[98]. This doped hole is very common in CTM and is very important to the underlying physics of cuprates. The main difference between the two AOP materials studied from this perspective are the higher energy peaks around 520 eV, wherein CCCoO there is a significant weight of states mixed into the high energy side, while for CCCrO there is a clear separation of these states and the pre peak. This result shall be further discussed in the theoretical discussion below.

While the Cu and O states are the main focus of this investigation, the valence of the B-site is also important to determine what acts as the "charge reservoir" in these materials, the analog for the Cu-O chains in YBCO. We measured the Cr and Co L-edges of the AOPs and several reference samples to determine the charge configuration, Fig. 3.3. There were no standards for energy alignments, thus the comparison can only be made between the line shapes for the different spectra. As can be seen, for CCCrO (Fig. 3.3 a), the measured spectra is quite similar to the 4+ reference sample, CrO_2. This result gives a total charge

configuration of $Ca_1^{2+}Cu_3^{2+}Cr_4^{4+}O_{12}^{2-}$, assuming the ionic limit with Ca 2+ and O 2-, which conserves charge and further evidences the accuracy of the measurements. In the case of CCCoO, Fig. 3.3 b, the comparison is not as straight-forward. The CCCoO spectrum is similar to the Co 3+ spectrum of $LaCoO_3$, however it also contains some features of the Co 4+ spectra $SrCoO_3$, i. e. the low energy shoulder of the white line. Therefore, in this case we judge the Co valence to be mixed but cannot determine an exact value. However, in combination with the Cu data, which gave a Cu charge of $\sim$ 3+, for charge conservation we require Co to be 3.25+, which is consistent with the Co data. Thus a final configuration is found of $Ca_1^{2+}Cu_3^{3+}Co_4^{3.25+}O_{12}^{2-}$.

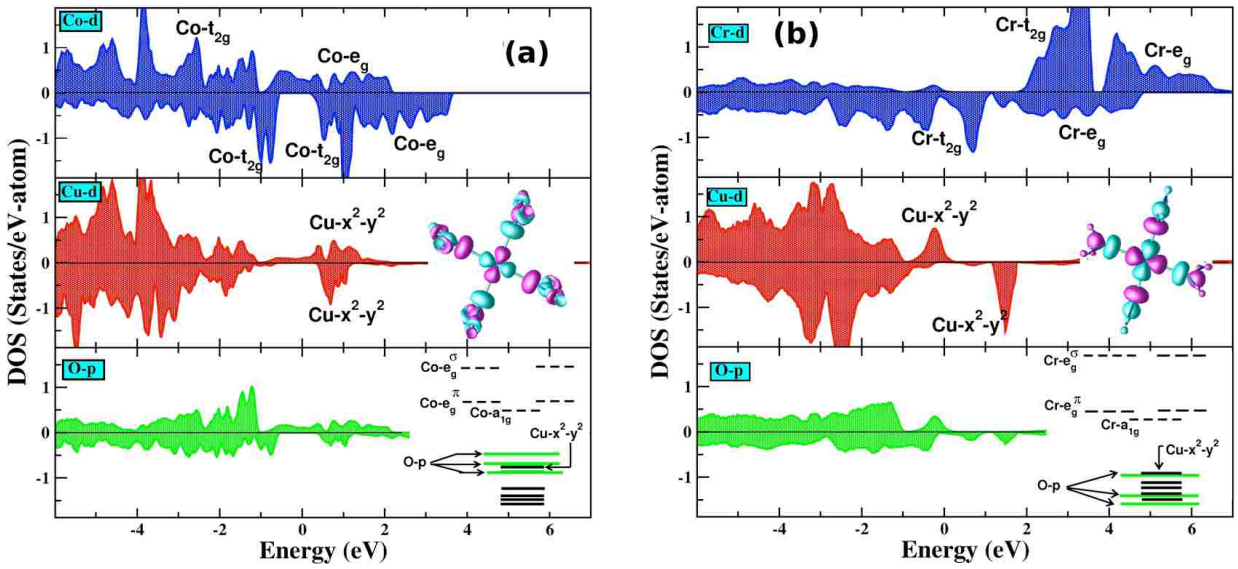

Figure 3.4: Electronic band structure of the AOPs. a) Shows the PDOS for Co, Cu, and O for CCCoO. b) PDOS of Cr, Cu, and O for CCCrO. Also included as insets are the Wannier function shapes and the band diagrams. Positive and negative values represent up and down spins respectively. Figure originally published in Ref. [10].

While these measurements were able to give good approximate valences and reveal some of the characteristics shared with the HTSC, cooperative theoretical calculations are able to reveal more detail and help reveal how the valence state was able to change so drastically on the isostructural lattice. These calculations were carried out using Density Functional Theory (DFT) within the Generalized Gradient Approximation (GGA) with Hubbard U by Tanusri Dasgupta and Swarnakamal Mukherjee at the S. N. Bose National Centre for Basic Sciences. The results of this investigation are shown in Fig. 3.4. As can be seen these materials are characterized by a very large covalence, with Cu, O, and B-site DOS at or near

the Fermi level, showing good agreement with previous experimental observation of metallic behavior in both of these systems[29, 99]. Also, the experimentally observed O-K edge data is well reproduced, with the O-p PDOS on CCCoO being strongly mixed and not displaying any sharp peaks immediately above E_F. Further, the B-site d levels are split into e_g and t_{2g} levels, with the trigonal distortion further splitting the t_{2g} band into e_g^{π} and a_{1g} bands. The Cu site, having square planar symmetry, causes a large increase in the energy of the in-plane $d_{x^2-y^2}$ orbitals, which will be empty for d^8 and be half-occupied for d^9. Looking closer at the Cu band structure, the theoretical results confirm the experimental observations, CCCoO is found to have an almost empty $d_{x^2-y^2}$ band, giving Cu d^8 and CCCrO is found to have a nearly single electron occupation, giving d^9. Further, the Cr (Co) state was found to 4+ (3.25+), confirming the experimental conclusions and lending further credence to the Co valence that the Co L-edge could not exactly pinpoint.

This method, giving spin-polarized DOS, also gave the magnetic moments at each ion. For CCCoO the Cu moment is found to be 0.07 μ_B, which is expected for the exotic d^8 state, and 1.7μ_B for Co which also complies with the finding of a strongly mixed valency. For CCCrO the Cu moment is found to be 0.5 μ_B and the Cr moment is found to be 2.2 μ_B, both also in good agreement with our experimental observations.

Looking further, in Fig. 3.3 insets, the energy level diagrams show the Cu d and O p states are nearly degenerate, as in the HTSC cuprates. This leads to the cuprate-like Cu $d_{x^2-y^2}$ and O p_x, p_y pdσ bonding, with the added entanglement of the B-site d orbital bonding with the same O. In the case of CCCrO, Cu and O levels are very similar to the HTSC, with a small hole doping due to the O p level and Cu $d_{x^2-y^2}$ nearly degenerate at the Fermi level. Finally, the Wannier functions, which were obtained by keeping the Cu $d_{x^2-y^2}$ active and down-folding / integrating out the additional degrees of freedoms, lend further insight on the role of B-site. As can be seen, Fig. 3.3 insets, the B-site has almost no mixing with the Cu - O bond, instead giving an anti-bonding Cu - O wave function further reminiscent of the cuprates. In CCCoO, the situation is very different. The Co d orbitals here does hybridize with the empty Cu $d_{x^2-y^2}$ orbital, further distancing this compound from the case of the cuprates.

Thus, the experimental and theoretical results all point to a large Cu valency change depending on the choice of B-site, with final charge configurations of $Ca_1^{2+}Cu_3^{2+}Cr_4^{4+}O_{12}^{2-}$ and $Ca_1^{2+}Cu_3^{3+}Co_4^{3.25+}O_{12}^{2-}$.

3.2.2 Zhang-rice physics and relation to superconductivity

While the true microscopic origin of HTSC remains a mystery, several "ingredients" have been identified as necessary for it's occurrence, in the case of the cuprates these have been extensively researched. One of the key components identified in this case has been the so-called Zhang-Rice state (ZR), detailed herein[30]. Anderson *et al* showed the cuprate SC could be modeled with a single-band effective Hamiltonian, which was surprising due to the knowledge that a doped hole on O existed in addition to the electron on Cu, thus pointing towards the need for at least a two-band model[100]. F. C. Zhang and T. M. Rice were able to solve the apparent paradox by utilizing a two-band model including the hole on O and the Cu 2+ ion that bind to form a local singlet. This singlet state then travels through the lattice as a psuedo-particle and behaves similar to a hole in a single-band Hamiltonian[30]. The experimental signature of this state can be observed using various spectroscopy techniques, with XAS being a common and excellent technique, Fig. 3.2 and 3.5[88, 89, 90, 91, 92, 93]. These studies have shown that HTSC cuprates show a strong Cu d^9 peak with a small peak (appearing as a high energy shoulder) establishing the $d^9\underline{L}$ state. YBCO seen in Fig. 3.2 above is a prototypical example. Furthermore, the doped hole on oxygen is evidenced by the pre-peak on the O K-edge.

In this case, we investigated the presence of the ZR state using both the Cu L-edge and O K-edge XAS. As discussed above, the CCCoO sample contains Cu in the majority $d^9\underline{L}$ state and d^8 state, with almost no weight in the d^9 state. Thus, this sample does not comply with the requirements for the ZR state, which require a majority Cu 2+ state to bind to the doped hole on O. However, in the case of CCCrO, the similarities with the prototypical cuprate, YBCO, is striking, Fig. 3.2. Fitting Voight functions to the L_3 peaks can give some idea of the degree of hole-doping present, though, due to self-absorption effects in bulk samples, the analysis can only be done in TEY mode, which has the disadvantage of being particularly surface-sensitive. The details of our peak fitting procedures can be found in appendix A. In this case, we found that for YBCO the ratio of the peak area of the d^9 and $d^9\underline{L}$ states is 2.05 $\pm$ 0.25, while for CCCrO it is found to be 9.33 $\pm$ 2.36. The large errors are likely due to the closeness of the peaks, $\sim$ 1.5 eV, and the removal of the edge jump. Either way, the result shows a much larger ratio for CCCrO, implying a much smaller hole doping onto O, though the bulk sample surface will be contaminated with various amounts of CuO_2, which will increase the relative weight of the d^9 peak. However, with the majority 2+

Cu and the hole doping, some ZR singlets likely do form. This would imply the possibility of superconductivity in these compounds, however there is another restraint preventing the realization of HTSC in the CuO_4 planes, namely the alternating orientation of each individual plane. This is in contrast to all known HTSC cuprates, which contain psuedo-infinite 2D CuO_2 layers. Thus, the observed lack of HTSC can be reasonably understood. Interestingly, this is the only compound besides LCO we are aware of that contains ZR singlets and is not a HTSC. Going further, the B-site is contained within BO_6 octahedra, and thus could conceivably carry superconductivity. As mentioned previously, recent years have seen HTSC arise in non-cuprate materials, with speculation that such a state can be obtained in the iridates [101]. This lead to our interest in $CaCu_3Ir_4O_{12}$ (CCIrO) as a possible host of this state.

3.3 Competition between heavy fermion and Kondo physics

3.3.1 Valence state of TMO ions

The following section was published in Ref.[11].

First, we discuss the evolution of the electronic structure of Cu. The Cu L_3 edge XAS are presented in Fig. 3.5(a). In accord with the previously reported results [10], for $CaCu_3Co_4O_{12}$ (CCCoO) the main absorption line at 931.4 eV arises due to absorption from the $d^9\underline{L} \rightarrow \underline{c}d^{10}\underline{L}$ transition, where $\underline{L}$ stands for a ligand hole whereas $\underline{c}$ indicates a hole in the Cu $2p$ core states. The low-energy shoulder around 930 eV arises from the $d^9 \rightarrow \underline{c}d^{10}$ transition; the d^9 transition accounting for 10% of the total peak area, indicating that there is a large Cu - O hybridization present in CCCoO. The line shape of the Cu L_3 absorption edge for $CaCu_3Rh_4O_{12}$ (CCRhO), containing the $4d$ element Rh at the B-site, also contains a lesser and yet still significant $d^9\underline{L}$ contribution, giving a Cu valence of ~ 2.6 +. The transport behavior for this compound is quite similar to CCCO and points to CCRhO also being paramagnetic metallic. On the other hand, for CCIrO, the $d^9\underline{L}$ state is no longer present and the L_3 line shape is almost analogous to that recorded from purely ionic d^9 Cu^{2+} charge state, agreeing with an earlier report utilizing electron energy loss spectroscopy (EELS) [88, 89, 90, 91, 92, 93]. This implies that the hole is no longer interacting with the Cu $\underline{c}d^{10}$ final state, showing a significant reduction of the hole contribution to the hybridized orbital between Cu and O. Furthermore, the small multiplet split peak seen around ~ 940 eV for all Cu L_3-edge spectra is due to a transition from the metastable $3d^8$ (Cu^{3+}) to

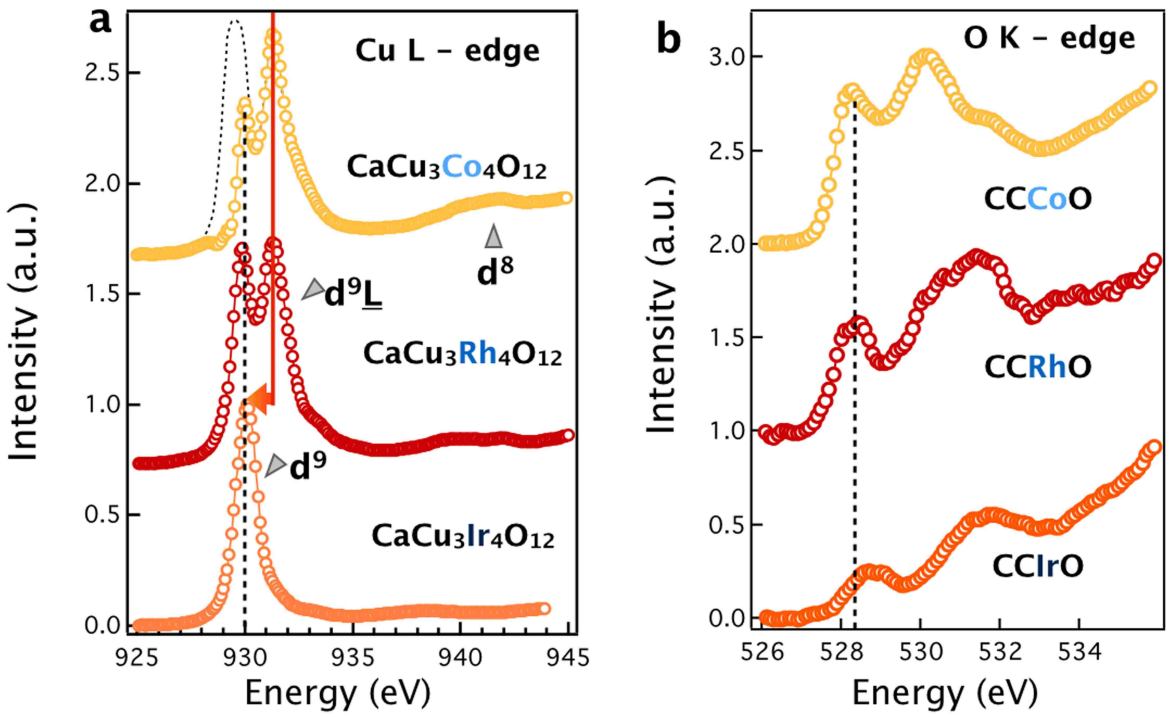

Figure 3.5: a) Soft XAS on the Cu L-edge for all samples showing the changing Cu valence. The dotted line is the spectrum before the subtraction of the impurity peak (Note that CCCoO TFY data and explanation of impurity peak originally given here[10]). The dashed line indicated the energy of the d^9 peak. b) XAS on the O K-edge showing both the reduction of the prepeak on O and the shifting of the O $2p$ - Cu $3d$ and O $2p$ - B-site d hybridized orbitals. The dashed line here indicates the energy of the O prepeak associated with a doped hole. Figure originally published in Ref. [11].

$\underline{c}d^9$ state; the small decrease in this $3d^8$ peak spectral weight in going from Co to Ir also indicates movement towards the ionic $3d^9$ state of Cu [102, 92, 91]. Taken as a whole, the Cu L_3-edge data directly illustrate that in the presence of $4d$ or $5d$ orbitals it is energetically more favorable to transfer the hole on to the B-site instead of stabilizing the Cu^{3+} state, suggesting a strong change in covalency, as tabulated in Table 3.1.

In the past, the electronic structure of Cu has been extensively studied in the context of high T_c superconducting cuprates, where it was also found that the reduction of ligand hole weight on Cu causes a decrease of the pre-peak intensity around 528 eV in the O K-edge XAS spectrum [94, 95, 96, 97]. To track the movement of the hole in the present series of samples, we obtained O K-edge XAS spectra shown in Fig. 3.5(b), with the post-edge normalized to 1 (at 540 eV). As immediately seen, the decrease of the relative intensity of

Table 3.1: Experimental and theoretical values for the valence of Cu and the B-site for each compound

	CCCoO	CCRhO	CCIrO
Cu (experimental)	$(2.90 \pm 0.15)^+$	$(2.63 \pm 0.1)^+$	$(2.03 \pm 0.1)^+$
B-site (experimental)	3.25^+ [10]	$(3.64 \pm 0.1)^+$	4^+
Cu (theory)	3^+	2.5^+	2^+
B-site (theory)	3.25^+	3.6^+	4^+

the pre-peak indeed scales with the reduction of the ligand hole on Cu, implying a marked change in both bandwidth, W, and the charge transfer gap, Δ.

The decrease of the pre-peak intensity can be rationalized in terms of a decreasing availability of empty states as the hole concentration on O decreases in moving from Co to Rh to Ir. While the high energy shoulder on the Cu L_3 peak disappears entirely for CCIrO, the oxygen prepeak does not, which indicates the hybridization between the B-site and O is also significant, as Cu 2+ will not contribute to the prepeak. The results of the O K edge spectroscopy are thus in excellent agreement with the Cu L-edge observations. Another interesting observation is that the energy separation between the pre-peak and the peak around 530 eV increases from Co to Ir. The shift towards higher energy will be discussed in detail in the theory section and is attributed to the gradually increasing separation of the B-site bands (CCCoO) and both the B-site and Cu bands (CCRhO and CCIrO) from the O $2p$ band.

The movement of the hole away from Cu naturally implies a change in valency of the B-site ion. To verify this proposition and to corroborate the previous findings we performed XAS on the L and K edges of Ir and Rh respectively (Co was measured previously and found to be in the $\sim$ 3.25+ state, after subtraction of an impurity peak[10]). Moving to the $4d$ compound, Rh K-edge XAS spectra have been simultaneously collected from the CCRhO sample and a standard $SrRhO_3$ reference sample. Though the line shape from CCRhO shares similarities with $SrRhO_3$ (Rh^{4+}), the difference in energy at 80 % of the normalized absorption was found to be $\sim$ 0.68 eV lower relative to $SrRhO_3$, Fig. 3.6(a)[103]. Unfortunately a cursory analysis was not sufficient to determine the valence, thus, to further investigate the mixed valency of Rh, further analysis was done on the energy shift of the edge jumps. In the case of Rh 3+ (Rh2O3) and 4+ (Sr2RhO4) compounds the edge jump has a

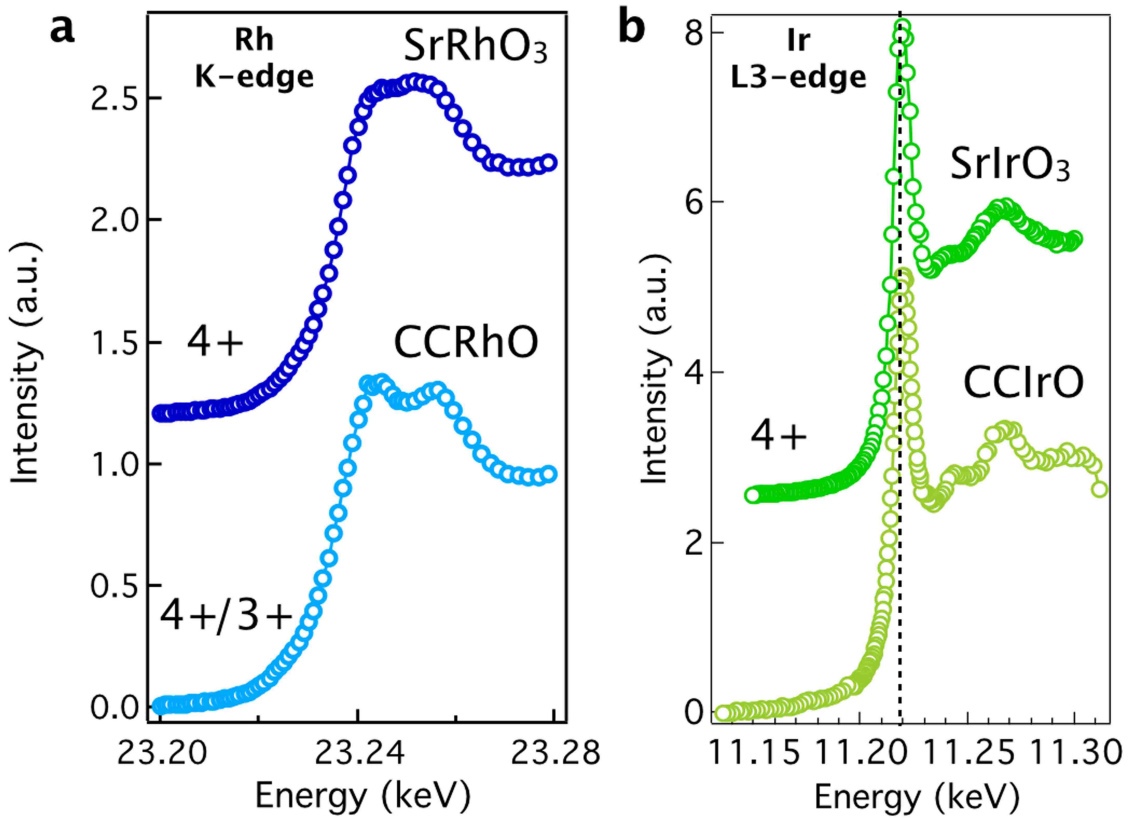

Figure 3.6: a) Hard XAS Rh K-edge measurements on the CCRhO and $SrRhO_3$ (4+) standard. The line is a guide to the eyes. b) XAS on the Ir L_3-edge for both CCIrO and a $SrIrO_3$ standard evidencing the nearly identical line shape and position indicating the 4+ valency. The dashed line shows the excellent agreement of the peak positions. Figure originally published in Ref. [11].

noticeable shift in energy, Fig. 3.7(b). In this case it is found that the shift is approximately 1.9 eV at 0.8 absorption units, as used by Zeng et al3. The shift of 0.68 eV at 0.8 absorption units for CCRhO gives an approximate valence state of 3.64+, Fig. 3.7(a). Also of note is the absorption edge appears to consist of a doublet. A larger low energy peak corresponds to the 3+ state, and vice versa. In the case of CCRhO, the lower energy feature is slightly larger, further evidencing the mixed valency state. We conclude that the Rh valence state is indeed strongly mixed between 3+ and 4+, with a value of 3.64+ ($\pm$ 0.1). In conjunction with the Cu and O soft XAS, the entire Rh data set strongly supports the notion that the hole still largely resides on the O anion, but spreads to the hybridized orbital with Rh from the O - Cu molecular orbital.

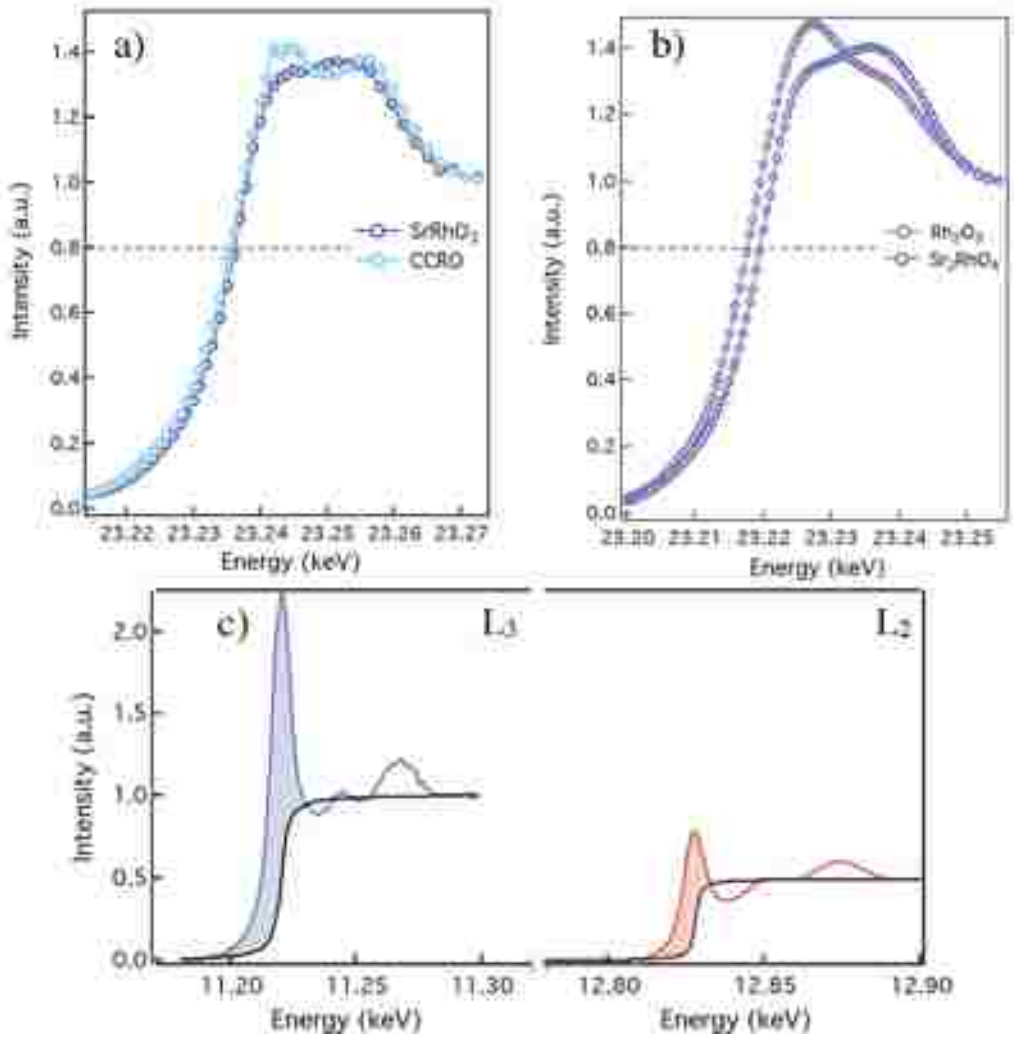

Figure 3.7: X-ray absorption spectra for Ir and Rh edges. (a) Experimental data of Rh edges of CCRhO and $SrRhO_3$. (b) XAS of Rh reference samples Rh2O3 (3+) and Sr2RhO4 (4+). The line at 0.8 is where the energy separation was found. (c) Ir L3 and L2 edges and the fitted edge jumps (black lines) for the branching ratio analysis. Figure originally published in Ref. [11].

Finally, the Ir L_3 edge ($2p_{3/2} \rightarrow 5d$ transition) recorded from CCIrO and SrIr(4+)O_3 is shown in Fig. 3.6(b). As seen, the remarkably similar line shape and the energy peak position both confirm that Ir is in the 4+ state. The L_3 to L_2 branching ratio (BR) was found to be 3.79, Fig. 3.7(c)[104, 105]. This value is similar to that found in several other iridate compounds and signifies a large spin-orbit coupling (SOC) as expected for a 5d compound[104, 105, 106, 107]. Overall, the Ir L edge data is in excellent agreement with the Cu L edge data stating the d^9 Cu^{2+} ground state, with a much smaller d^8 contribution compared to the Rh and Co compounds; thus, in the CCIrO compound the hole is now

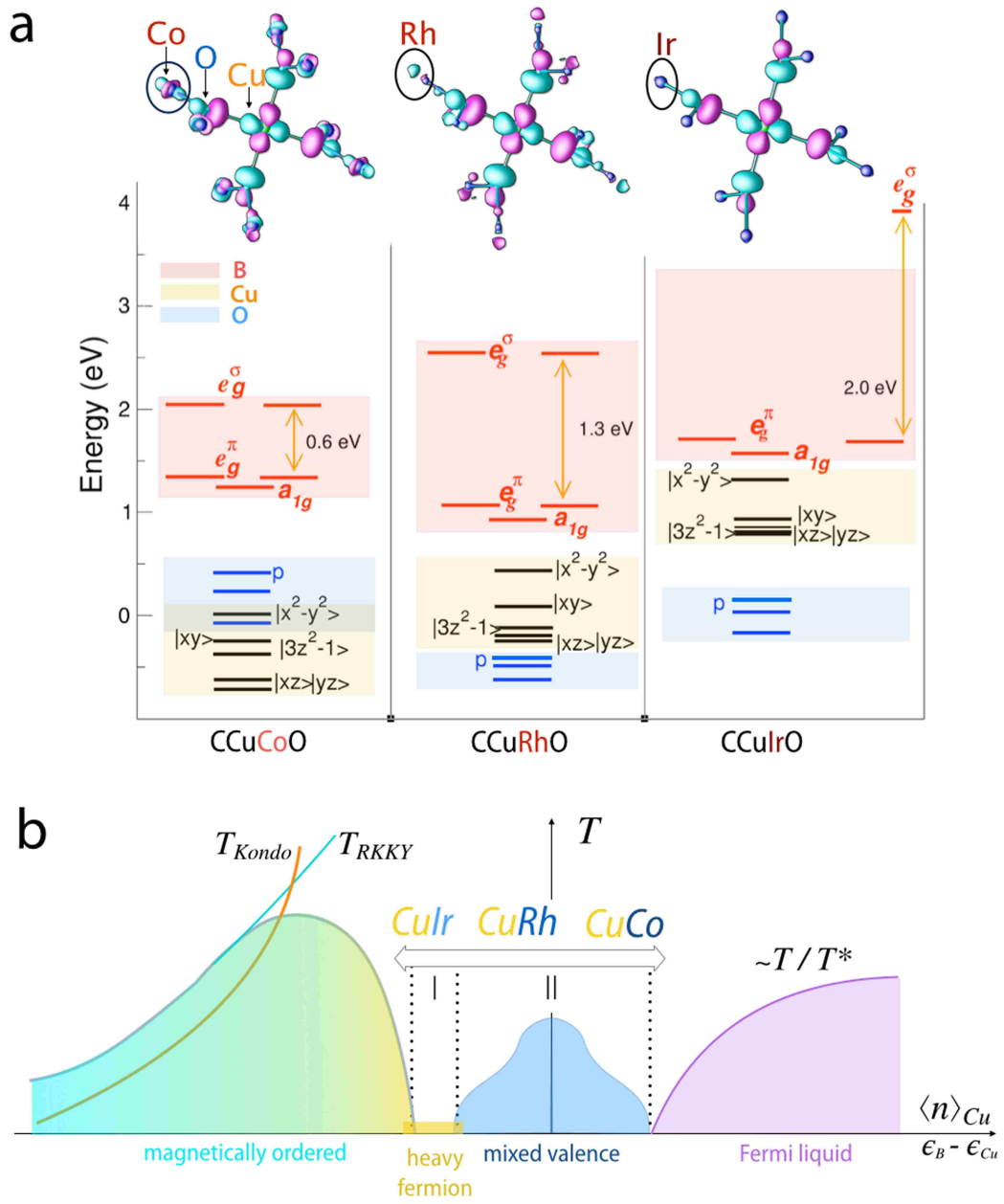

Figure 3.8: a) Top panels: Plots of effective Wannier functions for O p, Cu $d_{x^2-y^2}$ orbitals for CCCoO, CCRhO and CCIrO. Plotted are the constant value surfaces with lobes of different signs colored as cyan and magenta. The Cu, *B*- and O sites are shown as green, red and blue colored balls. Bottom panels: Energy level positions of Cu d, *B* d and O p states for CCCoO, CCRhO and CCIrO. b) Doniach phase diagram showing the dependency on the Cu occupation. Figure originally published in Ref. [11].

almost entirely transferred from the Cu 3*d* - O 2*p* state to the Ir 5*d* - O 2*p* hybridized orbital. The obtained valences for the *B*-sites are also listed in Table 1. F

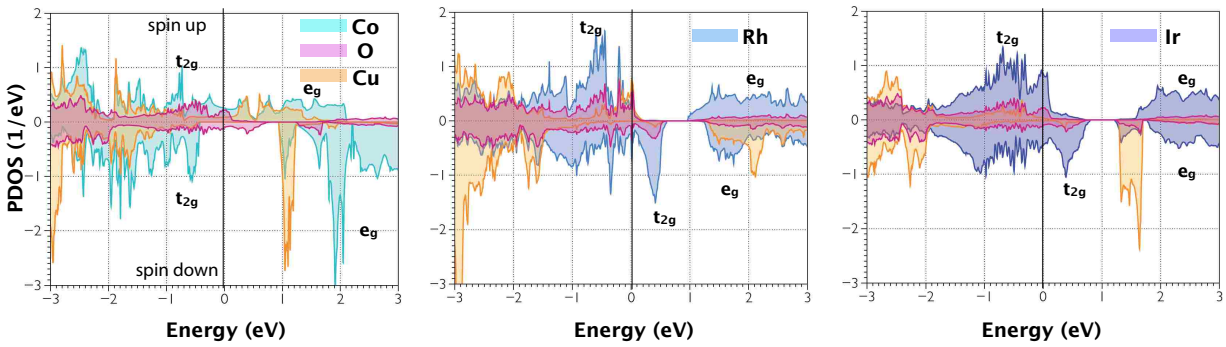

Figure 3.9: Partial density of states (PDOS) of Cu, O, and B-site for each compound. Figure originally published in Ref. [11].

Calculating the spin-polarized electronic structure of the three compounds, as a common feature, we find that the Cu d, B d and O p states are admixed, though the degree of admixture varies between the three compounds. Site projected partial density of states (PDOS) was calculated (not shown)[108]. A direct inspection of the plot for CCCoO reveals that the Cu $d_{x^2-y^2}$ - O (p) states, which are strongly admixed with Co e$_g$ (e$_g^\sigma$) states, are empty in both spin up- and spin down channels, thus lending strong support for the Cu^{3+} ($d^9\underline{L}$) valence in CCCoO. This yields a mixed valence of 3.25+ on Co and the intermediate spin state with a magnetic moment of ~ 1.68 μ_B. Moving towards the CCRhO compound, the admixture between the Cu $d_{x^2-y^2}$ + O state and Rh states becomes markedly reduced compared to that of CCCoO. In this compound, the calculated Cu valence is found to be mixed between 2+ and 3+ ($\sim 2.5+$), with Rh valence close to 3.6+. Unlike Co, magnetically Rh is found to be in the low spin state with a spin moment of 0.21 μ_B and largely quenched orbital moment of 0.05 μ_B.

Finally, we consider the CCIrO. In sharp contrast to both Co and Rh, the mixing of the Cu $d_{x^2-y^2}$ - O p states and the Ir d states is drastically reduced. This results in an almost pure Cu $d_{x^2-y^2}$ - O p state occupied in one spin channel and empty in another, implying a Cu^{2+} valence and nominal Ir^{4+} valence. The spin moments at Ir and Cu sites are found to be 0.45 μ_B and 0.65 μ_B respectively, with a rather large spin moment of 0.12 μ_B on O, arising from strong hybridization with Ir. We note that ionic Ir^{4+} is in the $5d^5$ configuration and has extensively been discussed in view of the interplay of strong SO coupling and correlation physics[104, 105, 109, 110, 111, 112, 21]. The large BR of close to 3.8 signifies the presence of a large spin-orbit coupling at the Ir site, which is found to be common among many of the compounds of Ir 4+ in an octahedral environment, even when the compound is metallic

as in IrO_2[107]. The orbital moment at the Ir site, calculated within the GGA+U+SO, turned out to be 0.12 μ_B, smaller than the spin moment with $m_{orbital}/m_{spin}$ being 0.27. This is curious when compared to the values obtained in cases like $BaIrO_3$[105]. The structure and coupling mechanisms are, however, rather different between compounds like Sr_2IrO_4 or $BaIrO_3$ and the present one. In the former examples, magnetic interactions are one or two-dimensional Ir - Ir, while here they are Cu - Ir with three dimensional connectivity. The dominance of hybridization produces an additional induced spin moment at the Ir site due to the presence of the magnetic ion Cu, a behavior qualitatively similar to the case of La_2CoIrO_6, discussed in recent literature[106]. The presence of a significant SO interaction is found to mix up and down spins and destroys half-metallicity in CCIrO. We note here that inclusion of spin-orbit coupling allows for the non-collinear arrangement of spins. We have therefore carried out spin-polarized calculations assuming collinear as well as non-collinear spin arrangements. The calculated magnetic moments at various atomic sites, obtained in non-collinear calculations, turn out to be very similar to that obtained assuming simple collinear arrangement of spins. The spin magnetic moments are found to be similar to that obtained from collinear calculations within 1-2%, while the orbital magnetic moments are found to differ from that in collinear calculation by a maximum of 0.5%, providing confidence in the general conclusion drawn from the electronic structure calculations on the various valence and spin-states, irrespective of the assumed spin arrangements.

The evolution of the nominal valence of Cu from predominant 3+ ($d^9\underline{L}$) to 2+, as one moves from 3d (Co) to 4d (Rh) to 5d (Ir) elements at the B-site, is controlled by mixing between B-site d states and Cu $d_{x^2-y^2}$ - O p states and can be vividly visualized in the effective Wannier function plots shown in Fig. 3.8(a) (upper panel). As clearly seen, the Wannier functions centered at the Cu site have the orbital character of $d_{x^2-y^2}$ symmetry, and the tail is shaped according to the symmetry of the orbitals mixed with it. Specifically, moving from CCCoO to CCRhO to CCIrO, we find the weight at the tails centered at the B-site (marked by a circle) progressively diminishes.

Microscopically, the nature of this peculiar unmixing / dehybridization effect between Cu-O and B-site in moving from 3d to 4d to 5d element at the B-site can be further elucidated by considering the energy level positions of B d, Cu d, and O p states (see Fig. 3.8(a) (bottom panel)). As mentioned above, the octahedral crystal field coupled with the trigonal distortion separates the B d states into doubly degenerate e_g^σ, e_g^π and singly degenerate a_{1g} ones, while the square planar geometry of the CuO_2 plane breaks the Cu d states into Cu $d_{x^2-y^2}$ and the

rest, with Cu $d_{x^2-y^2}$ being of the highest energy. In progressing from CCCoO to CCRhO to CCIrO, the relative position of Cu $d_{x^2-y^2}$ with respect to O p states increases, driven by the pushing down of O p states due to the increased crystal field splitting (e_g^σ - e_g^π/a_{1g} splitting) at the B-site. This, in turn, makes the hybridization between the Cu sublattice and B sublattice weaker and weaker since those ions communicate via the intervening oxygen. This highlights a key difference between CCIrO and $CaCu_3Ru_4O_{12}$, where for the later it was found that the suspected Kondo-like physics was unlikely due to a strong mixing of Cu with O[113, 114]. Similar to that of high T_c cuprates, for CCCoO the O p states are positioned *above* Cu $d_{x^2-y^2}$, placing Cu in to a *negative charge transfer* regime which promotes a high-T_c cuprate like $d^9\underline{L}$ state akin to the Zhang-Rice singlet state[10, 30, 25, 115]. The progressive weakening of covalency between the B sublattice and Cu-O sublattice as one moves from CCCoO to CCRhO to CCIrO, makes the spread of the effective Cu $d_{x^2-y^2}$ Wannier function (top panel of Figure 3.8(a)) in the case of Ir dramatically reduced compared to either Co or Rh.

3.3.2 Mapping onto the Doniach phase diagram

Finally, the element resolved spectroscopic results combined with the *ab-initio* calculations prompts us to build a unified framework to explain their emergent physical behavior. While an earlier study utilizing EELS found small changes between 3-4-5 d A-site ordered perovskites from different columns[88], our study reveals that upon ascending a column of the periodic table from Ir to Co, the Cu $3d_{x^2-y^2}$ orbital occupation changes from practically ionic $3d^9_{x^2-y^2}$ (S=1/2) for CCIrO to the non-magnetic cuprate Zhang-Rice like state with $3d^9\underline{L}$ ($S = 0$) for CCCoO, as supported by experimentally and theoretically deduced valences listed in Table 1. Along with it, these localized and magnetically active Cu d-states in CCIrO shift towards the Fermi surface demonstrating a rapid change in hybridization compared to both CCRhO and CCCoO. On the opposite end, such a drastic change in the Cu orbital occupation results in the *mixed valence* intermediate spin state of $Co^{3.25+}$, mixed valence Rh $\sim$ 3.7+ but ionic Ir^{4+} ($5d^5$). These findings allow us to place the three compounds under discussion in the context of the Doniach phase diagram depicted in Fig. 3.8(b), where the fundamental control parameter is the average occupation $\langle n \rangle_{\mathrm{Cu}}$ of the $d_{x^2-y^2}$ orbital modulated by the hybridization from the strongly mixed B-site d- and O p-bands[116, 117, 118]. In the modern version of the Doniach phase diagram interesting physics involving heavy fermions

manifests itself as a competition between the Kondo liquid and spin liquid behavior mediated by chemical doping, while very little attention has been given to the mixed valency regime, particularly in *d*-electron systems and in the absence of doping[116, 117, 118, 119, 120, 121]. In this framework the overall ground state is defined by the competition between RKKY type magnetic exchange between magnetic holes on Cu with the Kondo screening by conduction carries from the B-O sublattices. For CCIrO, with a $S = 1/2$ *d*-hole localized on Cu, the large magnetic exchange is comparable in strength with the Kondo screening, resulting in the strongly enhanced effective mass observed with transport and thermal measurements[31]. Thus, Cheng *et al.* firmly placed CCIrO into the heavy fermion regime I in Fig. 3.8(b) with the antiferromagnetic local moment short-range magnetism[31, 88]. In moving from Ir to Rh and Co, the Kondo energy scale begins to gain due to the collective hybridization of Cu d-holes into the ZR singlets. With the strong reduction in the Cu $d_{x^2-y^2}$ orbital occupation both CCRhO and CCCoO enter the regime II of mixed valency (or Kondo liquid phase) in Fig. 3.8(b). Unlike regime I, in the mixed-valence regime quantum fluctuations between different electronic configurations are highly relevant; in this regime, the local electronic and magnetic structure of Kondo centers (Cu) is defined by the redistribution of electrons between Cu d-states and electrons from the strongly hybridized d and p-states of Rh (Co) and O, i.e. $|3d^9,\, S = 1/2\rangle$ vs. $|3d^9\underline{L}, S = 0\rangle$. The conjectured microscopic framework that links the electronic and magnetic ground state of the *A*-site perovskites with macroscopic behavior opens a path in designing emergent ordered phases with heavy fermion behaviour, quantum criticality, and unconventional superconductivity in the magnetic Kondo lattice of cuprate-like moments.

To summarize, we performed XAS measurements and first-principles calculations on a series of *A*-site ordered perovskites, chemical formula $CaCu_3B_4O_{12}$, spanning one period of the periodic table. Surprisingly, we find that the materials fit well within the Doniach phase diagram, being controlled by the hole count on Cu, leading to the conclusion that the competition between RKKY and Kondo effects is responsible for the anomalous behavior observed in the CCIrO compound.

3.4 Conclusion

The results of our investigations on the AOPs provided us with some key insights on both the effects of isostructural doping and the potential of these materials to display

HTSC. Both studies were able to show that changing the *B*-site has tremendous effects on the valence state observed for Cu. This gave the ability to effectively "hole dope" Cu in a controlled matter, similar to numerous previous studies utilizing random doping, but without the added complication of defects and *structural changes*. This doping can be achieved moving both laterally and vertically on the periodic table at the *B*-site. Through this novel microscopic engineering method two distinct relations to HTSC were found. The relation to the cuprates is the most obvious. In the case of CCCrO it was found that the "hole doping" was analogous to the well-known HTSC YBCO. The Cu in this material forms CuO_4 planes that mimc the CuO_2 planes in the cuprates. However, the lack of interconnectivity between these alternating planes seemingly precludes the formation of the HTSC state, despite the explicit presence of the localized ZR state which is a constant feature among the HTSC cuprates. The more contemporary relation is the findings on CCIrO, where Cheng *et al* showed a sharp downturn in resistivity reminiscent of HTSC, which was found to be due to heavy fermion effects[31]. This led to speculation about the possibility of the heavy fermion superconducting state. Our investigation of this compound, in conjunction with CCCoO and CCRhO, revealed the evolution of the electronic structure leading to the heavy fermion state. Starting in CCCoO with a hole localized at Cu, this hole gets gradually redstributed towards the *B*-site, until in CCIrO the hole is nearly entirely distributed to Ir, with a small amount of hole doping still present on O. The Kondo effect, with the Cu 2+ ions creating a Kondo lattice of localized S = 1/2 magnetic moments, then leads to the observed heavy fermion behavior. These electronic structure insights help to shed light on the mechanisms behind HTSC in both cuprates and possibly in future heavy fermion HTSC.

4 Strain modulated Mott transition: Lattice mismatch engineering

In this chapter, we explore the consequences of epitaxial strain on rare-earth nickelates. Due to the low thermodynamic stability of the nickelates[17], stabilization of high quality ultra thin films requires the interface to the substrate to act as a source of extra Gibb's free energy to facilitate the growth of the perovskite structure, as oppose to the impurity NiO and RE_2O_3 phases. As a consequence of this, true bulk-like nickelate single crystals are not realistic, as there is always some effect due to the interface between the two materials. Most significantly, the compression or stretching of the film lattice to match the substrate has a profound effect on the physics, as well as symmetry and octahedral rotation changes. Thus, before any possible device applications or superlattice growth can be considered, the role of epitaxial strain must be further scrutinized. We utilize transport, x-ray diffraction, and synchrotron based x-ray absorption spectroscopy and scattering to explore the effects of epitaxial strain on both $EuNiO_3$ and $NdNiO_3$ in regards to the metal-insulator transition and the related magnetic and charge ordering.

4.1 Introduction

As discussed in section 1.2.2, an emerging method that is being heavily utilized in recent years for exploring the phase space of TMOs is the application of epitaxial strain in thin films. This heterostructuring has lead to many anomalous ground states which were not observed in the corresponding bulk materials, showing great promise for use in technological applications. This method is a natural consequence of the stabilization of ultra thin films, which are not thick enough to relax to their bulk-like structure. By utilizing the entire catalog of available substrates very thorough investigation of the available phase space is possible. Such reports have become readily available for many materials, with the nickelates in particular being thoroughly explored[4, 46, 45, 47, 48, 49]. In particular, for $NdNiO_3$ an in-depth work by Jian Liu *et al* showed that not only did the strain control the phase, but it showed similarities with the bulk phase diagram that was obtained by varying the rare earth ion (RE) in $RENiO_3$, while it also contains important new phases that must be considered[12]. In this phase diagram, Fig. 4.1, several ground states not observed in the bulk phase diagram were kinetically stabilized.

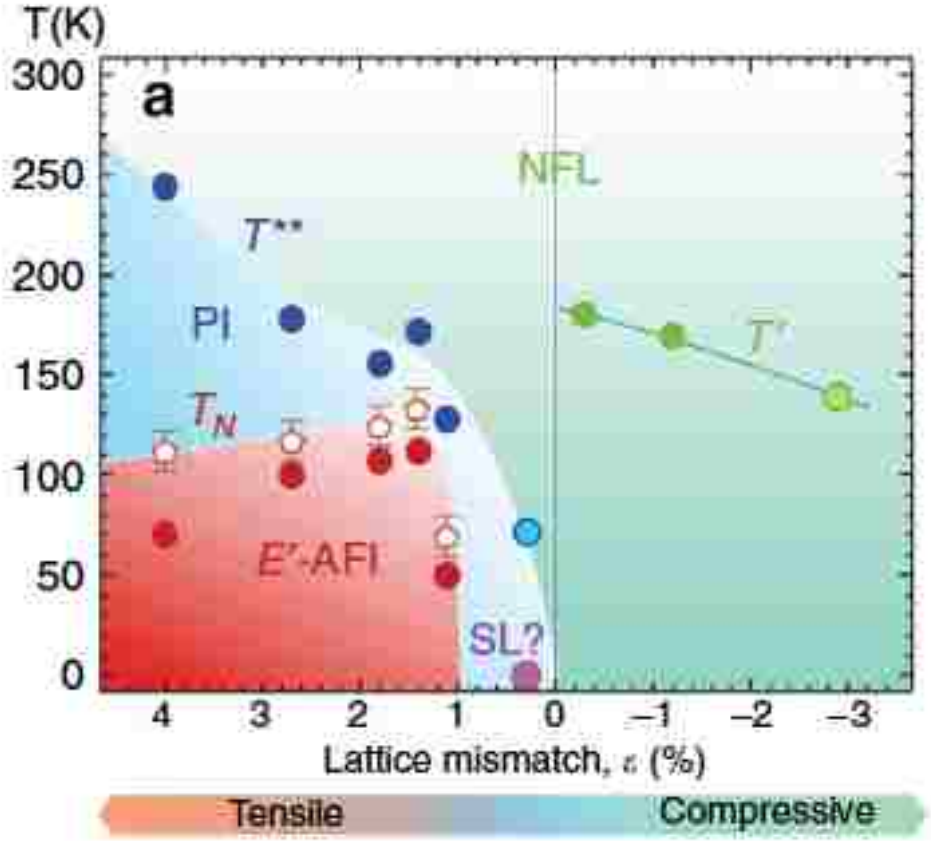

Figure 4.1: Strained NNO films on various substrates showing remarkable variation in physical properties. Blue circles represent MIT, red circles denote the hysteric inflection point, green circles represent the transition to non-Fermi liquid behavior, and open pentagons denote the AFM transition. Phase diagram originally published in Ref. [12].

Specifically, under compressive strain ($\epsilon < 0$) non-Fermi-liquid behavior was observed, with several distinct coefficients for the resistivity's T dependence (4/3 and 5/3) at low temperature due to either 2 or 3D quantum critical behavior, with typical bad metal behavior (T^1 above). With large tensile strain ($\epsilon > 0$) giving $T_{MIT} > T_{Neel}$ while at lower strain values a possible quantum critical point is approached, entirely suppressing the anti-ferromagnetic transition and possibly giving rise to a quantum spin liquid state around $\epsilon = 0$. This behavior is rationalized by realizing that beyond simply stretching or compressing the lattice, the heterostructure will also cause mismatches in octahedral rotation, distortions, and symmetry. This work was a rather exhaustive report and investigated nearly the entirety of the $NdNiO_3$ phase space, with the one exception being the observation of charge order (CO). CO was

observed for all the bulk nickelates (undergoing a MIT) and in thick films but has never been measured for ultra thin geometry. The preceding work showed the other bulk-like phases can be suppressed or preserved, so it is likely charge order can likewise be manipulated. This will be explored, along with the observation of charge order in $EuNiO_3$, in section 4.3.

Beyond $NdNiO_3$, epitaxially strained $EuNiO_3$ provides a unique opportunity to investigate a much more distorted nickelate. With the separation of T_{MIT} and T_{Neel} for bulk ENO in contrast to NNO, the separate progenitors of each can possibly be independently probed. Before such in-depth studies can be performed, however, the effect of the compulsory strain must be investigated, as was done for NNO.

4.2 Epitaxial transport modulation on $EuNiO_3$

The following section can be found in our publication[4], with minor editting done here.

The most distorted members with R= Lu, Y, Eu and Sm, *etc.* first exhibit a second order MIT at higher temperature accompanied by the development of a possible charge ordered state[122, 123, 124, 125, 126] while the magnetic moments remain disordered across the transition. Upon further cooling, these compounds undergo another second order transition characterized by a E′ - type antiferromagnetism[17, 38]. In sharp contrast, the members with a smaller degree of structural distortion (*e.g.* R= Nd and Pr) exhibit a first order phase transition emerging directly from the paramagnetic metallic state into the E′ - type antiferromagnetic insulating ground state, thus bypassing entirely the large paramagnetic insulating region[5, 127, 128]. Based on such a diverse behavior controlled by the A-site ion, several interesting theory proposals and experimental results have been put forward to control the MIT for potential applications[129, 130, 131]; however, using different RE ions depending on application seems impractical, as synthesis conditions and thermal stability vary wildly and rarely yield macroscopic size crystals of nickelates[33, 132, 45, 74]. Alternatively, one can explore the obligatory strain in ultra-thin films as a tool to engineer the physical properties based on a careful choice of a *single* member of the family to attempt to modulate the MIT and AFM transitions[45, 46, 47]. En route to this goal, one of the key questions is what effect will strain (tensile and compressive) have upon the phase diagram for the distorted members exhibiting the second order transitions? For example, it has been already shown in the bulk that while isotropic external pressure suppresses the MIT, it also

tends to raise the temperature for AFM transition and eventually leads to a surprising AFM in the metallic ground state[44, 43, 133]; based on this observation, one can expect highly non-trivial electronic and structural response after application of bi-axial strain [52, 90].

ENO films were grown on a variety of substrates incorporating lattice mismatch ranging from +2.5% to -2.4%, the details of which are reported elsewhere[74]. The substrates used for growth are as follows: $YAlO_3$ (YAO; -2.4% lattice mismatch), $SrLaAlO_4$ (SLAO; -1.3%), $LaAlO_3$ (LAO; -0.3%), $NdGaO_3$ (NGO; +1.5%), and $LaGaO_3$ (LGO; +2.5%). XRD measurements were taken around the (002) (psuedocubic notation) truncation rod of the substrate with a Panalytical X'Pert Pro MRD (Panalytical, Almelo), equipped with a parabolic mirror and triple bounce Ψ axis monochromator on the incident and diffracted beams. The same instrument was used to measure a RSM around the (-103) truncation rod. Transport properties were measured with a Quantum Design Physical Property Measurement System (PPMS) using a four point probe in the *Van Der Pauw* geometry. XAS measurements were taken at the 4-ID-C beam line of the Advanced Photon source at Argonne National Laboratory in total electron yield (TEY) mode at the Ni $L_{2,3}$-edges at 250 K.

Theoretical calculations were performed for a NiO_6 cluster with octahedral coordination using the methods described elsewhere[134, 135]. The Hamiltonian includes the on-site Coulomb interaction between the 3d electrons and between the 3d electrons and the 2p core hole. The model parameters are obtained within the Hartree-Fock limit and scaled down to 80% to account for intra-atomic screening effects. The monopole parts were $F^0_{dd} = 6$ eV and $F^0_{pd} = 7$ eV. The spin-orbit coupling was included for the 3d and 2p electrons. The hybridization with the ligands was taken into account by including configurations up to a double ligand hole. The hybridization parameters used were V = 2.25; -1.03 eV for the e_g and t_{2g} orbitals, respectively. The cubic crystal field of 10 Dq was set at 1.5 eV.

Results: Fig. 4.2(a) shows 2θ - ω scans around the (002) truncation rod for the 15 unit cell (uc) ENO films grown on different substrates. All samples show a broadened film peak (indicated by arrows), due to the reduced thickness of the films, and a sharp substrate peak which was used to align each data set. The film peaks for the highly compressive films (YAO and SLAO) show a noticeable shift from the bulk ENO lattice constant (represented by a dashed line) towards smaller 2θ, while for LAO no such shift is observed. On the other hand, films grown under tensile strain (NGO and LGO) exhibit a well resolved film peak with no measurable shift away from the bulk value. Fig. 4.2(b) shows a reciprocal scan map (RSM) around the (-103) Bragg peak for a 35 uc ENO on NGO film (thicker films were

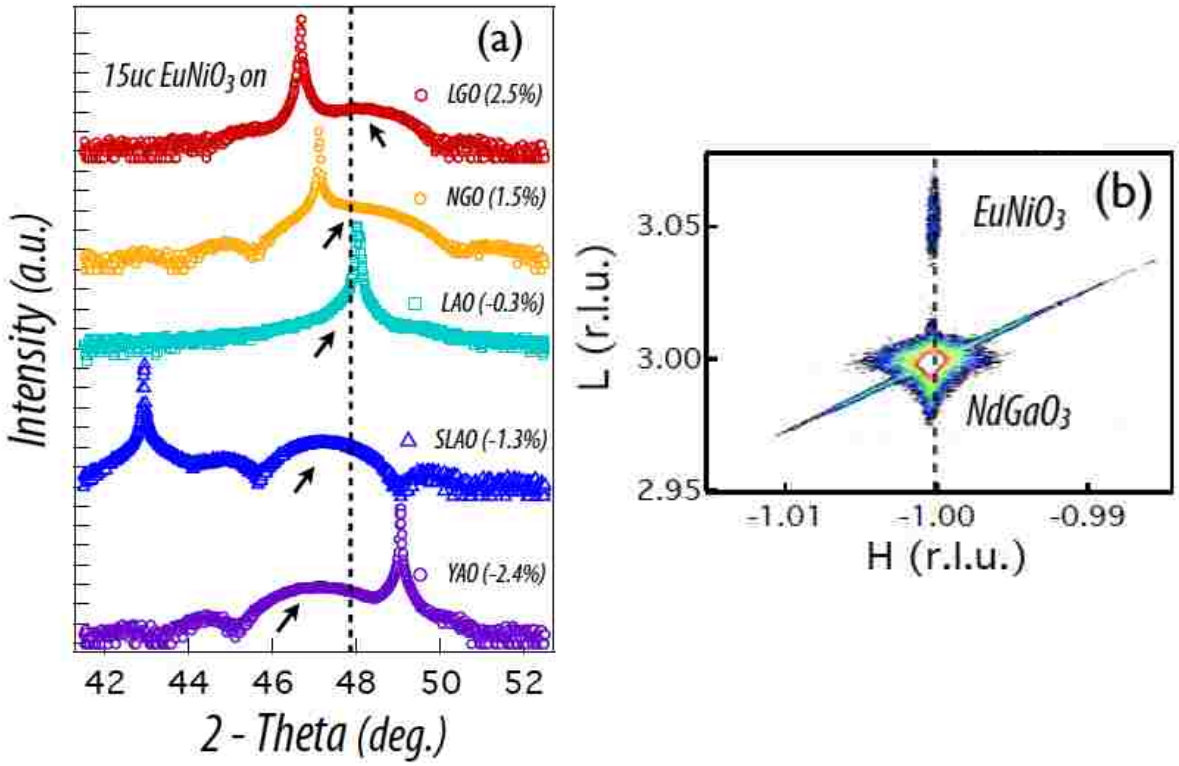

Figure 4.2: (a) XRD data for 15uc ENO samples on various substrates. The shifting from the bulk lattice value (indicated by the dashed line) is apparent for the compressively strained samples. The arrows indicate the film peaks. Note, for SLAO the (006) rod is scanned due to the tetragonal structure. The data have been artificially shifted vertically to ease inspection. (b) RSM for a 35uc ENO film grown on NGO showing the film is coherently strained. Originally published in Ref.[4]

necessary to resolve the peak using this conventional XRD). The weak film peak shares the same value for H (reciprocal lattice units) and a larger value for L, showing the film shares the in-plane lattice constant of the substrate.

After the high structural quality was established we turned our attention to their transport properties shown in Fig 4.3(a). The data were recorded during both cooling and heating cycles from 380 K to 2 K; since no measurable hysteresis was found only the curves measured on warming are shown. As seen, for the tensile strain the resistivity follows the expected bulk-like insulating behavior below 380 K. This behavior, however, markedly changes after reversing the sign of strain. For the small compressive strain on LAO, the resistivity at lower temperatures separates from bulk behavior at $\sim$ 250 K and begins increasing at a lesser rate. For the compressively strained film on SLAO, the sample shows unexpected

metallic behavior at high temperatures with a MIT occurring at 335 K. And finally, for the largest value of strain of -2.5 %, the film on YAO turns metallic in the entire temperature range down to 2 K. To investigate the magnetic transition via the electrical transport, $\frac{dln\rho}{d(1/T)}$ vs T is shown for all films besides ENO on YAO using a custom built liquid nitrogen cryostat to reduce measurement noise which is usually amplified by the derivative analysis, in order to mimick the analysis used by Zhou *et al*[127]. Each film showed a characteristic kink indicative of an AFM transition around 200K. Fig. 4.3(c) shows the extracted T values for the kinks, denoted T*.

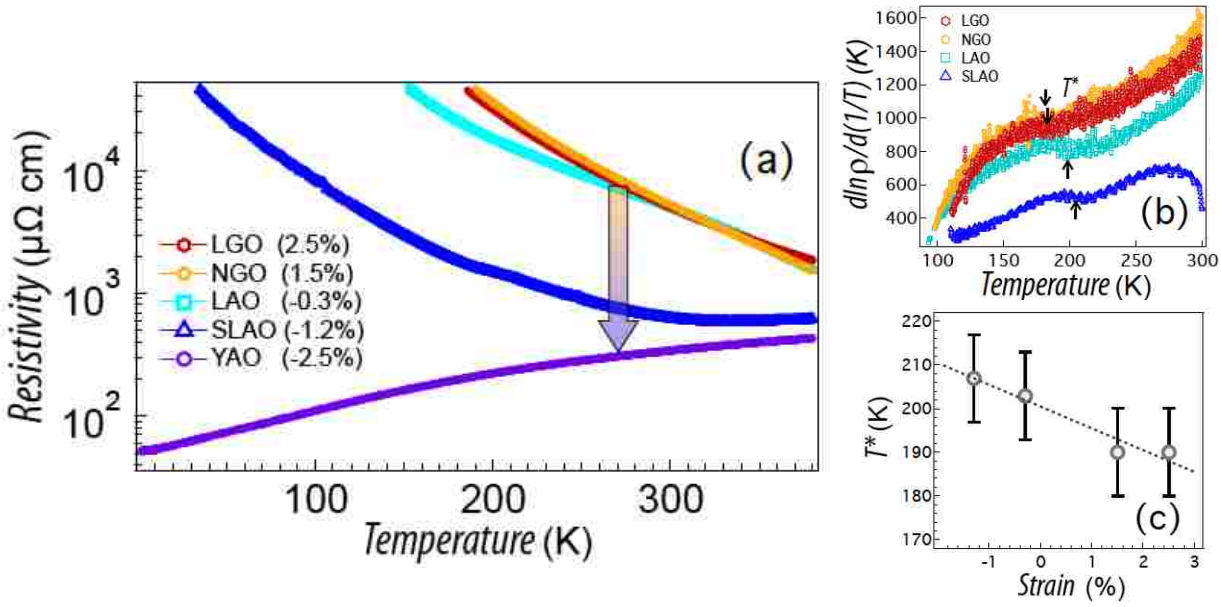

Figure 4.3: (a) Transport data for 15uc ENO samples on various substrates. The arrow indicates the direction of increasing compressive strain. (b) dln(ρ)/d(1/T) data for the films. Arrows indicate the location of T*. (c) T* for various strains. Originally published in Ref.[4]

We performed measurements at the Ni $L_{3,2}$ - edges using XAS to investigate the electronic structure of our films. As seen in Fig. 4.4a, all films show a strong white line at $\sim$ 855 eV and $\sim$ 872 eV. Additionally, a shoulder around 853 eV and 871 eV is apparent for all films, being much larger for the tensile case; this feature gradually decreases with increasing compressive strain. The size of the energy separation between the L_3 multiplet peak for each value of strain is plotted in Fig. 4.4(b) in the left axis. The splitting decreases from the tensile strained films, $\sim$ 1.8 eV, with increasing compressive strain to $\sim$ 1.2 eV for YAO. Fig. 4.4(b) also shows the calculated CT energy (right axis) which follows a very similar trend.

Discussion: The large amount of epitaxial strain built into these materials is due to the extraordinary ability of the perovskite structural units to accommodate the strain through tilts/rotations and changes in lattice symmetry[52]; it is these effects that ultimately lead to the observed modulation of the physical properties. Based on this, 2θ values, corresponding to the film peaks in Fig. 4.2(a), were used to calculate the out-of-plane lattice constants yielding the following c-axis lattice constants: 3.86 Å (YAO), 3.84 Å (SLAO), 3.80 Å (NGO), and 3.81 Å (LGO), while for LAO strong overlap between the substrate peak and film peak due to the small strain value of -0.5%, prevent a reliable c-axis lattice constant from being extracted. While for the samples with in-plane compressive strain the shift of the out-of-plane lattice constants from the bulk value of 3.80 Å is expected and consistent with tetragonal distortion of the unit cell, the samples under tensile strain show no significant shift (e.g. 0.26% for ENO on LGO, much lower then the +2.5% biaxial in-plane strain).

To ascertain whether or not this lack of c-axis lattice modulation was due to strain relaxation, unlikely in ultra-thin films, a RSM was taken to detect any deviation from epitaxial growth. The thicker sample (35 uc) was required in order to obtain a strong enough (-103) film peak with the conventional source XRD. The H value of this film peak matches well with that of the substrate (demonstrated by the dotted line) confirming the film is fully coherent to the substrate (as was found for ENO on YAO[74]), while the center L value of ~ 3.053 r.l.u. gives an out-of-plane lattice constant of 3.793 Å, in excellent agreement with the rocking curve measurement (within 0.2 %). This, along with the bulk-like c-axis lattice constant, implies the strain is compensated for by octahedral tilts and rotations, similar to that found for $LaNiO_3$ films under tensile strain[52, 136]. Further work including X-ray linear dichroism (XLD) measurements and density functional theory calculations need to be performed in order to confirm this.

Tracking the evolution of the MIT with lattice modulation revealed a very significant effect. As compressive strain is increased T_{MIT} is gradually suppressed until entirely disappearing for the case of ENO on YAO. In the case of intermediate compressive strain on SLAO, the linear T-dependent metallic behavior is followed by a MIT shifted to 335 K, putting it very close to room temperature. Unfortunately, the high temperature of the bulk MIT (480 K) prevents us from investigating the change in the T_{MIT} for LAO, NGO, and LGO films. With the lack of hysteresis, characteristic of first order phase transitions, our results strongly imply that epitaxial strain does not induce a first order transition in this material, as was seen in the bulk by application of 'chemical' pressure[128]. Instead the re-

sults show that compressive strain acts to lower the transition temperatures akin to isotropic external pressure[43, 127, 133]. The resistivity results are also strongly reminiscent of behavior of ultra thin films of $NdNiO_3$, where it was proposed that a closing of the correlated gap is responsible for the quenching of the MIT by compressive strain[45].

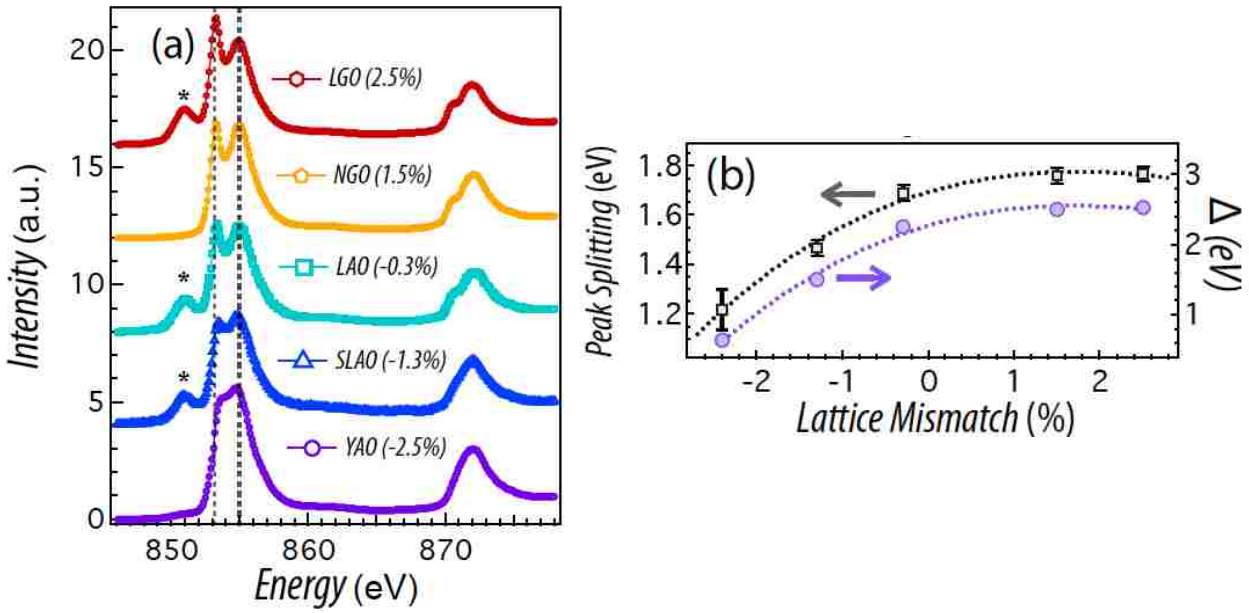

Figure 4.4: (a) XAS data for 15uc ENO samples on various substrates showing the change in the multiplet peak with strain. The data have been artificially shifted vertically to ease inspection. (b) The experimentally obtained peak splitting along with the theoretically obtained corresponding CT energy. Note, a small peak, indicated by the asterisks, around $\sim$ 851 eV corresponding to the La M_4 edge appears for the substrates containing La. Originally published in Ref.[4]

The ultra-thin nature of the samples precludes direct investigation of the sample by way of conventional magnetometry. In an attempt to locate the AFM transition temperature, $\frac{dln\rho}{d(1T)}$ was extracted for all insulating samples; this analysis allowed Zhou *et al* to reveal a characteristic spin ordering temperature in the bulk nickelates where spin ordering appears as a kink in the T dependence[127]. As seen in Fig. 4.3(c), all the films exhibit a broadened kink around T^*. The error bars are meant to represent the approximate width of the kink, which is similar for all samples. The magnitude of T^* is approximately 12K lower for the tensile strained samples and is similar to the change reported for external pressure[127].

For LAO, with very small compressive strain, the value is shifted upward to 203 K. For SLAO the value of T^* is further shifted to 207 K, indicating that the Neel temperature

for these films is shifted higher with higher value strain, analogous to the effect of external pressure reported by Zhou *et al*[127]. Resonant x-ray scattering measurements are needed in order to further confirm these changes in T_N and investigate any possible changes in magnetic structure, which cannot be deduced via transport.

Resonant soft X-ray absorption has been extensively utilized in the study of $RENiO_3$ perovskites[113, 45, 137]. The small thickness ($\sim$ 6 nm) of these films compares well with the probing depth ($\sim$ 12 nm) of TEY mode and allows us to explore the electronic structure of the entire sample. In all of the rare-earth nickelates, $RNiO_3$, Ni is maintained in the metastable Ni^{3+} state, with a strong tendency to phase decompose by the following: $RNiO_3 \leftrightarrow 2NiO + R_2O_3 + \frac{1}{2}O_2$, especially in the case of high strain or low tolerance factor (large distortion from the ideal cubic structure). Fig. 4.4(a) shows the measured absorption for the whole range of strain values. As seen, the strong white line at 855 eV and 872 eV corresponds to the L_3 (L_2) edge transition from the d^7: $t_{2g}^6 e_g^1$ ground state to the $\underline{c}t_{2g}^6 e_g^2$ ($\underline{c}$ denotes a core hole) excited state. Another lower energy peak, $\sim$ 853 eV, which corresponds to the same electronic transition when strong electron localization is present, becoming prominent for the highly tensile strained samples. This systematic change in the multiplet / L_3 relative position and intensity holds valuable information about the hybridization of the d^7 and $d^8\underline{L}$ states. The quantitative value of the observed splitting, which is simulated by tuning the charge transfer energy (Δ) is plotted in Fig. 4.4(b)[135]. In order to obtain the peak splitting the data was fitted with two Voight functions. A direct inspection of the plot clearly shows that this splitting begins decreasing as the films are compressed in the a-b plane, suggesting that a change in the degree of covalency between Ni and O is likely a cause of the observed transport properties. To confirm this, ab-initio cluster calculations were carried out using the charge transfer energy Δ as a a control parameter (see Fig. 4.4(b) (right side)). The results of the calculation directly suggest that changing Δ reproduces the observed splitting well, with a value as large as $\sim$ 2.5 eV for the tensile strained samples and being reduced down to the very small value of $\sim$ 0.65 eV in the case of the all metallic film on YAO corresponding to an enhanced degree of covalency by almost four times (spectra can be seen in Ref. 52[135]).

The large reduction in Δ (approximately 1/4th of the saturated value for ENO on YAO) strongly implies that hybridization is strongly increased between Ni-d and O-p orbitals. In addition, the value of $\frac{dln\rho}{d(1/T)}$ (Fig. 4.3(b)) at room temperature is approximately equal to the activation gap, showing the activation energy is steadily increased as compressive strain is reduced and nearly quenched for the tensile strained samples.

The reduction of Δ and the activation gap under compressive strain can be rationalized in terms of changes in the Ni-O-Ni bond; as the lattice is compressed in plane an increase in the overlap of the O: $p_{x,y}$ and Ni: $d_{x^2-y^2}$ orbitals occurs. Furthermore, the increasing covalence is strongly resemblant of the effect of A-site cation exchange[17]. On the other hand, for the tensile strained samples, the bond overlap would decrease, leading to a reduction in Ni-O hybridization, except for the fact that the splitting and transport appear to remain *unchanged* with increasing tensile strain. This observation indicates that as the strain is changed from compressive to tensile the major $d^8\underline{L}$ contribution to the ground state becomes effectively decoupled from the ionic d^7 state. It is interesting to note that these results are also compatible with the recent Density Functional Theory + Dynamical Mean Field Theory (DFT + DMFT) nickelate calculations, based on a site-selective Mott state, where the insulating gap is determined by the singlet formation energy between an O-p hole and Ni-d electron[126]; the theory also suggests the decoupling of the d^7 and the $d^8\underline{L}$ states leading to an insulating ground state. Further corroborating our results, Wang *et al* recently suggested that the insulating regime is largely controlled by the d-band occupancy, and not by the intra-electronic repulsion, which is strongly dependent on the charge transfer from oxygen ions[138].

To summarize, epitaxial ultra-thin films of ENO grown on a variety of substrates spanning both compressive and tensile strain were investigated with XRD, electric d.c. transport, resonant XAS, and first principle cluster calculations. The sample's electronic properties were found to be highly tunable by strain, shifting the Mott transition tantalizingly close to room temperature and only affecting magnetic ordering transition T_N to a small extent. The absence of hysteresis indicates that the transitions remains second-order, showing a key difference between epitaxial strain and A-site doping implying that compressive strain effectively mimics external isotropic pressure. A combination of XAS and ab-initio cluster calculations has determined that compressive strain enhances the covalence of the Ni-d and O-p orbitals, eventually leading to an entirely metallic ground state not accessible in the bulk. These results showcase ENO's tunability, as the MIT can be tuned from the impractically high bulk value of 480 K to near room temperature or to being entirely quenched without the complication of chemical doping.

4.3 Charge and magnetic ordering in ultra thin films

Having established the effects of the ultra thin geometry and lattice mismatch on the MIT in both NNO and ENO, we then subjected these systems to soft and hard x-ray resonant scattering to investigate the charge and magnetic ordering patterns. While both the bulk materials show E′-type AFM and a rock-salt charge order pattern, the manipulation of the MIT led us to hypothesize there could be some further discrepancies with the bulk-like behavior.

4.3.1 Symmetry locking in epitaxial $NdNiO_3$

The combination of multiple transitions at the same temperature for RE = Nd has fueled a debate on the definitive origin of the MIT. Among these, the Ni $2d^7 \rightarrow d^{7-\delta} + d^{7+\delta}$ charge ordered ground state has been fastidiously scrutinized with various techniques, including resonant x-ray scattering (RXS), and been shown to invariably accompany the MIT both in the bulk and in thick films[139, 123, 124, 140]. Previous RXS measurements focused on the (0 1 5) and (1 0 5) orthorhombic peaks, which have no Ni contribution in the metallic state (*Pbnm* symmetry), but become allowed with the advent of charge disproportionation ($P2_1/n$ symmetry). Additionally, it was found that within DFT theory the CO alone can drive the MIT, making it a likely culprit for the MIT[133]. On the other hand, recent infrared spectroscopy measurements demonstrated the importance of Mott physics for the MIT in $NdNiO_3$ film[141]. In a pure Mott picture, however, T_{MIT} would be expected to be well above T_{Neel}, as observed in only the more distorted nickelates, and no bond disproportionation would have occurred. However, bond disproportionation has been observed in the nickelates, thus the Mott picture cannot fully explain the results as well[123, 124, 139, 140]. Finally, RXS on the (1/2 0 1/2) orthorhombic peak has revealed that the AFM is also unwaveringly commensurate with the MIT in NNO, raising the question of what role, if any, it may play[13, 14, 142]. The case of an anti-ferromagnetically driven MIT, known as a Slater transition, has only recently been experimentally realized suggesting the role of the AFM transition in the nickelates deserves further scrutiny[143, 144]. In this direction, Lee *et al* recently showed the Landau theory indeed predicts an AFM driven MIT in the nickelates[39] . Likewise, Yamamoto *et al* utilized *ab initio* density functional theory (DFT) calculations using the local spin density approximation (LSDA) to show magnetism alone can open the insulating gap. Interestingly, Hepting *et al* recently showed the AFM can

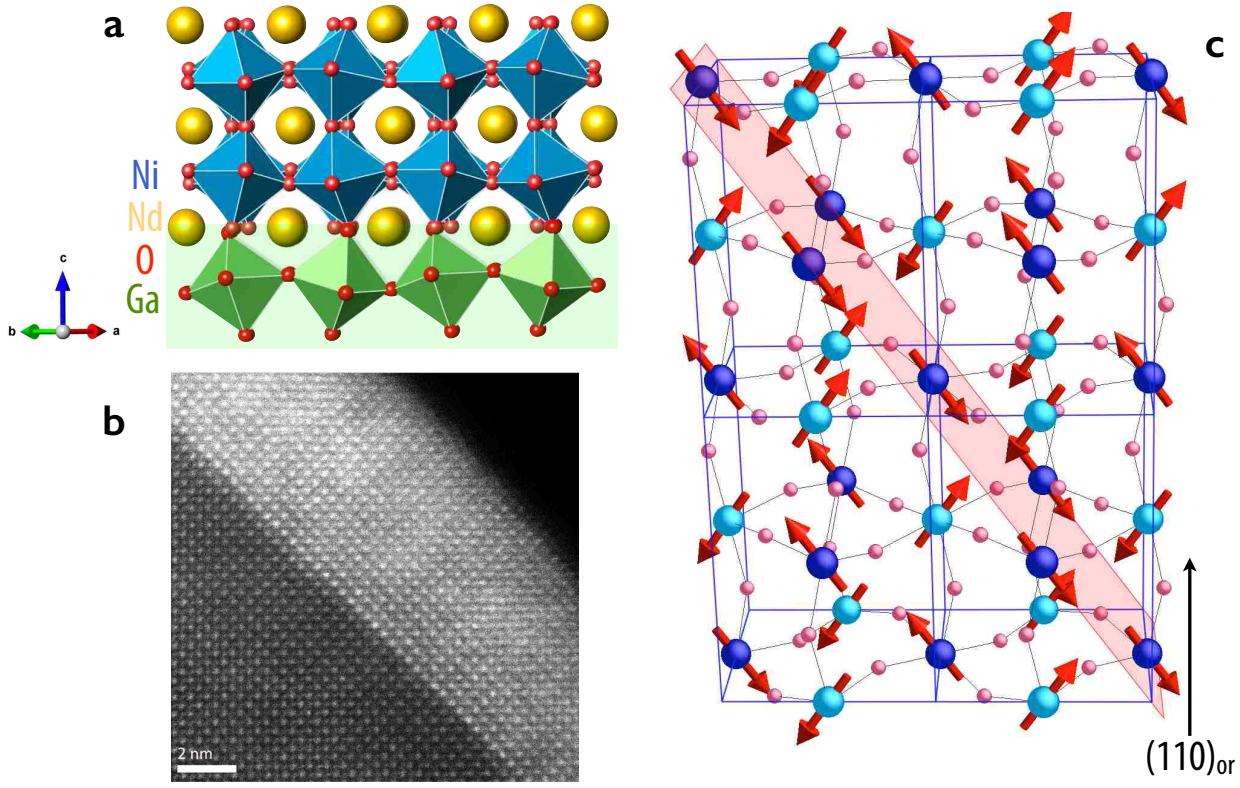

Figure 4.5: (a) NNO on NGO substrate heterostructure. (b) TEM image of NNO on STO showing high structural quality of NNO ultra thin films. (c) E′-type antiferromagnetic ordering in the nickelates with the $(111)_{pc}$ plane highlighted. The dark and light blue spheres represent the nickel sites with charge of $3 \pm \delta$[13, 14].

be stabilized with no CO and a very weak MIT in $PrNiO_3/PrAlO_3$ superlattices[145, 146]. However, the nickelates do not entirely comply with the requirements for a Slater transition in several ways, notably in the first-order nature of the MIT and the large spectral weight transfer $\sim$ 5 eV[141]. Thus the early rare-earth nickelates do not distinctly fit any of these models, and a definitive mechanism triggering the MIT has remained elusive. Theoretical work on the nickelates also expounds the rather convoluted view of the MIT, with numerous contradicting results displaying both the need for CO[40, 147] and the possibility or even the necessity for the absence of CO[39, 126, 148, 149] with various roles for the AFM. Thus, experimentally to date, these systems have been shown to process a myriad degrees of freedom preventing identification of a true origin of the MIT. However, epitaxial strain has been shown in the past to restrict the degrees of freedom available to a system and is a possible route to further our understanding of this transition.

Here we discuss the results of both hard and soft resonant x-ray scattering (RXS) on ultrathin NNO films grown on single crystals of orthorhombic $NdGaO_3$ (NGO), Fig. 4.5(a) which are able to probe both charge and spin ordering directly, elucidating the presence and temperature dependence of these transitions. The ultra thin geometry is an ideal candidate for this investigation as the lattice is fully strained with no relaxation, leaving the bulk-like room temperature *Pbnm* symmetry and circumventing the dichroic effects known to greatly complicate the interpretation of RXS data[17, 123].

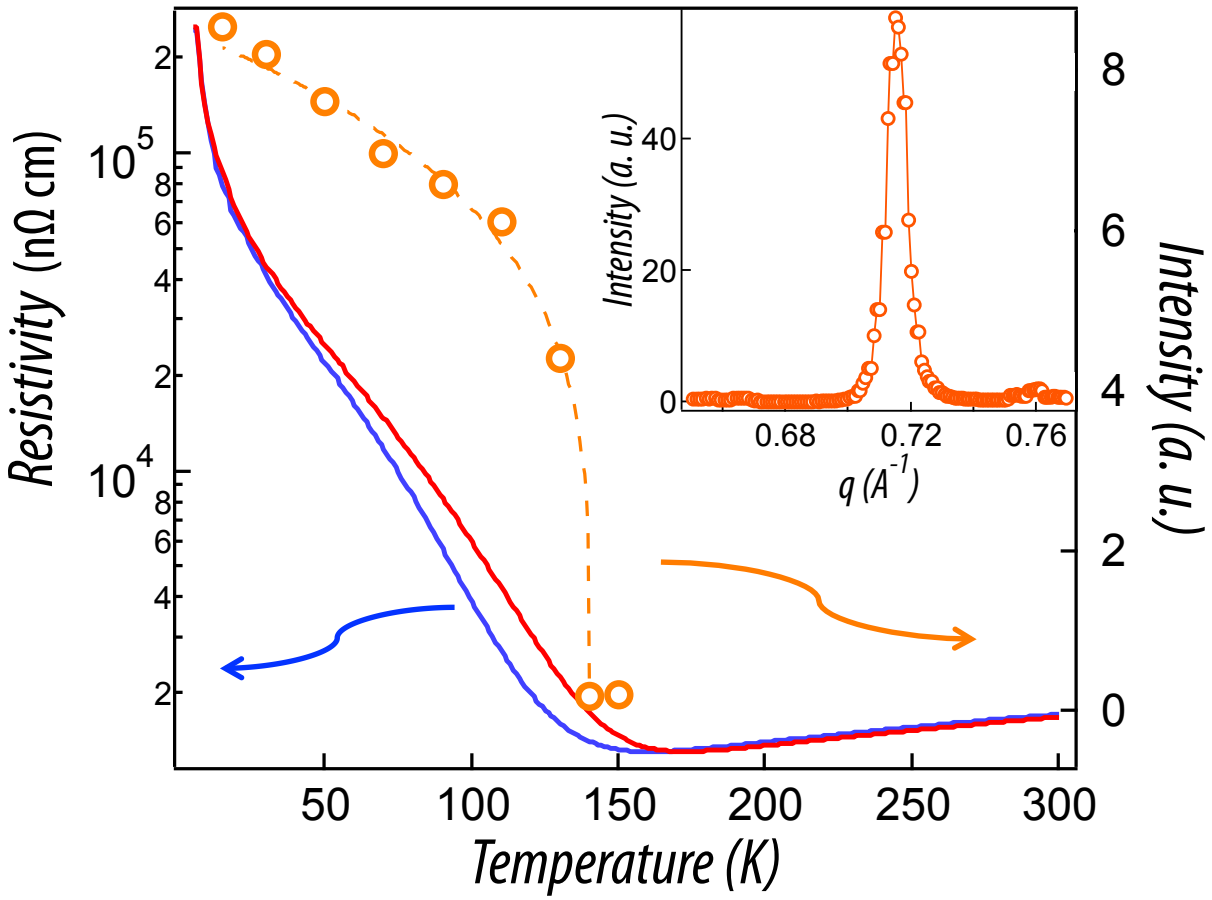

Figure 4.6: Left axis: Temperature dependence DC transport for cooling (blue) and warming (red) cycles. Right Axis: Temperature dependence of the forbidden Bragg peak intensity corresponding to the magnetic order parameter. The inset shows the measured scattering above and below the MIT[12].

The magnetic ordering in the nickelates has received widespread attention due to the unusual stacking of ferromagnetic planes along the $(1\ 1\ 1)_{pc}$ (pc = psuedocubic) direction that are coupled anti-ferromagnetically to one another, a non-collinear periodic behavior

and a magnetic unit cell consisting of 4 structural unit cells, shown in Fig. 4.5(c)[13, 14]. This transition is commensurate with the first-order MIT in bulk NNO, which occurs at $\sim$ 150K, as seen in Fig. 4.6, solid lines, data previously shown here[12]. The right axis, circles, displays the results of the soft x-ray resonant scattering at the $(1/2\ 0\ 1/2)_{or}$ (or = orthorhombic) reflection with the energy tuned to the Ni L_3 edge (852 eV). This Bragg forbidden reflection corresponds to a 4-fold unit cell repetition in the $(1\ 1\ 1)_{pc}$ direction. As can be seen, the intensity of the forbidden peak tracks well with the MIT, sharply rising above the background noise at around 140K and steadily increasing until beginning to stabilize at low temperature. This is in good agreement with previous studies on thick $NdNiO_3$ films and bulk powders[13, 142]. The inset displays the measured scattering well below the MIT. Despite the ultra thin nature of these films (15uc), these results strongly imply that the bulk E′-type magnetic ordering is conserved, showing this phenomena tracks with the MIT in the nickelates despite bi-axial strain ($\sim$ 1.4 %) *and* quantum confinement. With the typical AFM ordering and first-order MIT observed, charge ordering and the accompanying lattice symmetry change are expected to occur as in the bulk.

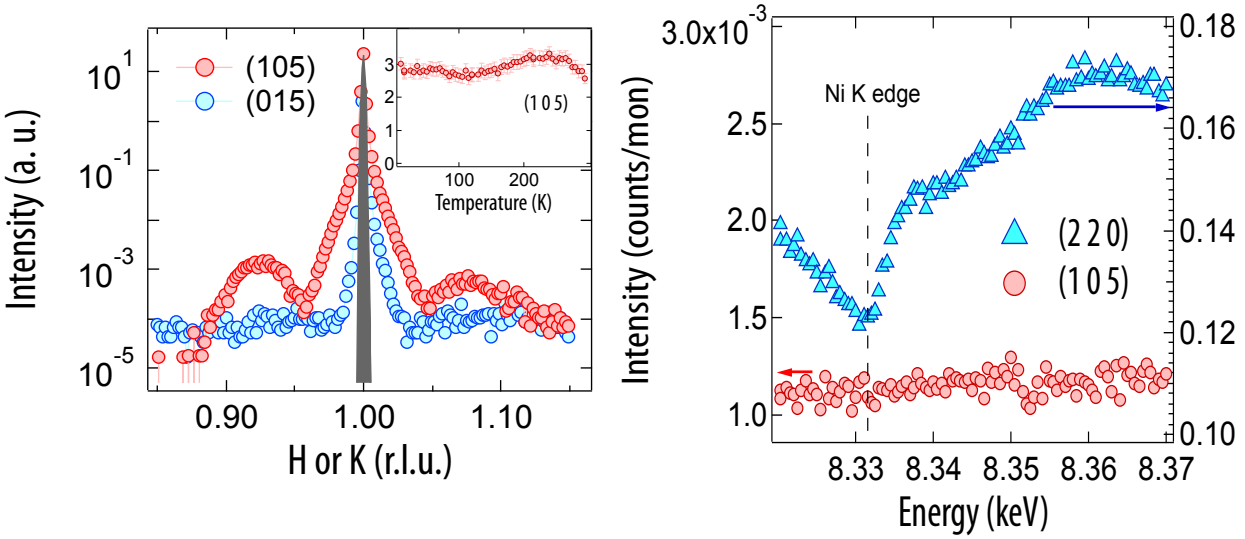

Figure 4.7: (a) Scattering around the $(1\ 0\ 5)_{or}$ and $(0\ 1\ 5)_{or}$ peaks at low temperature ($\sim$ 10 °K). The inset show the measured intensity of the $(1\ 0\ 5)_{or}$ peak for several temperatures crossing the MIT. (b) Ni L_3-edge resonance scans at the $(1\ 0\ 5)_{or}$ and $(2\ 2\ 0)_{or}$ peaks.

In recent years it has been found that, while RXS is a powerful tool for investigating

charge ordering, very careful attention to detail is required to unambiguously identify charge ordering as was found for the maganites, as very small distortions of the oxygen octahedra lead to dichroic terms in the scattering tensor, leading to resonance that can easily be misinterpreted as being the signature of charge-order[123, 150, 151]. Previous studies on thick NNO films have found charge ordering by successfully using azimuthal dependence and polarization analysis to firmly establish the presence of the charge ordered state[123]. With this in mind, we investigated the $(0\ 1\ 5)_{or}$ and $(1\ 0\ 5)_{or}$ reflections, Fig. 4.7(a) and (b).

Fig. 4.7(a) displays scans along the L reciprocal space vector (L-scan) at the $(0\ 1\ 5)_{or}$ and $(1\ 0\ 5)_{or}$ peaks. The $(1\ 0\ 5)_{or}$ peak is symmetry allowed for orthorhombic NNO, as a Bragg peak corresponding to the Nd sub-lattice, thus the film peak with Kisseg fringes is entirely expected (the sharp peak at 1.00 being the substrate). According to Staub *et al*, this peak has no Ni component until the low temperature phase is obtained, at which point the charge ordering should break the *Pbnm* symmetry; this leads to a Ni contribution to this peak causing a change in signal strength, especially so with the x-rays tuned to the Ni K-edge (8.34 keV)[123]. Surprisingly, as the temperature was moved across the MIT no change was observed, inset of Fig. 4.7(a). This implies that neither charge ordering nor the associated symmetry breaking occurs at all across the transition. Furthermore the $(0\ 1\ 5)_{or}$ peak, which is not symmetry allowed for *Pbnm* and is therefore much weaker, does not appear at any temperature (the substrate peak here arises due to defects).

Energy scans at the $(1\ 0\ 5)_{or}$ peak corroborate this picture, Fig. 4.7(b), showing that *no resonance signature is observed below the MIT* for the $(1\ 0\ 5)_{or}$ peak. This is in stark contrast to the previous studies on both thick films and powders where strong, temperature dependent resonance was shown to convincingly track with the MIT[124, 139, 140]. To further verify this, the $(2\ 2\ 0)_{or}$ reflection shows the expected Ni resonance signal as the Ni contribution to this structural peak is symmetry allowed for Ni in *Pbnm* symmetry, confirming the Ni K-edge is present and observable in our experimental setup. These results confirm that (i) no stretching / compressing distortion of the NiO_6 octahedra occurs and the bulk, metallic phase *Pbnm* structure is conserved, if this did occur dichroic terms would appear within the scattering matrix leading to a resonance signal[123, 124], and (ii) *no charge ordering occurs* in these ultra thin films as no Ni resonance is observed. These results indicate that these ultra thin films have stabilized a previously unidentified ground state. Interestingly, the case of a phase transition without a structural symmetry change can only

be first order, as we observed here, and is rare, with the most prominent example being the liquid-gas transformation. For perovskites, only in the case of Cr-doped V_2O_3 is this behavior found; in this case, the Mott MIT transition was shown to display the universal properties of the liquid-gas transition[152]. The observation of a strong first-order MIT without the presence of charge ordering has not been previously reported experimentally on any of the perovskite nickelate systems to the best of our knowledge.

While this ground state has not been experimentally observed, several theoretical works have predicted this phase, however with several caveats. Two works utilizing different theoretical methods by Lee *et al* have shown the CO is slaved to the spin density wave (SDW) in the weak coupling limit, and can indeed disappear in certain cases; in particular, using Landau Theory, they were able to show that restricting the nickelates to the thin film regime, as was done in this study, can remove CO. Both works find that the SDW can either be bond- or site- centered, with the bond centered wave giving no CO. This discrepancy with experiment is cleared up by the presence of the orthorhombic distortion, which displaces the SDW leading to a fractional CO[39, 40]. However, when confined to ultra thin films and with a small enough contribution of the orthorhombic distortion to the free energy, the applied epitaxial strain is able to suppress the CO; this agrees with our results, as the ultra thin films are fully epitaxial and lack CO, however their phase also switches the Q-vector of the magnetic ordering, which was not observed for our sample. Beyond this work, Park *et al* also showed within DFT + dynamical mean field theory (DMFT) that, despite the near Fermi-energy imbalance in the spectral weight between the two Ni sites, the total valence of Ni on both sites is nearly identical, with the two different sites instead hybridizing with O disparately, leading to an $S = 1$ state on the larger octahedra at the Ni site and an $S = 0$ state forming due to AFM coupling with the O holes (Ni being in the $3d^8\underline{L}$ state). However, when *Pbnm* symmetry was used instead of $P2_1/n$, a metallic state was stabilized disparate to our results. Finally, Prosandeev *et al.* utilized DFT with the generalized gradient approximation to show that CO may actually be a direct consequence of an O_6 breathing distortion, which lowers the symmetry to monoclinic. In the case of high Hubbard U, high epitaxial strain, and the maintaining of orthorhombic symmetry, as shown experimentally here, no CO was found[149]. However, key differences are still present, such as the strain in our work (1.3%) is much lower then what was used ($\sim 9\%$).

Finally, using LSDA + U calculations, Yamamoto *et al* obtained results that are in the best agreement to what was observed here[148]. While some of the previously discussed

reports predicted the absence of CO, various inconsistencies with our results arose. However, Yamamoto *et al* calculated the electronic and magnetic structure in orthorhombic NNO and found an insulating state with no Ni CO (as expected for equivalent Ni sites). In contrast, they found the magnetic space group is monoclinic due to different spin density polarizations around two O sites that would be equivalent in the *Pbnm* space group. Most importantly, this symmetry breaking, driven by the Hubbard U, opens the insulating gap, with U values ranging from 7 to 4 eV, which agree well with our previous work on NNO films grown on $SrTiO_3$. This magnetic space group symmetry breaking on O would not lead to the observance of a peak at the $(0\ 1\ 5)_{or}$ and $(1\ 0\ 5)_{or}$ peaks or Ni resonance therein, as was observed experimentally. Interestingly, while in the bulk structural symmetry lowering to $P2_1/c$ is observed in contrast to these LSDA results, the advent of epitaxial strain is able to stabilize this state. It is likely the orthorhombic symmetry of the substrate prevents divergence of the β angle from 90 °, as this angle is partially in-plane , preserving the orthorhombic symmetry. The resulting ground state, observed experimentally for the first time in this work, can therefore be well understood by virtue of LSDA + U theory, showing that the bulk-like MIT and AFM can be obtained without the lowering of the symmetry. Future experiments, such as x-ray magnetic linear dichroism (XMLD), to directly observe the spin density variation on the O sites could further confirm the compliance of our experimental observations and the theoretical prediction of Yamamoto *et al*.

In conclusion, the lack of any signal indicating CO for our ultra thin NNO films at any temperature contrasts with the conclusions for thicker films and powder samples, and directly challenges the assertion that the MIT in these systems is dependent on the CO transition. Going further, the measurements also show that no structural symmetry transition away from *Pbnm* occurs despite the first order MIT and AFM. Contrary to the findings for CO, the magnetic ordering is compatible with previously reported experiments. This is in good agreement with theoretical calculations showing that the lowering of the symmetry group of the magnetic order, driven by the Hubbard U, can stabilize the insulating state. These findings lead us to conclude that a new phase with a reduced degree of freedom has been stabilized for the first time and sheds light on the nature of the MIT in these materials, revealing that the AFM plays a far more central role then previously suspected.

4.3.2 Symmetry lowering and charge order in $EuNiO_3$

Transition metal oxides host a vast array of collective phenomena with enormous potential for use in next generation electronic devices, e.g. high temperature superconductivity, collosal magnetoresistance, metal-insulator transition, charge ordering (CO), etc[42, 56, 89, 90, 153]. In particular, electric field induced changes in the CO state, where the modulated charge density acquires a periodic pattern instead of the usual uniform distribution typically leading to insulating behavior, has received substantial attention lately and been implemented in several devices[131, 153, 154, 155, 156, 157]. In the ferrites, for instance, the application of an external electric field was found to induce a phase transitions to a metallic state with a resistance change of several orders of magnitude, allowing their incorporation into devices[156, 157]. These devices typically require ultra thin films or nanoparticles of materials making the study of size effects of paramount importance to future functionality. Surprisingly, it was found that the bulk CO transition is suppressed in the nano-limit for some CMR manganites[158, 159]. Further, a device of any practical importance typically needs to operate at room temperature, while CO is typically a low temperature phenomena. Thus a material is required that fulfills all of the criteria, i.e. displays charge ordering, maintains this transition in nanometer size applications, and operates ideally at room temperature.

As a prototypical TMO perovskite system, the rare-earth nickelates with chemical formula $RENiO_3$ (RE = Pr, Nd, Eu, Y, etc) utilize Ni ions in a low spin, ionic $3d^7$ ($t_{2g}^6 e_g^1$ state), with a strong covalence with oxygen placing these systems firmly in the charge transfer regime with a significant $3d^8\underline{L}$ component of the ground state[17]. This class of materials has received significant attention recently due to the MIT [17], E′-type anti-ferromagnetic transition (AFM)[125], symmetry transition [17], predicted high T_c superconductivity in heterostructure with $LaAlO_3$[129], potential for device applications[130, 131, 154], and the charge-ordering transition [123, 124, 139, 140]. Indeed, devices utilizing $NdNiO_3$ (NNO), in particular, have already been realized, including electric field control, however the low transition temperature ($\sim$ 150K) limits the practicality of such systems[130, 131]. The rock-salt CO structure is shown in Fig. 4.8(a) and the E′-type anti-ferromagnetic structure is shown in Fig. 4.8(b). In the nickelates, the CO transition is also found routinely in the bulk, but, as in the CMR manganites, has been shown to be suppressed under certain conditions, i.e. epitaxial strain, for NNO[43, 160, 161]. For ultra-thin films, it was found the substrate is able to "pin" the symmetry in the non-CO *Pbnm* state, analogous to the effect of surface

tension in $La_{0.5}Ca_{0.5}MnO_3$[158]. As changes in the ground state could render materials futile for applicability, it is important to find ways to mitigate these reduced dimensionality effects. Within the nickelates, one possible route towards this goal is the use of a RE ion of smaller radius, which increases the distortion of the lattice and correspondingly the T_{MIT} at which CO arises in the bulk. This scheme could either recover the typical bulk ground state or show the two-dimensional geometry forbids it's occurrence limiting the phase's potential utility in future device applications.

In this work, ultra thin films (14 unit cells, u.c.) of $EuNiO_3$ (ENO) on orthorhombic $NdGaO_3$ (NGO) substrates were probed by resonant x-ray scattering (RXS) in the hard and soft x-ray regime to determine the alteration of the ground state due to the highly two-dimensional geometry[63, 64]. Structural diffraction established that the film was of high quality, proper thickness, and was *single-domain* with the same orientation as the substrate. Measurements of the $(0\ 1\ 1)_{or}$ (or refers to orthorhombic structure; pc = pseudocubic) and $(\frac{1}{2}\ 0\ \frac{1}{2})_{or}$ peaks in both diffraction and resonance modes were utilized to establish the presence of the bulk-like CO and E′-type AFM orderings, respectively. Our results indicate these films display bulk-like ground states in contrast to NNO, likely due to the larger distortion of the lattice destabilizing the substrate-induced symmetry pinning. These findings highlight the excellent plausibility of fabricating oxide based devices employing room temperature charge ordering.

Ultra thin ENO samples were grown on NGO $(110)_{or}$ by pulsed laser deposition as described in Ref.[4]. Resonant x-ray scattering (RXS) measurements were acquired at both the 4.0.2 beam line of the Advanced Light Source, Lawrence-Berkeley National Laboratory (soft RXS), and the 6-ID-B beam line of the Advanced Photon Source, Argonne National Laboratory.

Structural quality for these ENO thin films was established previously with a laboratory based Materials Research Diffractometer system[4]. Fig. 4.8(c) displays scans across the $(0\ 0\ L)_{pc}$ truncation rods with synchrotron based diffraction showcasing the high flux and resolution available at the 6-ID-B, with 10^8 counts observed for the 14 uc film. The structural quality is clearly evident from the appearance of Kisseg fringes spanning the $(001)_{pc}$ truncation rod and film. The spacing of the Kisseg fringes gives a film thickness of ~ 5.3 nm, corresponding to 14 u.c. of ENO as was deduced from reflection high energy electron diffraction (RHEED) oscillations during the growth. The high flux is of particular importance due to the relatively weak reflections used to probe CO. Beyond this, another basic indication of

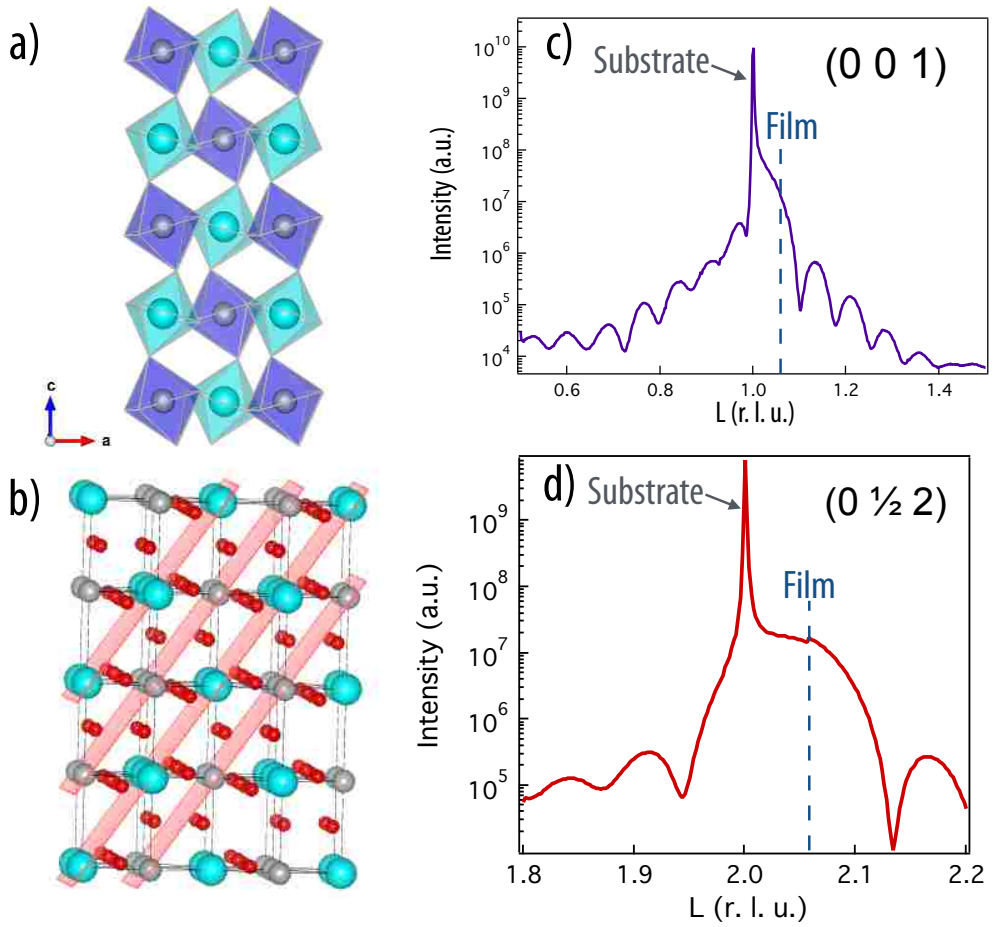

Figure 4.8: a) Charge ordered rock salt crystal structure with exaggerated $Ni^{3\pm\delta}$ radius variations. b) Crystal structure showing $(1\ 1\ 1)_{pc}$ E′-type anti-ferromagnetic planes. (small red spheres are O, grey and cyan are Ni) c) L-scan through the (001) and (002) truncation rods showing the high quality of the ultra-thin films. d) L-scan around the $(0\ \frac{1}{2}\ 2)$ truncation rod.

quality is the orientation of the orthorhombic c-direction of the film relative to the substrate, which corresponds to a doubling of the pseudo-cubic unit cell. The NGO substrates used for growth are cut to have the $(1\ 1\ 0)_{or}$ direction out-of-plane, giving in-plane directions of $(1\ \text{-}1\ 0)_{or}$ and $(0\ 0\ 1)_{or}$. Thus, there exists a half-order peak in either the $(H\ 0\ 0)_{pc}$ or $(0\ K\ 0)_{pc}$ direction corresponding to the orthorhombic c-direction for both the substrate and film. Our scans across the $(0\ \frac{1}{2}\ 2)_{pc}$ half-order peak show a clear substrate and film peak, Fig. 4.8(d). Subsequent attempts to locate the $(\frac{1}{2}\ 0\ 2)_{pc}$ found no peaks and significantly reduce background. This indicates the orthrhombic c-direction is in the $(0\ K\ 0)_{pc}$ direction for both the film and the substrate, with no mixing of $(H\ 0\ 0)_{pc}$ oriented domains. This point is crucial for investigating CO as domains with different c-orientations will mix the

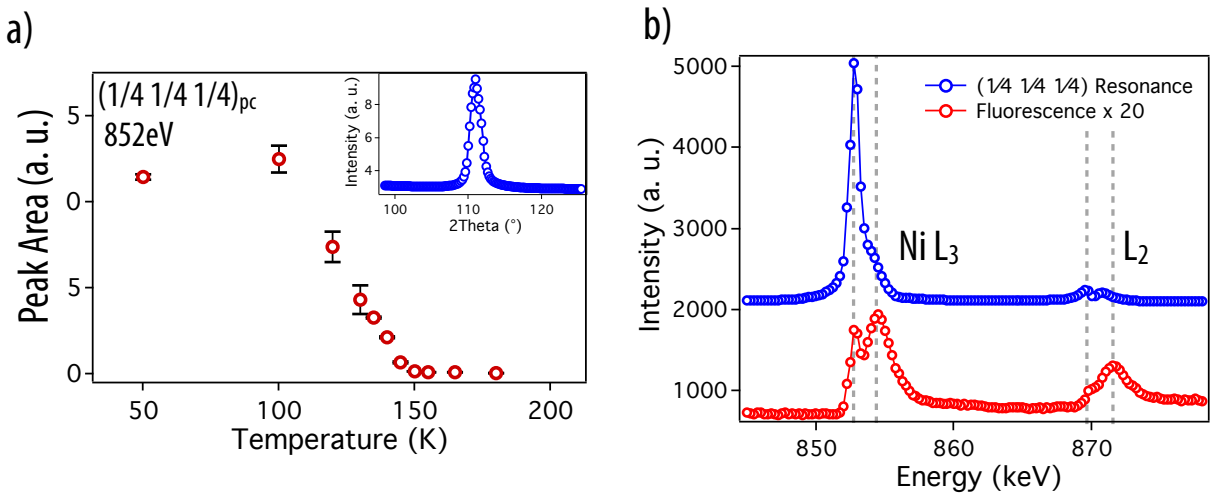

Figure 4.9: (a)Temperature dependence of the forbidden Bragg peak intensity corresponding to the magnetic order parameter. The inset shows the measured scattering at 50K. (b) 50K resonant and fluorescent measurements of the Ni L_3 and L_2 edges. The florence signal is enhanced 20x and the resonance data vertically offset for clarity. Dashed lines are guides to the eye.

signal from the A-site allowed (H 0 L)$_{or}$ and forbidden (0 K L)$_{or}$ peaks, thus adding a large Thompson scattering background which can obscure the resonant term.

Previous studies by several groups, including our recent work on NNO, have shown the E′ -type AFM order in the nickelates is very robust and may even play a critical role in the MIT transition in these less distorted nickelates[13, 125, 161]. With ENO, the separation of the MIT and the AFM transitions is nearly 300 K allowing separate investigation of both. The E′ -type AFM gives a 4x4x4 repeating ordering in terms of the psuedocubic unit cell, thus this ordering can then be probed via the $(\frac{1}{4}\ \frac{1}{4}\ \frac{1}{4})_{pc}$ peak, which corresponds to the $(\frac{1}{2}\ 0\ \frac{1}{2})_{or}$ peak.

2θ scans about this peak revealed a strong peak at low temperature, Fig. 4.9(a) inset. Temperature dependence of this peak was also measured, with the fitted area shown in Fig. 4.9(a). A clear transition to the magnetically ordered state is observed around 150K. Thus, the magnetic Bragg peak corresponding to the bulk-like E′ -type AFM order was observed despite the ultra-thin nature of the films displaying the robustness of this transition down to less then 4 full magnetic unit cell thickness.

Beyond the Bragg reflection, low temperature resonance scans at the $(\frac{1}{4}\ \frac{1}{4}\ \frac{1}{4})_{pc}$ peak also reveal important information about the sample. The use of an in-situ 2D detector allows

simultaneous collection of both the on Q and background scattering, which corresponds to the resonant peak and flouresence data, respectively, shown in Fig. 4.9(b). The typical Ni L_3 and L_2 features are seen for the fluorescence data, with the higher energy peak corresponding to the Ni 3+ state around 855 eV and the lower energy multiplet split peak, characteristic of the insulating state, around 853 eV as seen previously[4].

The resonance of the L_3 edge, besides indicating a strong Ni contribution to the observed magnetic Bragg peak, also can be used to predict the degree of CO in the sample[125, 13]. Scagnoli *et al* used a configuration interaction model to show the value of δ strongly influences the line shape of the resonant peak. Interestingly, Bodenthin *et al* found, for $RNiO_3$ powder samples spanning a large range of rare earth ions, no deviation in δ. For our $EuNiO_3$ ultra thin films, surprisingly, the line shape for the σ incident light is nearly identical, and, based upon the difference observed for the calculated spectra of $\delta = 0.41$e, is within the 0.05e range found for all of the various $RNiO_3$ bulk powders. Thus, combing the results of the $(0\ 1\ 1)_{or}$ CO peak and the $(\frac{1}{4}\ \frac{1}{4}\ \frac{1}{4})_{pc}$ magnetic peak, it is clear the CO in this thin film sample maintains a bulk-like value of $\delta = 0.32 \pm 0.05$e despite the highly constraining two-dimensional geometry and lattice pinning found for NNO thin films[160, 161]. However, the low temperature of the AFM transition precludes investigation of the room-temperature CO behavior, an important factor in determining the utility of use in devices.

Having established the high structural quality, single domain phase, and the typical magnetic transition, the temperature dependence of the $(0\ \mathrm{K}\ \mathrm{L})_{or}$ peaks, associated directly with charge order, can be investigated[123, 124, 139, 140]. Fig. 4.10 shows the results of resonant energy scans around the $(0\ 1\ 1)_{or}$ peak. As can be seen a clear energy dependence is observed at the Ni K-edge with no apparent temperature dependence. While the scattering around the Ni K-edge is clearly due to the resonant term of the total scattering factor, the off-resonance scattering indicates some component of the Thompson scattering term. As with the resonant peak, no temperature dependence was observed for this contribution. Further analysis, taking the ratio of the peak at 8.348 keV to the background Thompson scattering, inset of Fig. 4.10, confirms the lack of any significant temperature dependence for this peak. For bulk ENO, the 470K MIT transition, which cannot be reached with this setup, suggests this lack of temperature dependence should be the case.

These results are quite surprising as the ultra thin nature of the films, only 5.3 nm in the growth direction, is known to influence the band structure which could then influence the CO parameter[12, 52]. Further, previous work on NNO ultra thin films showed the

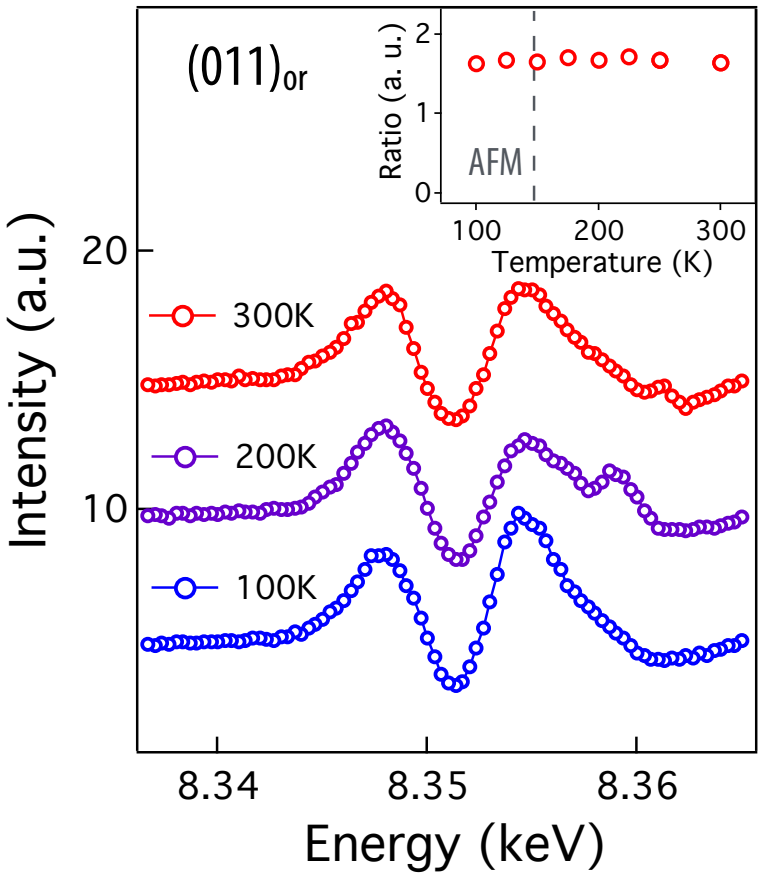

Figure 4.10: Resonant scattering at the $(0\ 1\ 1)_{or}$ peak at various temperatures. Data offset for clarity. The inset shows the ratio of the peak around 8.348 keV to the background at 8.34 keV across the AFM transition up to room temperature.

substrate is able to supress the transition to monoclinic symmetry, leading to CO. Due to the higher distortion in ENO, it is not entirely surprising that the CO indeed persists, however it is quite remarkable that, based upon the Ni L_3 edge resonant scattering, the degree of charge disproportionation appears unchanged from the bulk value. Thus, we find the higher distortion in this nickelate incorporating a smaller RE ion, Eu, is able to recover the bulk-like phase transitions that were suppressed for NNO in the same two-dimensional geometry. This indicates that the relative phonon coupling strength between ENO and NNO is strongly modulated by the degree distortion of the orthorhombic structure. These findings reveal a possible route to overcome the ground state suppression that can occur when materials are reduced to a nano-scale geometry recovering their utility for device functionality.

In conclusion, we synthesized ultra thin films of ENO films on NGO substrates to investigate the stability of the AFM and CO transitions against the ultra thin geometry via

hard and soft XRS. An AFM transition is found to occur near the expected temperature with the Q-value corresponding to the bulk-like E′ type ordering, as in the bulk. Interestingly, the CO δ parameter, derived from magnetic scattering, was found to be the same as was reported for both bulk and thick films of various $RNiO_3$. Thus, despite the ultra thin geometry and electronic bandwidth modifications, our measurements revealed the CO and AFM transitions remain bulk-like. Importantly, CO is observed at room temperature giving these films potential utility for electric field controlled devices.

4.4 Conclusion

To summarize, our various measurements show the profound effect of epitaxial strain on the MIT and the various orderings on the rare-earth nickelates. Both $NdNiO_3$ and $EuNiO_3$ ultra thin films showed a remarkable ability to grow with large lattice mismatches spanning both compressive and tensile strain up to 4%. Correspondingly, transport measurements on both revealed compressive strain can reduce T_{MIT} significantly, with $NdNiO_3$ showing no MIT at even $\epsilon = 0$, and $EuNiO_3$ requiring ϵ = -2.4%. On the tensile side, both systems recover the bulk-like insulating ground state. Resonant soft x-ray scattering revealed both systems recover the E′-type AFM under tensile strain, and both can obtain the paramagnetic insulating state as well, with varying strain requirements.

Resonant hard x-ray scattering revealed the most interesting repercussion of the ultra-thin geometry and lattice mismatch, namely the suppression of the charge order transition in NNO, as oppose to ENO which maintains the bulk-like charge disproportionation, however we were not able to measure above the MIT (470K) to ascertain whether the peak is due strictly to dichroic distortions or charge order. We conjectured, with past theoretical support, the $NdGaO_3$ substrate is able to suppress the structural monoclinic transition in the NNO film, leading to a magnetic symmetry breaking which future work hopes to uncover. This indicates this system displays a Mott transition with no accompanying structural transition, a result only seen previously in Cr doped V_2O_3[152]. In the case of ENO, we conjectured the larger structural distortion is able to overcome the substrate induced symmetry locking and relax to a more bulk-like state.

5 Designer phases in Nickelate Heterostructures: Superlattice integer control

In this chapter, we explore the final and, in many ways, the most intriguing emerging method for engineering the phase space of materials. This method involves the alternating growth of two separate materials to form a heterostructure or superlattice. Specifically, we explore how this structural design affects the metal-insulator transition (5.2) and the various orderings present in the constituent materials (5.3). Our preliminary results show the utility of this method for drastically altering a material's phase space and reveal the importance of the effect of the broken symmetry on the material's properties.

5.1 Introduction

Designer phases of nickelates through use of integer layering of two separate nickelate compounds, creates a superlattice, that is then repeated multiple times. Electronically, these designer phases display excellent tunability, allowing the metal-insulator transition temperature to be controlled. Symmetry changes also become significant, with the dominant layer imposing it's own symmetry group upon the entire lattice, causing a sharp change in physical properties with small changes in interior thicknesses. Magnetically, the bulk-like E'-type anti ferromagnetism is found to be preserved for all materials in the insulating ground state. Most interestingly, it is found that the periodic structure of the superlattice can alter the energetics dictating the bulk-like charge order and can either enhance it or remove the transition entirely.

5.2 Transport modulation in digital superlattices

The distorted member of the series with RE= Y, Gd, Eu, Sm undergoes a first order metal-insulator transition (MIT) at high temperature, accompanied with a structural transition from orthorhombic to monoclinic phase[17, 38]. They also undergo a second order magnetic transition from a paramagnetic insulating (PI) to E‘ type antiferromagnetic insulating state (AFI) at lower temperature. While in the bulk the structural transition, MIT and magnetic ordering happens simultaneously for the intermediate member of the series (RE = Nd, Pr), the end member $LaNiO_3$ with rhombohedral structure remains metal-

lic down to the lowest temperature without any transition. As the insulating state with monoclinic structure has two sets of inequivalent Ni sites, one with smaller and another one with larger Ni-O bonds, the insulating state has been also associated with a charge disproportionation[38, 123, 139, 140]. As several transitions happen simultaneously, it is not possible to identify which one is the progenitor and which are ones are slaved to the primary transition, demanding alternative ways of engineering the electronic properties of these systems.

One of the most powerful methods for ground state engineering with correlated oxides, which has only become possible in the last decade, is the layer-by-layer synthesis of two dissimilar materials to form a new quantum solid, i.e. superlattice[162, 146, 145, 163]. In order to find out whether the structural symmetry change (while all Ni are equivalent in the orthorhombic metallic phase, the monoclinic insulating phase has two inequivalent Ni sites) is a prerequisite for this fascinating MIT in nickelates, we have combined two distant members of the series $EuNiO_3$ (ENO) and $LaNiO_3$ (LNO) to form 2 uc ENO/ 1 uc LNO and 1 uc ENO/2 uc LNO (uc= unit cell in pseudo cubic notation) superlattices. As the parent compounds ENO and LNO have crystal structures with very different symmetry, the resulting materials have two kinds of Ni by design, Ni(1) : located at the interface and Ni(2): away from the interface (Fig. 1(a)).

[2ENO/1LNO]x12 and [1ENO/2LNO]x12 SLs were grown on orthorhombic $NdGaO_3$ (1 1 0) [$\equiv$ pseudo cubic (0 0 1)] substrates by pulsed laser interval deposition [70, 74, 132] and the growth was monitored by in situ RHEED (reflection high energy electron diffraction). While the layer by layer growth sequences have been shown schematically in Fig. 1(b), the growth conditions can be found in our earlier publications[74]. All of the diffraction peaks through out the manuscript will be described with respect to the pseudocubic settings unless specified otherway. X-ray diffractions (XRD) pattern for the (0 0 L) peaks and various half order peaks were recorded using the six-circle diffractometer at the 6-ID-B beam-line of the Advanced Photon Source (APS) at Argonne National Laboratory. X-ray absorption spectroscopy (XAS) at the Ni $L_{2,3}$ edges measurements were taken at the 4-ID-C beam line of APS in bulk sensitive total fluoresce yield (TFY) mode. Magnetic ordering was investigated by resonant x-ray scattering on Ni L_3 edge at Advanced Light Source (ALS) of Lawrence Berkley National Laboratory. Transport properties were measured using a four probe Van Der Pauw geometry with a Quantum Design physical property measurement system (PPMS).

The essential criteria for the described work was to grow the superlattice in a layer-

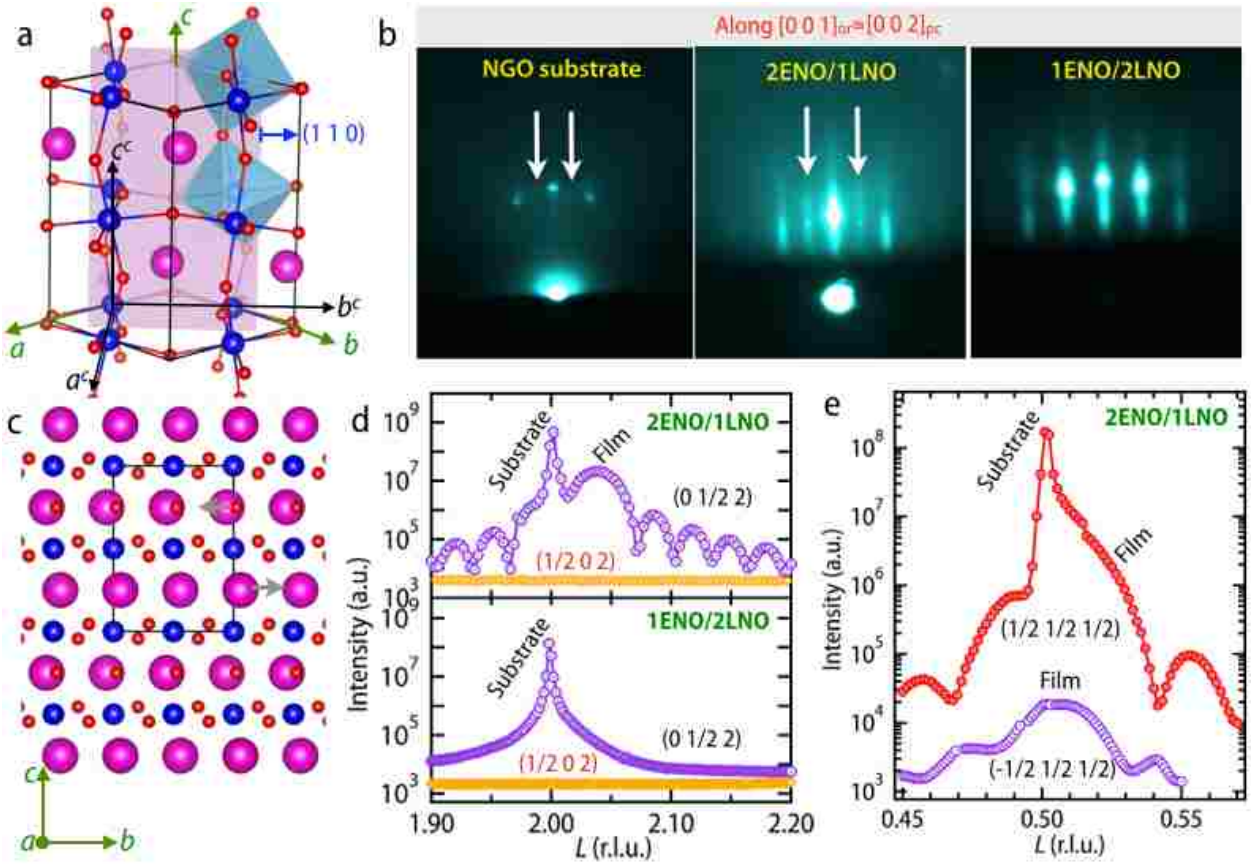

Figure 5.1: (a) Schematic crystal structure of 2 uc RENiO$_3$/1 uc RE'NO superlattices grown along pseudo cubic [001] direction. (b) Schematics of deposition sequence of 2ENO/1LNO and 1ENO/2LNO SLs. (c) The intensity variation of the specular reflection in RHEED during the growth of 2ENO/1LNO SL (laser frequency used for the growth was 18 Hz). (d) A long (0 0 L) x-ray diffraction scan for 2ENO/1LNO SL.

by-layer mode so that interfaces between the ENO and LNO layers are very sharp i.e. free from any Eu/La disorder. Fig. 1(c) shows the time dependence of the RHEED specular intensity (RSI) during the growth of 2ENO/1LNO superlattice. The full recovery of RSI after the growth each period (2 uc ENO + 1 uc LNO) highlights the desired layer-by-layer growth of the SLs. An extended (0 0 L) x-ray diffraction scan for 2ENO/1LNO SL is presented in Fig. 1(d). Apart from the ordinary structural peak due to substrate and film, the diffraction pattern also shows the Kiessig fringes, due to the finite film thickness and sharp film-substrate interface. Further, the superlattice satellite peaks (indicated by their order +1, -1), consistent with the desired superlattice period to within an error of $\leq$ 1.5% confirms the absence of any intermixing between ENO and LNO layers. The out of plane lattice constant is found to be 3.793, 3.818 Å (consistent with the larger constant for LNO

vs ENO) for 2ENO/1LNO, 1ENO/2LNO SLs respectively.

After confirming high structural quality, we have investigated the resulting structural symmetry of these superlattices. To this end, Fig. 2(b) and (c) shows the RHEED patterns of the SLs (top most layer is LNO for both systems), recorded at room temperature after completing the annealing procedure. Apart from the usual specular (0 0) and off-specular (0 $\pm$1) reflections, the 2ENO/1LNO SL showed additional half order reflections (0 $\pm$1/2), as highlighted by the white arrows. The presence of these half order reflections, as seen for the NGO substrate suggests the in-plane doubling of the unit cell in the orthorhombic c-direction (Fig. 2(a)) i.e. the structure can be either orthorhombic (e.g. $NdNiO_3$) or monoclinic (*e.g.* $EuNiO_3$) at room temperature. However, the 1ENO/2LNO SL does not show this half order peak, suggesting the rhombohedral type symmetry, similar to single layer LNO films, is conserved even in this heterostructure[17, 38, 164]. During the growth of this SL, it was observed that the half order peak vanishes after the growth of the second LNO layer for each repeat, while it reappears after the deposition of next ENO layer of each repeat. The emergence and evanescence of the half-order peaks as a function of ENO and LNO layer number additionally emphasizes our atomic layer control of structural symmetry.

As RHEED is a surface sensitive technique, the superlattices were further investigated ex-situ by synchrotron x-ray diffraction to check whether the change of the symmetry between these two superlattice is a property of the entire crystal or just a surface effect. The orthorhombic (and monoclinic) ABO_3 perovskites are also accompanied by antiparallel displacement of the A-site as shown in Fig. 2(d) while rhombohedral perovskite does not have this behavior. Such displacement give rise to half order reflections with index (odd even even)/2 in Glazer notations. The results of L scans (at 300 K) around the (1/2 0 2) and (0 1/2 2) peaks are shown in Fig. 2(e)-(f). The presence [absence] of the (0 1/2 2) [(1/2 0 2)] peak for 2ENO/1LNO similar to the NGO substrate, emphasizes that the orthorhombic doubling direction of this superlattice coincides with that of the substrate and the film is also structurally a *single domain* in the c-direction, while the very small difference between the a- and b-lattice constants makes resolving any possible flipping of the a and b directions difficult. The 1ENO/2LNO SL does not show either (0 1/2 2) or (1/2 0 2) reflections highlighting the absence of an anti-parallal displacement, which is consistent with the rhombohedral like structure suggested by earlier discussed RHEED patterns. Thus, the combined results of electron and x-ray diffraction show that the symmetry of the entire crystal structure of 2ENO/1LNO and 1ENO/2LNO SLs at room temperature are different

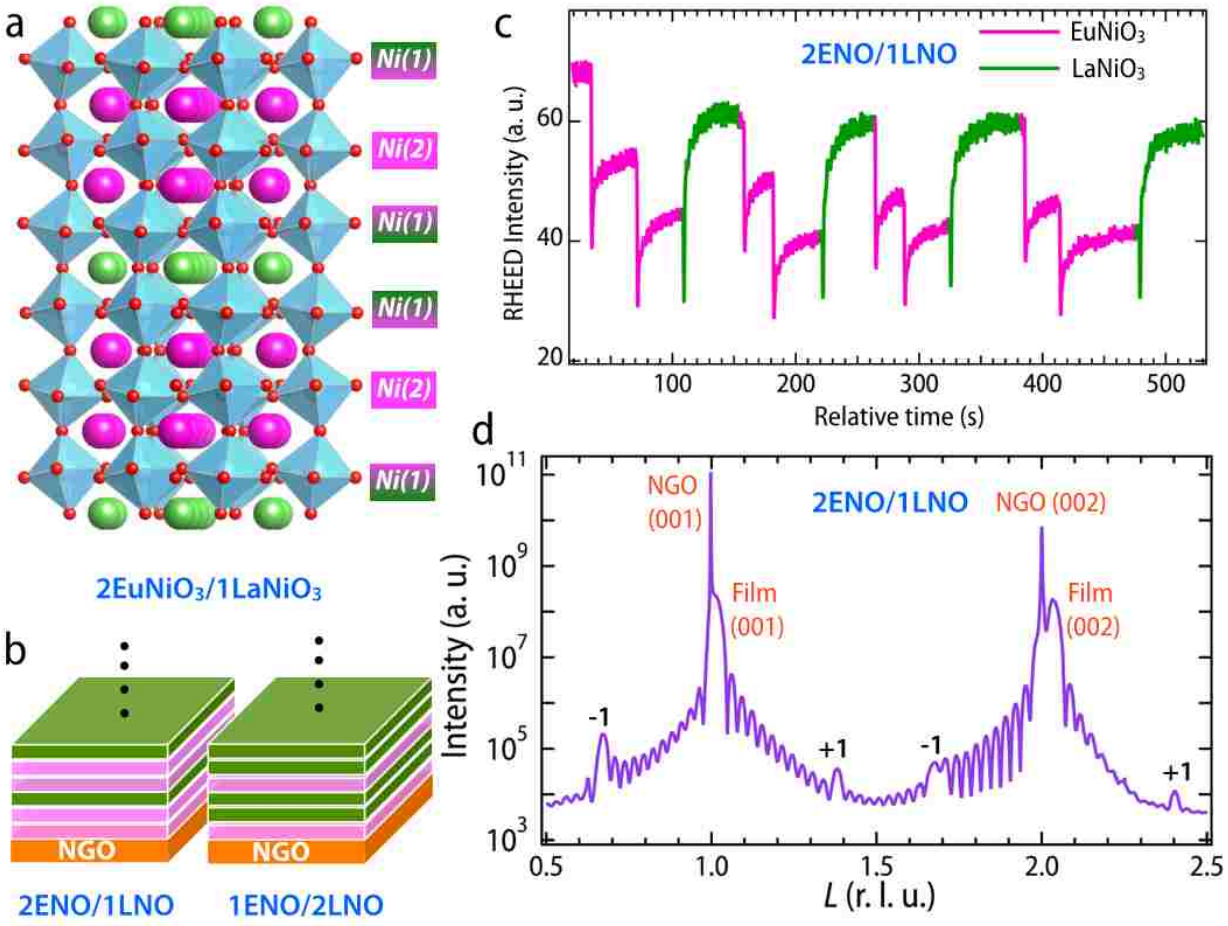

Figure 5.2: (a) RHEED patterns of NGO substrate and SLs. Left panel, unit cells in view of the orthorhombic and cubic symmetries. (b)-(d) XRD L scans of the SLs around the peaks (1/2, 0, 2) and (0, 1/2, 2).

from each other.

In order to further distinguish between orthorhombic and monoclinic symmetry for 2ENO/1LNO SL, another set of half order peaks were measured at room temperature. For an ABO_3 perovskite, while the B-sites contribute to the (1/2 1/2 1/2) [$(1\ 0\ 1)_{or}$] reflection for both orthorhombic $Pbnm$ and monoclinic $P2_1/n$ symmetry, the (-1/2 1/2 1/2) [$(0\ -1\ 1)_{or}$] peak is allowed only for $P2_1/n$ symmetry. While the (-1/2 1/2 1/2) (Fig. 2(e)) is absent for orthorhombic $NdGaO_3$ substrate as expected, the presence of this particular peak for the film, establish that the 2ENO/1LNO SL is monoclinic at room temperature. Thus the individual layer, which has a larger ratio in the superlattice, determines the resultant symmetry of the heterostructures: monoclinic for 2ENO/1LNO (similar to bulk ENO) and rhombohedral like for 1ENO/2LNO (similar to bulk LNO). Ab-initio calculations have been

carried out for the superlattices also to investigate how the bond lengths and angles are affected by the heterostructuring and the extracted information is shown in Table I. While inequivalent Ni sites exists for both superlattices, the bond length variation between Ni(1) and Ni(2) is larger for 2ENO/1LNO SL (Jahn-Teller like distortion for Ni(2)). The average bond angles are smaller for 2ENO/1LNO SL due to the smaller ionic radii of Eu ion compared to La.

After confirming the structural quality and determining the symmetry, we have investigated the electronic properties of these SLs. The most important observation is 2ENO/1LNO remains metallic down to 240 K i.e. we have been able to a generate **a metallic phase with a monoclinic symmetry**, which has not been realized before. The strong thermal hysteresis behavior of the resistivity measured during the cooling and warming cycles indicates the first-order nature of the MIT. Hence, by our purposeful engineering of nickelates, we can rule out the *o*rthorhombic to monoclinic symmetry change at T_{MIT} is not a prerequisite for the electronic transition in rare earth nickelates. On the other hand, 1ENO/2LNO SL remains metallic down to 2K without any thermal hysteresis despite having two inequivalent Ni sites. This observation emphasizes that the in-plane orthorhombic distortion is crucial for the MIT, as shown by Lee *et al.*'s model hamiltonian calculation that the single particle gap depends on the orthorhombicity of the lattice[39].

The magnetic ordering for 2ENO/1LNO SL have also been investigated by using resonant X-ray diffraction at the Ni L_3 edge. The intensity of the Bragg reflection corresponding to the wave vector k = (1/4 1/4 1/4) for E' type antiferromagnetism has been recorded at different temperatures. The antiferromagnetic transition temperature (T_N) is found to be

Table 5.1: Ni-O-Ni angle and Ni-O bond lengths for 2ENO/1LNO (2E/1L) and 1ENO/2LNO (1E/2L) SLs from ab-initio theory.

		∠ Ni-O-Ni (°)		Ni-O (Å)	
		2E/1L	1E/2L	2E/1L	1E /2L
Ni(1)	average along c	161.4	160.0	1.940	1.928
	average in ab plane	162.0	165.0	1.955	1.949
	net average	161.8	163.3	1.950	1.942
Ni(2)	average along c	158.0	162.3	1.895	1.933
	average in ab plane	159.7	161.3	1.962	1.958
	net average	159.1	161.6	1.940	1.950

220 K by plotting the integrated intensity as a function of T (Fig. 2(b)). $d\rho/dT$ vs. T plot in Fig. 2(b) (right axis) further confirms T_N and T_{MIT} are not the same i.e. the superlattice has three phases: PM (for T > 240 K), PI (220K < T < 240 K) and AFI (T < 220 K).

The rare earth nickelates are a negative charge transfer system with ground state wave function $|\psi> = \alpha|d^7> + \beta|d^8\underline{L}>$ with α=0.4-0.5 and β=0.6-0.5 ($\underline{L}$ indicates hole on ligand oxygen p orbitals). As a result both the Ni d bands and O p bands cross the Fermi energy forming hole and electron pockets. Recent angle resolved photoemission spectroscopy measurements on metallic $LaNiO_3$ showed that unlike the electron Fermi surface, the hole Fermi surface has nesting character[165]. In order to determine how the electronic and mag-

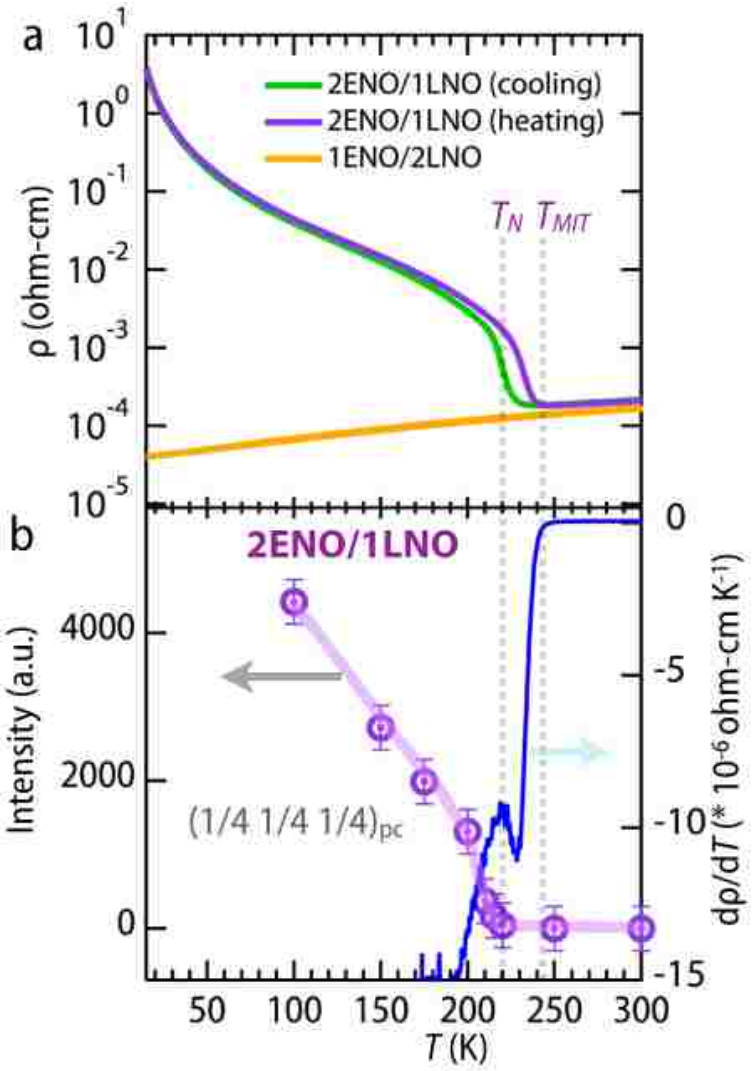

Figure 5.3: (a) and (b) Temperature dependence of the *dc* resistivity and Hall coefficients, respectively, in three SLs. (c) XAS data at 20 and 300 K.

netic transitions affect the carriers, Hall effect and X-ray absorption spectroscopy (XAS) measurements were carried out at various temperatures. As one can see in Fig. 4(a), R_H remains positive for the metallic 1ENO/2LNO, R_H become -ve below the magnetic transition while it is +ve in PI and PM phase. This was further confirmed by R_H measurements on 3ENO/1LNO SL, NNO on STO and DSO where the two transitions have a larger temperature difference. Similar observations were also found for $NdNiO_3$, $PrNiO_3$, $SmNiO_3$ while the thermopower measurement shows the Seebeck coefficient is $= -ve$ in all phases[17].

Assuming one hole and one electron band contributing to the Hall effect, R_H can be expressed as $R_H=(n_p\mu_p^2 - n_e\mu_e^2)/e(n_p\mu_p+n_e\mu_e)^2$ where n_p (n_e) is the hole (electron) density and $\mu_p(\mu_e)$ is mobility of hole (electron). Since the thermopower measurements confirm majority carriers are electron, positive R_H demands $\mu_p > \mu_e$. The ARPES measurement on LNO also show that the electrons have enhanced effective mass while holes do not have such enhancement[165]. Thus, the sign change of R_H without any sign change of Seebeck coefficient demands that the holes states are mainly responsible for the magnetic transition. The infrared optics measurement on NNO on STO shows the Drude peak vanishes only below T_N and the insulating phase in $T_N < T < T_{MIT}$ regions still show a Drude peak, which is generally a signature of a metallic state[141].

According to the above data, control of the m and n indices has a strong effect on the long-range transport properties of the SLs. To shed deeper light on the microscopic electronic structure, we performed detailed soft x-ray absorption measurements (see Fig. 2(c)) for all the samples both at 300 K (solid lines) and 20 K (dash lines) on the Ni L edge of the three superlattices, respectively. Note that the first peak at 850 eV of each curve marked in the blue column belongs to the La M_4 edge[4]. All samples show two strong white lines at 855 eV and 872 eV which correspond to the L_3 and L_2 edges of the d^7 configuration. Moreover, the shoulders around 853 eV and 871 eV can also be observed clearly at 20 K, being much more distinct in 2ENO/1LNO and 1ENO/1LNO than that in 1ENO/2LNO while at 300 K all the SLs show a much weaker multiplet structure. The size of the energy separation between the L_3 multiplet peak for each superlattice is plotted as the inset in Fig. 2(c). The splitting is about 1.4 eV, nearly the same for all three samples at 300 K. However at 20 K, the value of 2ENO/1LNO and 1ENO/1LNO is about 1.7 eV while it decreases slightly to 1.3 eV for 1ENO/2LNO. This splitting is related to the activation gap and was shown to correlate with the Ni-O-Ni bond angle[4]. These results indicate a buckling of this bond across the MIT, as seen in bulk[75, 142].

To conclude, mENO/nLNO SLs were grown on NGO substrates with n and m integers values ranging from 1 to 2. Electrical transport measurements revealed a sudden switchover from a strong first-order MIT to fully metallic behavior for n = 2, m = 1. Electronic structure measurements supported the transport results, showing a strong increase in the activation gap in the insulating state. Structural studies revealed a transition to a lower symmetry state coincided with the loss of metallic behavior.

5.3 Engineered Ni symmetry breaking

In the previous section, the two superlattices feature unbalanced m and n values of 2 and 1. An interesting observation which can be drawn from this structural motif comes from Fig. 5.1(a). In either case, the superlattice structure artificially creates two different Ni sites, one that will bond with the same A-site above and below, and one that will bond with one Eu and one La. While, as discussed in chapter 1, the bonding with the A-site is typically weak, the size difference between the A-sites will cause the respective Ni sites to be unique. Within the 1ENO/2LNO superlattice, as shown, the structure goes to rhombohedral symmetry and a metallic state is stabilized. However, the 2ENO/1LNO samples undergo a strong MIT as shown in Fig. 5.3. For the rare-earth nickelates, in the bulk, the MIT is *always* commensurate with a symmetry lowering to $P2_1/c$ (monoclinic) from $Pbnm$ (orthorhombic)[123, 139, 140]. However, in Chapter 4 we covered the case of an ultra thin film of NNO on NGO that showed a strong MIT with no symmetry lowering. In the case of 2ENO/1LNO, the creation of two inequivalent Ni sites by design suggests the system should take on monoclinic symmetry at all temperatures, as two inequivalent Ni sites lowers the symmetry to $P2_1/c$. Alternatively, 1ENO/1LNO superlattices feature equivalent Ni sites. Thus these two systems present an ideal case to study the effects of structural engineering to artificially break symmetry.

Soft x-ray resonant scattering experiments were done at the 4.0.2 beam line of the Advanced Light Source at Lawrence-Berkeley National Laboratory. Hard x-ray resonant scattering experiments were done at the 6-ID-B beam line of the Advanced Photon Source at Argonne National Laboratory.

Purely from transport, both of these SLs show strong, first-order MITs about 100K apart, despite the very different structural motifs (1ENO/1LNO MIT at 150K, not shown). Magnetically, as discussed in section 4.2, the nickelates anti-ferromagnetically order with E' (111) ordering with 4x4x4 magnetic unit cell, and such ordering has been found for all

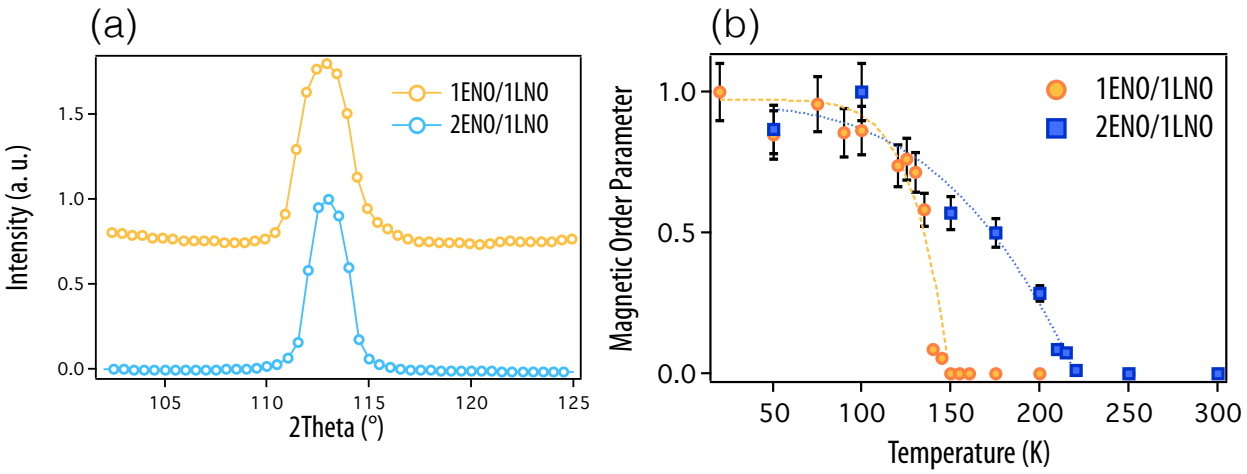

Figure 5.4: (a) and (b) Temperature dependence of the *dc* resistivity and Hall coefficients, respectively, in three SLs. (c) XAS data at 20 and 300 K.

nickelates, including thin films, in the insulating state (except for the special case of NNO on LAO)[12, 13, 14, 125, 145]. To ensure that the novel structural engineering utilized here does not inhibit the magnetic order parameter, soft x-ray scattering experiments were carried out at the Ni L-edge. At low temperature, a Bragg peak was observed for both samples at $\theta \sim 110°$ corresponding to the E'-type anti-ferromagnetism, Fig. 5.4(a). Temperature dependence of this peak for both samples shows a strong magnetic transition, commensurate with the MIT in 1ENO/1LNO and $\sim$ 20 K lower for 2ENO/1LNO, as discussed in section 5.2, Fig. 5.4(b). Thus, the designed symmetry breaking does not have a significant impact on the magnetic order parameter for either superlattice.

Following from our work on single layers, charge order and symmetry lowering are not necessary ingredients to the MIT. Within the structural motif, the artificial creation of two Ni sites is expected to lower the symmetry to monoclinic, even in the metallic state for 2ENO/1LNO. Meanwhile, there is no artificial Ni site symmetry breaking for the 1ENO/1LNO SL, with each Ni site having La and Eu A-sites as nearest (A-site) neighbors. Thus, hard x-ray resonant scattering at the Ni L edge at the (011) peak is expected to detect the monclinicity for 2ENO/1LNO above the transition, while for 1ENO/1LNO the lack of artificial symmetry breaking suggests no peak should appear. Below the transition, the appearance of charge order would cause a large change in the (011) peak, whether or not it appears above the transition.

For 2ENO/1LNO, Fig. 5.5(a), above the transition a strong Ni K-edge resonance does

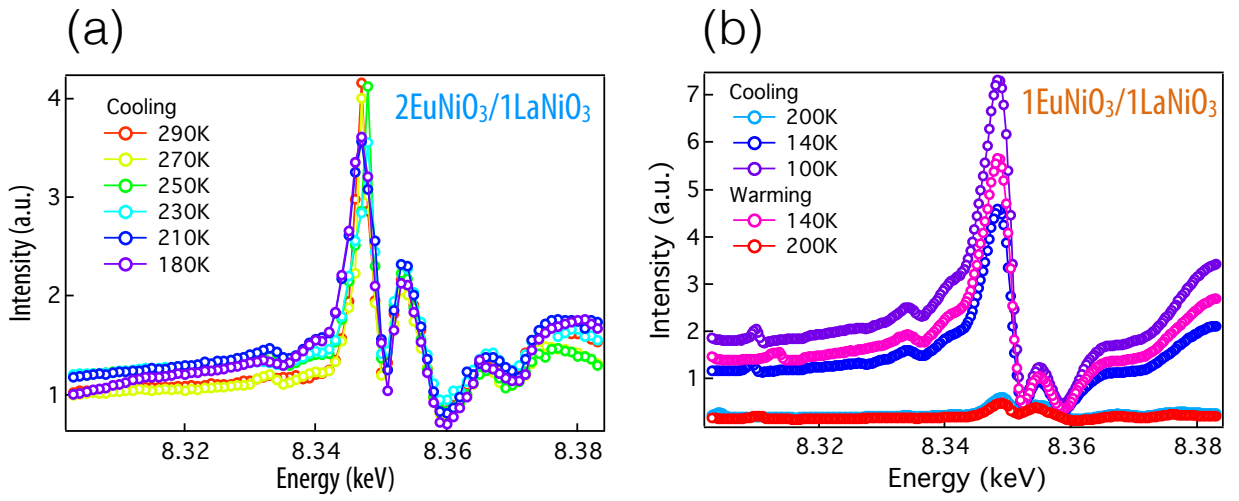

Figure 5.5: (a) and (b) Temperature dependence of the *dc* resistivity and Hall coefficients, respectively, in three SLs. (c) XAS data at 20 and 300 K.

indeed appear, indicating the presence of 2 Ni sites in a rock-salt pattern, as in bulk nickelates at low temperature. However, crossing the MIT does not change either the intensity or line shape of the doublet peak. This result is unique to this system among the nickelates, while NNO on NGO shows no change across the MIT as well, it also shows no peak at any temperature. For 1ENO/1LNO, a peak is observed above the MIT as well, showing some degree of monoclincity is present, however it is significantly weaker then that observed for 2ENO/1LNO, Fig. 5.5(b). As the temperature is lowered across the MIT, a sudden sharp increase in the peak intensity and a distinct line shape change is observed, bringing the total intensity above what is observed for 2ENO/1LNO. Interestingly, the line shape observed here is unique to this system, having not been observed for any other nickelates, FDMNES calculations are under way to ascertain the source of this anomaly which may indicate a strong enhancement of the distortion[17, 38].

Structurally, the lattice expansion observed in the bulk nickelates has also been observed in all ultra thin films studied thus far. This sudden change in lattice volume confirms the first order nature of the MIT in these materials[17, 38]. Identification of this expansion is done through temperature controlled observation of the (002) Bragg-peak position, which gives the out-of-plane lattice constant. The results of these experiments, along with the normalized magnetic and charge order parameters are shown in Fig. 1.6 (a) and (b) for the 1ENO/1LNO and 2ENO/1LNO SLs respectively. The charge order parameter was found

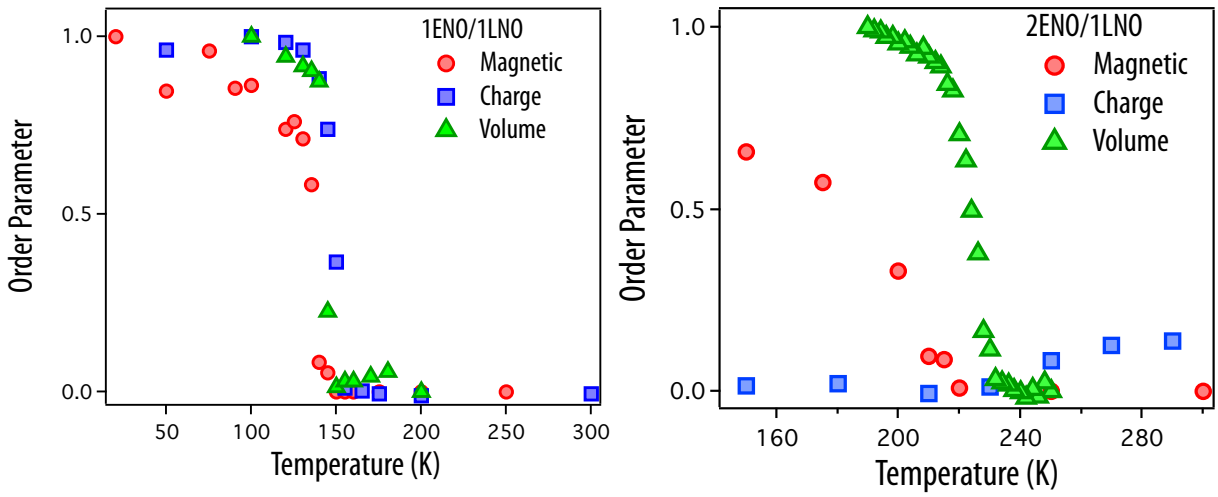

Figure 5.6: (a) and (b) Temperature dependence of the *dc* resistivity and Hall coefficients, respectively, in three SLs. (c) XAS data at 20 and 300 K.

by normalizing to the largest (011) peak intensity, for the 1ENO/1LNO sample at low temperature, and taking the peak above the transition as zero. The data was first normalized against the background intensity (at 8.32 keV), following the method utilized by Staub *et al* for thick films[139].The magnetic order parameters were normalized to one for each SL separately at low temperature, zero corresponds to no signal above background noise. In the case of the 1ENO/1LNO superlattice, a clear transition commensurate with the MIT occurs for all three order parameters, all three saturating close to the MIT. For 2ENO/1LNO, however, the order parameters all show different behavior. While the volume expansion occurs at the same temperature as the MIT, the magnetic transition occurs around 20 K lower, as discussed in section 5.2. However, unlike the 1ENO/1LNO SL, which saturates within 50 K of the transition, the magnetic order parameter is reduced and does not saturate down to 50 K, around 200 K below the transition. These two unusual magnetic properties, the small gap between the transition and the non-saturation of the magnetism, points to this sample lying very near the triple point on the bulk phase diagram, Fig. 1.8, perhaps leading to some magnetic phase inhomogeneity at higher temperatures. Further measurements will be required to understand the incomplete nature of the magnetic transition for this sample.

Finally, the CO parameter for the 2ENO/1LNO sample is intriguing. The peak being larger then the high temperature data for 1ENO/1LNO, its peak intensity is significant

and must be considered. Due to the metallic nature of the film above the transition, it is highly unlikely that any CO is present in this state, as the partially filled Ni *d*-band lies at the Fermi-surface. Resonant scattering is also sensitive to aspherical tensor scattering, which originates from non-diagonal terms in the scattering matrix, as discussed in section 2.2. This situation can thus arise when there is any distortion of the NiO_6 octahedra, such as an activated JT mode. As previously discussed, the Ni^{3+} ion is expected to be a JT ion, however CO breaks the degeneracy in the rare-earth nickelates, allowing the octahedra to remain unperturbed. It appears that artificial breaking of the Ni site symmetry, in a pattern that is not concurrent with the rock-salt CO pattern, raises the energy of this CO ground state and pushes the system towards another degeneracy lifting scheme, here likely a JT distortion. Further measurements, such as orbital reflectometry and extended x-ray absorption fine structure, could shed light on this matter.

Thus, the combination of hard and soft x-ray scattering experiments reveal the artificial symmetry breaking in the 2ENO/1LNO SL removes the bulk-like charge order transition while preserving the bulk-like magnetic order and MIT. In contrast, the 1ENO/1LNO SL preserves all of the bulk order parameters, though it displays a monoclinic distortion above the transition disparate to the bulk-like *Pbnm* metallic state. It is postulated that the rock-salt CO pattern is unstable due to the three-fold Ni repeat pattern in the growth direction for 2ENO/1LNO, while for 1ENO/1LNO the Ni sites repeat in a two-fold matter compatible with rock-salt ordering. Further investigation to evidence this hypothesis are under way, and theoretical modeling is being sought. It should be noted, charge ordering can occur in many patterns, however the superlattice peaks created by such patterns extend across reciprocal space, and the infeasibility of using x-rays to map the entirety of this space precludes this investigation using currently available techniques.

5.4 Conclusion

To conclude, the use of digital heterostructure of rare-earth nickelates $EuNiO_3$ and $LaNiO_3$ was shown to be powerful tool for engineering both controlled MIT temperatures and to destabilize a bulk-like order parameter, while maintaining the bulk-like MIT. These findings are likely not restricted to these specific SLs, with the possibility to utilize other complex oxides in this form to tune transition temperatures, and more interestingly, using artificially broken symmetry to selectively modulate order parameters.

6 Summary and future work

6.1 Conclusion

To begin, we established three different methods for manipulating the ground states of complex oxides: i) isostructural and isoelectronic doping, ii) epitaxial constraint, and iii) superlattice heterostructuring. Ground state alteration by these three techniques was investigated with various techniques, with synchrotron-based x-ray absorption spectroscopy and resonant scattering being the chief methods utilized.

In the case of isostructural and isoelectronic doping, featuring bulk samples, it was found that going from 3-4-5d orbitals strongly influences the amount of hole doping on the O p-band, which in turn was found to be extremely effective method for controlling the valence of the Cu d-band, allowing the Zhang-Rice state to be tuned. Further investigation revealed this same doping leads to a localization of the Cu d-band in $CaCu_3Ir_4O_{12}$, leading to the formation of a Kondo lattice of magnetic Cu^2+ ions interacting with the itinerant Ir^{4+} electrons leading a competition between the magnetic RKKY coupling and Kondo effects with the correct mixture to induce heavy fermion effects, a very rare ground state in non-4f materials.

Utilizing the Laboratory for Artificial Quantum Materials in-house pulsed laser deposition capabilities, epitaxial constraint was applied to the first ultra thin films of $EuNiO_3$ available. Upon discovering the growth conditions which allow the stabilization of this material, and our group's previous work on $LaNiO_3$ and $NdNiO_3$, it became clear the ideal growth temperature is heavily dependent on the cohesive energy of the lattice, with the less strongly bound materials requiring lower temperatures to avoid phase decomposition. Application of different levels of compressive and tensile strain was able to modify the onset temperature for the metal-insulator (MIT) transition, as in the other nickelates, quite drastically, as the ultra thin films were able to quench the transition entirely, high compressive strain, to around room temperature, SLAO substrate, to above 380K for tensile strain (with the bulk transition being 470K). Interestingly, the ultra-thin structure also has a strong influence on the symmetry transition within these materials. For films of $NdNiO_3$ on $NdGaO_3$ it was found that the bulk-like symmetry transition is entirely suppressed despite the first-order MIT observed in the samples, giving an extremely rare, purely electronic Mott transition. This

was the first realization of a nickelate, in any form, showing a strong MIT with no accompanying symmetry lowering. However, for $EuNiO_3$ films on $NdGaO_3$ of the same thickness, the monoclinic phase is realized, possibly due to the higher distortion of the ideal ABO_3 structure with the smaller rare-earth *A*-site. Thus, while the effects of epitaxial constraint have been extensively studied for many materials, small differences in materials can cause profound differences in their ground states under strain.

Finally, extending thin film growth capabilities to superlattice heterostructures requires materials requiring compatible growth conditions, around 3% or less difference in lattice constant, and layer-by-layer precision, making this method one of the most difficult, but also one of the most intriguing, emerging methods of complex oxide ground state engineering. By applying this method to digital alloys of $EuNiO_3$ and $LaNiO_3$, all three conditions were met, with samples showing high quality and layer-by-layer control. The relative number of layers of each material in each repeat of the superlattice determines T_{MIT} allowing effective tuning from low temperature to near room. Most importantly, the superlattice structure can be used to artificially break the bulk symmetry of the constituent materials, which was found to have a profound effect on the structural and electronic phase transitions. Despite this, the first-order MIT nor E′-type antiferromagnetic ordering does not show any divergence from bulk-like behavior. Coupled with our results on ultra-thin films, these findings cast serious doubt upon the conclusions drawn from bulk nickelates that linked the MIT directly to the symmetry (or charge ordering) transition. Beyond nickelates, only the gas-liquid transition lacks a symmetry transition except in rare special cases, such as presented within this thesis. Combined with these special cases, our results present strong evidence that symmetry changes, while typically commensurate with phase transitions, should not be assumed to be the driving force behind such transitions and all the accompanying orderings must be considered carefully.

When taken as a whole these works provide insight into the phase space malleability within transition metal oxides. While more conventional means of engineering their behavior, such as chemical doping, externally applied fields, isotropic pressure, and etc, can harbor myriad of interesting behavior themselves, the emerging methods utilized in this thesis clearly have a significant place in the future of this vast field of research and have already lead to the realization of hitherto unknown ground states.

6.2 Future prospects

While this work has shed further light on the effects and utility of these techniques for ground state engineering, much research remains to be done in all of the three presented methods. The AOPs, specifically, are still, relatively, in their infancy and thin film deposition has been very limited thus far, likely due to the lack of substrates which would properly seed the *A*-site ordered phase. One possible solution to this issue, which is possibly already being attempted, is the use of molecular beam epitaxy, which is able to grow a single atomic layer, instead of a unit cell, of material at a time, coupled with the use of substrates with along specific directions which would generate terraces containing only a small integer number of AOP unit cells. Our work on the bulk material has provided insight into how the electronic structure of these materials reconstructs, providing a template for future studies on these materials.

For thin films and heterostructures, our findings raise significant questions about the true nature of phase transitions in complex oxides, and the application of the present methods to any of the numerous materials being studied could help to disentangle the true progenitor of their unique phase transitions. Looking to our own work, further investigation is needed to truly understand the structural changes in the $m\mathrm{EuNiO_3}/n\mathrm{LaNiO_3}$ superlattices, as we were only able to investigate the bulk-like symmetry transition ordering peak due to the impracticality to effectively map large portions of reciprocal space with x-ray scattering. While the bulk-like transition is indeed removed for the $2\mathrm{EuNiO_3}/1\mathrm{LaNiO_3}$ sample, other charge ordering patterns, possibly some type of strip ordering phase cannot be ruled out.

Bibliography

[1] P. Cox, *Transition metal oxides*. Clarendon Press, Oxford, 1992.

[2] D. I. Khomskii, *Transition Metal Compounds*. Cambridge University Press, 2014.

[3] J. Zaanen, G. A. Sawatzky, and J. W. Allen, "Band gaps and electronic structure of transition-metal compounds," *Phys. Rev. Lett.*, vol. 55, pp. 418–421, 1985.

[4] D. Meyers, S. Middey, M. Kareev, M. van Veenendaal, E. J. Moon, B. A. Gray, J. Liu, J. W. Freeland, and J. Chakhalian, "Strain-modulated Mott transition in $EuNiO_3$ ultrathin films," *Phys. Rev. B*, vol. 88, p. 075116, 2013.

[5] J. B. Torrance, P. Lacorre, A. I. Nazzal, E. J. Ansaldo, and C. Niedermayer, "Systematic study of insulator-metal transitions in perovskites $R\ NiO_3$ (R = Pr, Nd, Sm, Eu) due to closing of charge-transfer gap," *Phys. Rev. B*, vol. 45, pp. 8209–8212, 1992.

[6] J. G. Bednorz, K. A. Muller, "Possible high T_c superconductivity in the BaLaCuO system," *Physica B*, vol. 64, 1986.

[7] H. Ihara *et al*, "A new high-$T_c TlBa_2Ca_3Cu_4O_{11}$ superconductor with $T_c > 120K$," *Nature*, vol. 334, pp. 510 – 511, 1988.

[8] C. W. Chu *et al*, "Superconductivity above 150K in $HgBa_2Ca_2Cu_3O_{8+\delta}$ at high pressures," *Nature*, vol. 365, pp. 323 – 325, 1993.

[9] Zhi-An Ren *et al*, "Superconductivity and phase diagram in iron-based arsenic-oxides $ReFeAsO_{1-\delta}$ (Re = rare-earth metal) without fluorine doping," *Europhysics Letters*, vol. 83, 1993.

[10] D. Meyers *et al*, "Zhang-Rice physics and anomalous copper states in A-site ordered perovskites," *Scientific Reports*, vol. 3, no. 1834, 1993.

[11] D. Meyers, S. Middey, J.-G. Cheng, S. Mukherjee, B. Gray, Y. Cao, J.-S. Zhou, J. Goodenough, Y. Choi, D. Haskel *et al.*, "Competition between heavy-fermion and Kondo interaction in isoelectronic A-site ordered perovskites," *Nature Communications*, vol. 5, no. 5818, 2014.

[12] J. Liu, M. Kargarian, M. Kareev, B. Gray, P. J. Ryan, A. Cruz, N. Tahir, Y.-D. Chuang, J. Guo, J. M. Rondinelli *et al.*, "Heterointerface engineered electronic and magnetic phases of $NdNiO_3$ thin films," *Nature Communications*, vol. 4, 2013.

[13] V. Scagnoli, U. Staub, A. M. Mulders, M. Janousch, G. I. Meijer, G. Hammerl, J. M. Tonnerre, and N. Stojic, "Role of magnetic and orbital ordering at the metal-insulator transition in $NdNiO_3$," *Phys. Rev. B*, vol. 73, p. 100409, 2006.

[14] V. Scagnoli, U. Staub, Y. Bodenthin, M. García-Fernández, A. M. Mulders, G. I. Meijer, and G. Hammerl, "Induced noncollinear magnetic order of Nd^{3+} in $NdNiO_3$ observed by resonant soft x-ray diffraction," *Phys. Rev. B*, vol. 77, p. 115138, 2008.

[15] D. I. Khomskii, *Basic aspects of the quantum theory of solids: order and elementary excitations*. Cambridge University Press, 2010.

[16] S. von Molnár and P. Stampe, *Handbook of Magnetism and Advanced Magnetic Materials-Spintronics and Magnetoelectronics*. John Wiley & Sons, Ltd, 2007, vol. 5.

[17] M. L. Medarde, "Structural, magnetic and electronic properties of $RNiO_3$ perovskites (R = rare earth)," *Journal of Physics: Condensed Matter*, vol. 9, no. 8, p. 1679, 1997.

[18] C. Schinzer, "Distortion of perovskites," 1998. [Online]. Available: http://www.ccp14.ac.uk/ccp/web-mirrors/pki/uni/pki/members/schinzer/stru_chem/perov/dist.html

[19] V. Goldschmidt, "Die Gesetze der Krystallochemie," *Naturwissenschaften*, vol. 14, no. 21, pp. 477–485, 1926.

[20] H. A. Jahn and E. Teller, "Stability of polyatomic molecules in degenerate electronic states. I. Orbital degeneracy," in *Proceedings of the Royal Society of London A: Mathematical, Physical and Engineering Sciences*, vol. 161, no. 905. The Royal Society, 1937, pp. 220–235.

[21] N. W. Ashcroft and N. D. Mermin, *Solid State Physics*. Holt, Rinehart and Winston, New York, 1976, 2005.

[22] A. Deschanvres, B. Raveau, and F. Tollemer, "Substitution of copper for a divalent metal in perovskite-type titanates," *Bull. Soc. Chim. Fr*, vol. 11, pp. 4077–4078, 1967.

[23] M. Subramanian, D. Li, N. Duan, B. Reisner, and A. Sleight, "High Dielectric Constant in $\{ACu_3Ti_4O_{12}\}$ and $\{ACu_3Ti_3FeO_{12}\}$ Phases," *Journal of Solid State Chemistry*, vol. 151, no. 2, pp. 323 – 325, 2000.

[24] Y. Shimakawa and T. Saito, "A-site magnetism in A-site-ordered perovskite-structure oxides," *Physica Status Solidi (B)*, vol. 249, no. 3, pp. 423–434, 2012.

[25] T. Mizokawa, Y. Morita, T. Sudayama, K. Takubo, I. Yamada, M. Azuma, M. Takano, and Y. Shimakawa, "Metallic versus insulating behavior in the A-site ordered perovskite oxides $ACu_3Co_4O_{12}$ (A= Ca and Y) controlled by Mott and Zhang-Rice physics," *Physical Review B*, vol. 80, no. 12, p. 125105, 2009.

[26] Y. Shimakawa, "A-Site-Ordered Perovskites with Intriguing Physical Properties," *Inorganic Chemistry*, vol. 47, no. 19, pp. 8562–8570, 2008.

[27] S. Jin, T. H. Tiefel, M. McCormack, R. A. Fastnacht, R. Ramesh, and L. H. Chen, "Thousandfold Change in Resistivity in Magnetoresistive La-Ca-Mn-O Films," *Science*, vol. 264, no. 5157, pp. 413–415, 1994.

[28] H. Li, X. Liu, C. Li, S. Lv, Y. Bai, Z. Wang, and J. Meng, "Magnetic coupling mechanism in A-site ordered perovskite $YMn_3Al_4O_{12}$: Extended (Mn-O)-(O-Mn) superexchange," *Solid State Sciences*, vol. 17, no. 0, pp. 63 – 66, 2013.

[29] Mizokawa, Takashi and Morita, Yosuke and Sudayama, Takaaki and Takubo, Kou and Yamada, Ikuya and Azuma, Masaki and Takano, Mikio and Shimakawa, Yuichi, "Metallic versus insulating behavior in the A-site ordered perovskite oxides $ACu_3Co_4O_{12}$ (A= Ca and Y) controlled by Mott and Zhang-Rice physics," *Physical Review B*, vol. 80, no. 12, p. 125105, 2009.

[30] Zhang, FC and Rice, TM, "Effective Hamiltonian for the superconducting Cu oxides," *Physical Review B*, vol. 37, no. 7, p. 3759, 1988.

[31] J.-G. Cheng, J.-S. Zhou, Y.-F. Yang, H. Zhou, K. Matsubayashi, Y. Uwatoko, A. MacDonald, and J. Goodenough, "Possible Kondo Physics near a Metal-Insulator Crossover in the A-Site Ordered Perovskite $CaCu_3Ir_4O_{12}$," *Physical Review Letters*, vol. 111, no. 17, p. 176403, 2013.

[32] G. Demazeau, A. Marbeuf, M. Pouchard, and P. Hagenmuller, "Sur une srie de composs oxygnes du nickel trivalent derivs de la perovskite ," *Journal of Solid State Chemistry*, vol. 3, no. 4, pp. 582 – 589, 1971.

[33] P. Lacorre, J. Torrance, J. Pannetier, A. Nazzal, P. Wang, and T. Huang, "Synthesis, crystal structure, and properties of metallic $PrNiO_3$: Comparison with metallic $NdNiO_3$ and semiconducting $SmNiO_3$," *Journal of Solid State Chemistry*, vol. 91, no. 2, pp. 225 – 237, 1991.

[34] J. c. v. Chaloupka and G. Khaliullin, "Orbital Order and Possible Superconductivity in $LaNiO_3/LaMO_3$ Superlattices," *Phys. Rev. Lett.*, vol. 100, p. 016404, 2008.

[35] A. R. Kaul, O. Y. Gorbenko, and A. A. Kamenev, "The role of heteroepitaxy in the development of new thin-film oxide-based functional materials," *Russian Chemical Reviews*, vol. 73, no. 9, p. 861, 2004.

[36] J.-S. Zhou and J. B. Goodenough, "Chemical bonding and electronic structure of $R\mathrm{NiO}_3$ (R = rare earth)," *Phys. Rev. B*, vol. 69, p. 153105, 2004.

[37] J. L. García-Muñoz, J. Rodríguez-Carvajal, P. Lacorre, and J. B. Torrance, "Neutron-diffraction study of R NiO_3 (R =La,Pr,Nd,Sm): Electronically induced structural changes across the metal-insulator transition," *Phys. Rev. B*, vol. 46, pp. 4414–4425, 1992.

[38] G. Catalan, "Progress in perovskite nickelate research," *Phase Transitions*, vol. 81, no. 7-8, pp. 729–749, 2008.

[39] S. Lee, R. Chen, and L. Balents, "Landau Theory of Charge and Spin Ordering in the Nickelates," *Phys. Rev. Lett.*, vol. 106, p. 016405, 2011.

[40] ——, "Metal-insulator transition in a two-band model for the perovskite nickelates," *Phys. Rev. B*, vol. 84, p. 165119, 2011.

[41] J. L. Garca-Muoz, J. Rodrguez-Carvajal, and P. Lacorre, "Sudden Appearance of an Unusual Spin Density Wave At the Metal-Insulator Transition in the Perovskites $RNiO_3$ (R=Pr, Nd)," *EPL (Europhysics Letters)*, vol. 20, no. 3, p. 241, 1992.

[42] M. Imada, A. Fujimori, and Y. Tokura, "Metal-insulator transitions," *Reviews of Modern Physics*, vol. 70, no. 4, p. 1039, 1998.

[43] R Lengsdorf and A Barla and J A Alonso and M J Martinez-Lope and H Micklitz and M M Abd-Elmeguid, "The observation of the insulator-metal transition in $EuNiO_3$ under high pressure," *Journal of Physics: Condensed Matter*, vol. 16, no. 20, p. 3355, 2004.

[44] J.-G. Cheng, J.-S. Zhou, J. B. Goodenough, J. A. Alonso, and M. J. Martinez-Lope, "Pressure dependence of metal-insulator transition in perovskites $RNiO_3$ (R = Eu, Y, Lu)," *Phys. Rev. B*, vol. 82, p. 085107, 2010.

[45] Liu, Jian and Kareev, M. and Gray, B. and Kim, J. W. and Ryan, P. and Dabrowski, B. and Freeland, J. W. and Chakhalian, J., "Strain-mediated metal-insulator transition in epitaxial ultrathin films of $NdNiO_3$," *Applied Physics Letters*, vol. 96, no. 23, 2010.

[46] A. Tiwari, C. Jin, and J. Narayan, "Strain-induced tuning of metal-insulator transition in $NdNiO_3$," *Applied Physics Letters*, vol. 80, no. 21, pp. 4039–4041, 2002.

[47] A. Venimadhav, I. C. Lekshmi, and M. Hegde, "Strain-induced metallic behavior in $PrNiO_3$ epitaxial thin films ," *Materials Research Bulletin*, vol. 37, no. 2, pp. 201 – 208, 2002.

[48] F. Conchon, A. Boulle, R. Guinebretire, C. Girardot, S. Pignard, J. Kreisel, F. Weiss, E. Dooryhe, and J.-L. Hodeau, "Effect of tensile and compressive strains on the transport properties of $SmNiO_3$ layers epitaxially grown on (001) $SrTiO_3$ and $LaAlO_3$ substrates," *Applied Physics Letters*, vol. 91, no. 19, 2007.

[49] G. H. Aydogdu, S. D. Ha, B. Viswanath, and S. Ramanathan, "Epitaxy, strain, and composition effects on metal-insulator transition characteristics of $SmNiO_3$ thin films," *Journal of Applied Physics*, vol. 109, no. 12, 2011.

[50] E. J. Moon, D. J. Keavney, and S. J. May, "Strain Effects in Narrow-Bandwidth Manganites: The Case of Epitaxial $Eu_{0.7}Sr_{0.3}MnO_3$ Thin Films," *Phys. Rev. Applied*, vol. 1, p. 054006, 2014.

[51] J. H. Gruenewald, J. Nichols, J. Terzic, G. Cao, J. W. Brill, and S. S. A. Seo, "Compressive strain-induced metal–insulator transition in orthorhombic $SrIrO_3$ thin films," *Journal of Materials Research*, vol. 29, no. 21, pp. 2491–2496, 2014.

[52] J. Chakhalian, J. M. Rondinelli, J. Liu, B. A. Gray, M. Kareev, E. J. Moon, N. Prasai, J. L. Cohn, M. Varela, I. C. Tung, M. J. Bedzyk, S. G. Altendorf, F. Strigari, B. Dabrowski, L. H. Tjeng, P. J. Ryan, and J. W. Freeland, "Asymmetric Orbital-Lattice Interactions in Ultrathin Correlated Oxide Films," *Phys. Rev. Lett.*, vol. 107, p. 116805, 2011.

[53] D. Proffit, H. Jang, S. Lee, C. Nelson, X. Pan, M. Rzchowski, and C. Eom, "Influence of symmetry mismatch on heteroepitaxial growth of perovskite thin films," *Applied Physics Letters*, vol. 93, no. 11, pp. 111 912–111 912, 2008.

[54] S. Middey, P. Rivero, D. Meyers, M. Kareev, X. Liu, Y. Cao, J. Freeland, S. Barraza-Lopez, and J. Chakhalian, "Polarity compensation in ultra-thin films of complex oxides: The case of a perovskite nickelate," *Scientific Reports*, vol. 4, 2014.

[55] J. Liu, M. Kareev, D. Meyers, B. Gray, P. Ryan, J. Freeland, and J. Chakhalian, "Metal-Insulator Transition and Orbital Reconstruction in Mott-Type Quantum Wells Made of $NdNiO_3$," *Physical Review Letters*, vol. 109, no. 10, p. 107402, 2012.

[56] J. Chakhalian, J. W. Freeland, A. J. Millis, C. Panagopoulos, and J. M. Rondinelli, "*Colloquium* : Emergent properties in plane view: Strong correlations at oxide interfaces," *Rev. Mod. Phys.*, vol. 86, pp. 1189–1202, 2014.

[57] A. Rüegg and G. A. Fiete, "Topological insulators from complex orbital order in transition-metal oxides heterostructures," *Phys. Rev. B*, vol. 84, p. 201103, 2011.

[58] A. Tiwari, K. Rajeev, and J. Narayan, "Low temperature electrical transport in $La_{1-x}Nd_xNiO_{3-\delta}$," *Solid state communications*, vol. 121, no. 6, pp. 357–361, 2002.

[59] K. Okazaki, "Photoemission Studies of Temperature-Induced Metal-Insulator Transitions in Transition-Metal Oxides," Ph.D. dissertation, University of Tokyo, 2002.

[60] R. Sánchez, M. Causa, A. Seoane, J. Rivas, F. Rivadulla, M. López-Quintela, J. P. Cacho, J. Blasco, and J. Garcıa, "Metal-Insulator Transition and Magnetic Properties of $La_{1-x}Eu_xNiO_3$ ($0 < x < 1$)," *Journal of Solid State Chemistry*, vol. 151, no. 1, pp. 1–11, 2000.

[61] J. J. Sakurai, *Advanced quantum mechanics*. Pearson Education India, 2006.

[62] M. W. Haverkort, "Spin and orbital degrees of freedom in transition metal oxides and oxide thin films studied by soft x-ray absorption spectroscopy," *arXiv preprint cond-mat/0505214*, 2005.

[63] J. Fink, E. Schierle, E. Weschke, and J. Geck, "Resonant elastic soft x-ray scattering," *Reports on Progress in Physics*, vol. 76, no. 5, p. 056502, 2013.

[64] J.-L. Hodeau, V. Favre-Nicolin, S. Bos, H. Renevier, E. Lorenzo, and J.-F. Berar, "Resonant diffraction," *Chemical reviews*, vol. 101, no. 6, pp. 1843–1868, 2001.

[65] M. M. Woolfson, *An introduction to X-ray crystallography.* Cambridge University Press, 1997.

[66] H. Wang, L. Shi, B. Lukyanchuk, C. Sheppard, and C. T. Chong, "Creation of a needle of longitudinally polarized light in vacuum using binary optics," *Nature Photonics*, vol. 2, no. 8, pp. 501–505, 2008.

[67] J. Connerade, "Synchrotron Radiation. Techniques and Applications," *Journal of Modern Optics*, vol. 27, no. 4, pp. 443–444, 1980.

[68] K. S. Harsha, *Principles of vapor deposition of thin films.* Elsevier, 2005.

[69] W. Hong, H. N. Lee, M. Yoon, H. M. Christen, D. H. Lowndes, Z. Suo, and Z. Zhang, "Persistent step-flow growth of strained films on vicinal substrates," *Physical review letters*, vol. 95, no. 9, p. 095501, 2005.

[70] M. Kareev, S. Prosandeev, B. Gray, J. Liu, P. Ryan, A. Kareev, E. Ju Moon, and J. Chakhalian, "Sub-monolayer nucleation and growth of complex oxides at high supersaturation and rapid flux modulation," *Journal of Applied Physics*, vol. 109, no. 11, 2011.

[71] J. G. Amar, F. Family, and P.-M. Lam, "Dynamic scaling of the island-size distribution and percolation in a model of submonolayer molecular-beam epitaxy," *Phys. Rev. B*, vol. 50, pp. 8781–8797, 1994.

[72] J. Arthur and J. LePore, "GaAs, GaP, and $GaAs_xP_{1-X}$ epitaxial films grown by molecular beam deposition," *J. Vac. Sci. Technol*, vol. 6, pp. 545–548, 1969.

[73] J. Harris, B. A. Joyce, and P. Dobson, "Oscillations in the surface structure of Sn-doped GaAs during growth by {MBE}," *Surface Science*, vol. 103, no. 1, pp. L90 – L96, 1981.

[74] D. Meyers, E. J. Moon, M. Kareev, I. C. Tung, B. A. Gray, J. Liu, M. J. Bedzyk, J. W. Freeland, and J. Chakhalian, "Epitaxial stabilization of ultra-thin films of $EuNiO_3$," *Journal of Physics D: Applied Physics*, vol. 46, no. 38, p. 385303, 2013.

[75] J. A. Alonso, M. J. Martnez-Lope, M. T. Casais, M. A. G. Aranda, and M. T. Fernndez-Daz, "Metal-Insulator Transitions, Structural and Microstructural Evolution of $RNiO_3$ (R = Sm, Eu, Gd, Dy, Ho, Y) Perovskites: Evidence for Room-Temperature Charge Disproportionation in Monoclinic $HoNiO_3$ and $YNiO_3$," *Journal of the American Chemical Society*, vol. 121, no. 20, pp. 4754–4762, 1999.

[76] P. Lane, M. Crosbie, P. Wright, P. Donohue, P. Hirst, C. Reeves, C. Anthony, J. Jones, M. Todd, and D. Williams, "The Metal-Organic Chemical Vapor Deposition of Lanthanum Nickelate Electrodes for Use in Ferroelectric Devices," *Chemical Vapor Deposition*, vol. 9, no. 2, pp. 87–92, 2003.

[77] K. Bilewska, E. Wolna, M. Edely, P. Ruello, and J. Szade, "Evidence of charge disproportionation on the nickel sublattice in eunio$_3$ thin films: X-ray photoemission studies," *Phys. Rev. B*, vol. 82, p. 165105, 2010.

[78] D. H. Blank, G. Koster, G. A. Rijnders, E. van Setten, P. Slycke, and H. Rogalla, "Epitaxial growth of oxides with pulsed laser interval deposition," *Journal of Crystal Growth*, vol. 211, no. 14, pp. 98 – 105, 2000.

[79] D. L. Proffit, H. W. Jang, S. Lee, C. T. Nelson, X. Q. Pan, M. S. Rzchowski, and C. B. Eom, "Influence of symmetry mismatch on heteroepitaxial growth of perovskite thin films," *Applied Physics Letters*, vol. 93, no. 11, 2008.

[80] J.-S. Kang, S. S. Lee, G. Kim, H. J. Lee, H. K. Song, Y. J. Shin, S. W. Han, C. Hwang, M. C. Jung, H. J. Shin, B. H. Kim, S. K. Kwon, and B. I. Min, "Valence and spin states in delafossite $AgNiO_2$ and the frustrated Jahn-Teller system $ANiO_2$ ($A = \mathrm{Li}, \mathrm{Na}$)," *Phys. Rev. B*, vol. 76, p. 195122, 2007.

[81] D. Meyers, E. Moon, M. Kareev, I. Tung, B. Gray, J. Liu, M. Bedzyk, J. Freeland, and J. Chakhalian, "Epitaxial stabilization of ultrathin films of rare-earth nickelates," *arXiv preprint arXiv:1112.5348*, 2011.

[82] S. Little and A. Zangwill, "Equilibrium microstructure of epitaxial thin films," *Phys. Rev. B*, vol. 49, pp. 16 659–16 669, 1994.

[83] L. Glasser and H. D. B. Jenkins, "Lattice Energies and Unit Cell Volumes of Complex Ionic Solids," *Journal of the American Chemical Society*, vol. 122, no. 4, pp. 632–638, 2000.

[84] C. Li, K. C. K. Soh, and P. Wu, "Formability of {ABO_3} perovskites," *Journal of Alloys and Compounds*, vol. 372, no. 12, pp. 40 – 48, 2004.

[85] S. I. Shah, G. H. Jaffari, E. Yassitepe, and B. Ali, "Chapter 4 - Evaporation: Processes, Bulk Microstructures, and Mechanical Properties," in *Handbook of Deposition Technologies for Films and Coatings*, third edition ed., P. M. Martin, Ed. Boston: William Andrew Publishing, 2010, pp. 135 – 252.

[86] D. J. Scalapino, "A common thread: The pairing interaction for unconventional superconductors," *Rev. Mod. Phys.*, vol. 84, pp. 1383–1417, 2012.

[87] S. Tanaka, "High-temperature superconductivity: History and outlook," *JSAP International*, vol. 4, no. 4, pp. 17–22, 2001.

[88] Y. Xin, H. Zhou, J. Cheng, J. Zhou, and J. Goodenough, "Study of atomic structure and electronic structure of an $AA_3B_4O_{12}$ double-perovskite $CaCu_3Ir_4O_{12}$ using {STEM} imaging and {EELS} techniques," *Ultramicroscopy*, vol. 127, no. 0, pp. 94 – 99, 2013.

[89] J. Chakhalian, J. Freeland, H.-U. Habermeier, G. Cristiani, G. Khaliullin, M. Van Veenendaal, and B. Keimer, "Orbital reconstruction and covalent bonding at an oxide interface," *Science*, vol. 318, no. 5853, pp. 1114–1117, 2007.

[90] J. Chakhalian, J. Freeland, G. Srajer, J. Strempfer, G. Khaliullin, J. C. Cezar, T. Charlton, R. Dalgliesh, C. Bernhard, and G. Cristiani, "Magnetism at the interface between ferromagnetic and superconducting oxides," *Nature Physics*, vol. 2, no. 4, pp. 244–248, 2006.

[91] Z Hu and G Kaindl and S.A Warda and D Reinen and F.M.F de Groot and B.G Mller, "On the electronic structure of Cu(III) and Ni(III) in $La_2Li_{1/2}Cu_{1/2}O_4$, $Nd_2Li_{1/2}Ni_{1/2}O_4$, and Cs_2KCuF_6," *Chemical Physics*, vol. 232, no. 12, pp. 63 – 74, 1998.

[92] R. Sarangi, N. Aboelella, K. Fujisawa, W. B. Tolman, B. Hedman, K. O. Hodgson, and E. I. Solomon, "X-ray absorption edge spectroscopy and computational studies on $LCuO_2$ species: superoxide-CuII versus peroxide-CuIII bonding," *Journal of the American Chemical Society*, vol. 128, no. 25, pp. 8286–8296, 2006.

[93] A. Achkar, T. Regier, H. Wadati, Y.-J. Kim, H. Zhang, and D. Hawthorn, "Bulk sensitive x-ray absorption spectroscopy free of self-absorption effects," *Physical Review B*, vol. 83, no. 8, p. 081106, 2011.

[94] C. Chen, F. Sette, Y. Ma, M. Hybertsen, E. Stechel, W. Foulkes, M. Schulter, S. Cheong, A. Cooper, L. Rupp Jr *et al.*, "Electronic states in $La_{2-x}Sr_xCuO_{4+\delta}$ probed by soft-x-ray absorption," *Physical Review Letters*, vol. 66, no. 1, p. 104, 1991.

[95] N. Nücker, J. Fink, J. Fuggle, P. Durham, and W. Temmerman, "Evidence for holes on oxygen sites in the high-T c superconductors $La_{2-x}Sr_xCuO_4$ and $YBa_2Cu_3O_{7-y}$," *Physical Review B*, vol. 37, no. 10, p. 5158, 1988.

[96] N. Nücker, E. Pellegrin, P. Schweiss, J. Fink, S. Molodtsov, C. Simmons, G. Kaindl, W. Frentrup, A. Erb, and G. Müller-Vogt, "Site-specific and doping-dependent electronic structure of $YBa_2Cu_3O_x$ probed by O 1s and Cu 2p X-ray-absorption spectroscopy," *Physical Review B*, vol. 51, no. 13, p. 8529, 1995.

[97] P. Kuiper, G. Kruizinga, J. Ghijsen, M. Grioni, P. Weijs, F. De Groot, G. Sawatzky, H. Verweij, L. Feiner, and H. Petersen, "X-ray absorption study of the O 2 p hole concentration dependence on O stoichiometry in $YBa_2Cu_3O_x$," *Physical Review B*, vol. 38, no. 10, p. 6483, 1988.

[98] N. Plakida, *High-Temperature Cuprate Superconductors: Experiment, Theory, and Applications*. Springer Science & Business Media, 2010, vol. 166.

[99] Subramanian, MA and Marshall, WJ and Calvarese, TG and Sleight, AW, "Valence degeneracy in $CaCu_3Cr_4O_{12}$," *Journal of Physics and Chemistry of Solids*, vol. 64, no. 9, pp. 1569–1571, 2003.

[100] P. W. Anderson, "The resonating valence bond state in La_2CuO_4 and superconductivity," *Science*, vol. 235, no. 4793, pp. 1196–1198, 1987.

[101] F. Wang and T. Senthil, "Twisted Hubbard Model for Sr_2IrO_4: Magnetism and Possible High Temperature Superconductivity," *Phys. Rev. Lett.*, vol. 106, p. 136402, 2011.

[102] G. Kaindl, O. Strebel, A. Kolodziejczyk, W. Schäfer, R. Kiemel, S. Lösch, S. Kemmler-Sack, R. Hoppe, H. Müller, and D. Kissel, "Correlation between oxygen-hole concentration and T_c in $YBa_2Cu_3O_{7-\delta}$ from Cu-L_{III} X-ray absorption," *Physica B: Condensed Matter*, vol. 158, no. 1, pp. 446–449, 1989.

[103] Z. Zeng, M. Greenblatt, M. Subramanian, and M. Croft, "Large low-field magnetoresistance in perovskite-type $CaCu_3Mn_4O_{12}$ without double exchange," *Physical review letters*, vol. 82, no. 15, p. 3164, 1999.

[104] D. Haskel, G. Fabbris, M. Zhernenkov, P. Kong, C. Jin, G. Cao, and M. van Veenendaal, "Pressure tuning of the spin-orbit coupled ground state in Sr_2IrO_4," *Physical review letters*, vol. 109, no. 2, p. 027204, 2012.

[105] M. A. Laguna-Marco, D. Haskel, N. Souza-Neto, J. Lang, V. Krishnamurthy, S. Chikara, G. Cao, and M. van Veenendaal, "Orbital Magnetism and Spin-Orbit Effects in the Electronic Structure of $BaIrO_3$," *Physical review letters*, vol. 105, no. 21, p. 216407, 2010.

[106] A. Kolchinskaya, P. Komissinskiy, M. B. Yazdi, M. Vafaee, D. Mikhailova, N. Narayanan, H. Ehrenberg, F. Wilhelm, A. Rogalev, and L. Alff, "Magnetism and spin-orbit coupling in Ir-based double perovskites $La_{2-x}Sr_xCoIrO_6$," *Physical Review B*, vol. 85, no. 22, p. 224422, 2012.

[107] J. Clancy, N. Chen, C. Kim, W. Chen, K. Plumb, B. Jeon, T. Noh, and Y.-J. Kim, "Spin-orbit coupling in iridium-based 5 d compounds probed by x-ray absorption spectroscopy," *Physical Review B*, vol. 86, no. 19, p. 195131, 2012.

[108] S. Mukherjee, S. Sarkar, and T. Saha-Dasgupta, "First-principles study of $CaCu_3B_4O_{12}$ (B= Co, Rh, Ir)," *Journal of Materials Science*, vol. 47, no. 21, pp. 7660–7664, 2012.

[109] H. Watanaebe, T. Shirakawa, and S. Yunoki, "Theoretical study of insulating mechanism in multi-orbital Hubbard models with a large spin-orbit coupling: Is Sr_2IrO_4 a Slater insulator or a Mott insulator?" *arXiv preprint arXiv:1402.0935*, 2014.

[110] W. Witczak-Krempa, G. Chen, Y. B. Kim, and L. Balents, "Correlated quantum phenomena in the strong spin-orbit regime," *arXiv preprint arXiv:1305.2193*, 2013.

[111] G. Cao, J. Bolivar, S. McCall, J. Crow, and R. Guertin, "Weak ferromagnetism, metal-to-nonmetal transition, and negative differential resistivity in single-crystal Sr_2IrO_4," *Physical Review B*, vol. 57, no. 18, p. R11039, 1998.

[112] G. Cao, Y. Xin, C. Alexander, J. Crow, P. Schlottmann, M. Crawford, R. Harlow, and W. Marshall, "Anomalous magnetic and transport behavior in the magnetic insulator $Sr_3Ir_2O_7$," *Physical Review B*, vol. 66, no. 21, p. 214412, 2002.

[113] M. Mizumaki, T. Mizokawa, A. Agui, S. Tanaka, H. Takatsu, S. Yonezawa, and Y. Maeno, "Oxygen Hole State in A-site Ordered Perovskite $ACu_3Ru_4O_{12}$ (A= Na, Ca, and La) Probed by Resonant X-ray Emission Spectroscopy," *Journal of the Physical Society of Japan*, vol. 82, no. 2, 2013.

[114] S. Tanaka, H. Takatsu, S. Yonezawa, and Y. Maeno, "Suppression of the mass enhancement in $CaCu_3Ru_4O_{12}$," *Physical Review B*, vol. 80, no. 3, p. 035113, 2009.

[115] A. Ushakov, S. Streltsov, and D. Khomskii, "Crystal field splitting in correlated systems with negative charge-transfer gap," *Journal of Physics: Condensed Matter*, vol. 23, no. 44, p. 445601, 2011.

[116] Y.-f. Yang and D. Pines, "Emergent states in heavy-electron materials," *Proceedings of the National Academy of Sciences*, vol. 109, no. 45, pp. E3060–E3066, 2012.

[117] S. Süllow, M. Aronson, B. Rainford, and P. Haen, "Doniach phase diagram, revisited: From ferromagnet to Fermi liquid in pressurized $CeRu_2Ge_2$," *Physical review letters*, vol. 82, no. 14, p. 2963, 1999.

[118] Q. Si, "Global magnetic phase diagram and local quantum criticality in heavy fermion metals," *Physica B: Condensed Matter*, vol. 378, pp. 23–27, 2006.

[119] K. Yosida, "Magnetic properties of Cu-Mn alloys," *Physical Review*, vol. 106, no. 5, p. 893, 1957.

[120] A. Pandey, C. Mazumdar, R. Ranganathan, and S. Dattagupta, "Magnetism in ordered metallic perovskite compound $GdPd_3B_xC_{1-x}$," *Journal of Magnetism and Magnetic Materials*, vol. 321, no. 15, pp. 2311–2317, 2009.

[121] J. Feng, B. Xiao, R. Zhou, and W. Pan, "Electronic and magnetic properties of double perovskite slab-rocksalt layer rare earth strontium aluminates natural superlattice structure," *Journal of Applied Physics*, vol. 113, no. 14, p. 143907, 2013.

[122] A. Caytuero, H. Micklitz, M. M. Abd-Elmeguid, F. J. Litterst, J. A. Alonso, and E. M. Baggio-Saitovitch, "Evidence for charge disproportionation in monoclinic $EuNiO_3$ from ^{57}Fe Mössbauer spectroscopy," *Phys. Rev. B*, vol. 76, p. 193105, 2007.

[123] J. E. Lorenzo, J. L. Hodeau, L. Paolasini, S. Lefloch, J. A. Alonso, and G. Demazeau, "Resonant x-ray scattering experiments on electronic orderings in $NdNiO_3$ single crystals," *Phys. Rev. B*, vol. 71, p. 045128, 2005.

[124] V. Scagnoli, U. Staub, M. Janousch, A. M. Mulders, M. Shi, G. I. Meijer, S. Rosenkranz, S. B. Wilkins, L. Paolasini, J. Karpinski, S. M. Kazakov, and S. W. Lovesey, "Charge disproportionation and search for orbital ordering in $NdNiO_3$ by use of resonant x-ray diffraction," *Phys. Rev. B*, vol. 72, p. 155111, 2005.

[125] Y. Bodenthin, U. Staub, C. Piamonteze, M. Garcia-Fernandez, M. J. Martinez-Lope, and J. A. Alonso, "Magnetic and electronic properties of $RNiO_3$ (R = Pr, Nd, Eu, Ho and Y) perovskites studied by resonant soft x-ray magnetic powder diffraction," *Journal of Physics: Condensed Matter*, vol. 23, no. 3, p. 036002, 2011.

[126] H. Park, A. J. Millis, and C. A. Marianetti, "Site-Selective Mott Transition in Rare-Earth-Element Nickelates," *Phys. Rev. Lett.*, vol. 109, p. 156402, 2012.

[127] J.-S. Zhou, J. B. Goodenough, and B. Dabrowski, "Exchange Interaction in the Insulating Phase of $RNiO_3$," *Phys. Rev. Lett.*, vol. 95, p. 127204, 2005.

[128] G. Frand, O. Bohnke, P. Lacorre, J. Fourquet, A. Carr, B. Eid, J. Thobald, and A. Gire, "Tuning of Metal/Insulator Transition around Room Temperature of Perovskites $Sm_{1-x}Nd_xNiO_3$," *Journal of Solid State Chemistry*, vol. 120, no. 1, pp. 157 – 163, 1995.

[129] J. c. v. Chaloupka and G. Khaliullin, "Orbital Order and Possible Superconductivity in $LaNiO_3/LaMO_3$ Superlattices," *Phys. Rev. Lett.*, vol. 100, p. 016404, 2008.

[130] W. L. Lim, E. J. Moon, J. W. Freeland, D. J. Meyers, M. Kareev, J. Chakhalian, and S. Urazhdin, "Field-effect diode based on electron-induced Mott transition in $NdNiO_3$," *Applied Physics Letters*, vol. 101, no. 14, 2012.

[131] R. Scherwitzl, P. Zubko, I. G. Lezama, S. Ono, A. F. Morpurgo, G. Catalan, and J.-M. Triscone, "Electric-Field Control of the Metal-Insulator Transition in Ultrathin $NdNiO_3$ Films," *Advanced Materials*, vol. 22, no. 48, pp. 5517–5520, 2010.

[132] S. Middey, D. Meyers, M. Kareev, E. J. Moon, B. A. Gray, X. Liu, J. W. Freeland, and J. Chakhalian, "Epitaxial growth of (111)-oriented $LaAlO_3/LaNiO_3$ ultra-thin superlattices," *Applied Physics Letters*, vol. 101, no. 26, 2012.

[133] I. I. Mazin, D. I. Khomskii, R. Lengsdorf, J. A. Alonso, W. G. Marshall, R. M. Ibberson, A. Podlesnyak, M. J. Martínez-Lope, and M. M. Abd-Elmeguid, "Charge Ordering as Alternative to Jahn-Teller Distortion," *Phys. Rev. Lett.*, vol. 98, p. 176406, 2007.

[134] M. A. van Veenendaal and G. A. Sawatzky, "Doping dependence of Ni $2p$ x-ray-absorption spectra of $M_xNi_{1-x}O$ (M = Li, Na)," *Phys. Rev. B*, vol. 50, pp. 11 326–11 331, 1994.

[135] J. Liu, S. Okamoto, M. van Veenendaal, M. Kareev, B. Gray, P. Ryan, J. W. Freeland, and J. Chakhalian, "Quantum confinement of Mott electrons in ultrathin $LaNiO_3/LaAlO_3$ superlattices," *Phys. Rev. B*, vol. 83, p. 161102, 2011.

[136] S. J. May, C. R. Smith, J.-W. Kim, E. Karapetrova, A. Bhattacharya, and P. J. Ryan, "Control of octahedral rotations in $(LaNiO_3)_n/(SrMnO_3)_m$ superlattices," *Phys. Rev. B*, vol. 83, p. 153411, 2011.

[137] M. Medarde, A. Fontaine, J. L. García-Muñoz, J. Rodríguez-Carvajal, M. de Santis, M. Sacchi, G. Rossi, and P. Lacorre, "R NiO_3 perovskites (R = Pr, Nd): Nickel valence and the metal-insulator transition investigated by x-ray-absorption spectroscopy," *Phys. Rev. B*, vol. 46, pp. 14 975–14 984, 1992.

[138] X. Wang, M. J. Han, L. de' Medici, H. Park, C. A. Marianetti, and A. J. Millis, "Covalency, double-counting, and the metal-insulator phase diagram in transition metal oxides," *Phys. Rev. B*, vol. 86, p. 195136, 2012.

[139] U. Staub, G. I. Meijer, F. Fauth, R. Allenspach, J. G. Bednorz, J. Karpinski, S. M. Kazakov, L. Paolasini, and F. d'Acapito, "Direct Observation of Charge Order in an Epitaxial $NdNiO_3$ Film," *Phys. Rev. Lett.*, vol. 88, p. 126402, 2002.

[140] V. Scagnoli, U. Staub, M. Janousch, G. Meijer, L. Paolasini, F. D. Acapito, J. Bednorz, and R. Allenspach, "Charge disproportionation observed by resonant X-ray scattering at the metal-insulator transition in $NdNiO_3$," *Journal of Magnetism and Magnetic Materials*, vol. 272276, Part 1, no. 0, pp. 420 – 421, 2004.

[141] M. K. Stewart, J. Liu, M. Kareev, J. Chakhalian, and D. N. Basov, "Mott Physics near the Insulator-To-Metal Transition in $NdNiO_3$," *Phys. Rev. Lett.*, vol. 107, p. 176401, 2011.

[142] J. L. García-Muñoz, J. Rodríguez-Carvajal, and P. Lacorre, "Neutron-diffraction study of the magnetic ordering in the insulating regime of the perovskites R NiO_3 (R = Pr and Nd)," *Phys. Rev. B*, vol. 50, pp. 978–992, 1994.

[143] J. C. Slater, "Magnetic Effects and the Hartree-Fock Equation," *Phys. Rev.*, vol. 82, pp. 538–541, 1951.

[144] S. Calder, V. O. Garlea, D. F. McMorrow, M. D. Lumsden, M. B. Stone, J. C. Lang, J.-W. Kim, J. A. Schlueter, Y. G. Shi, K. Yamaura, Y. S. Sun, Y. Tsujimoto, and A. D. Christianson, "Magnetically Driven Metal-Insulator Transition in $NaOsO_3$," *Phys. Rev. Lett.*, vol. 108, p. 257209, 2012.

[145] M. Hepting, M. Minola, A. Frano, G. Cristiani, G. Logvenov, E. Schierle, M. Wu, M. Bluschke, E. Weschke, H.-U. Habermeier, E. Benckiser, M. Le Tacon, and B. Keimer, "Tunable Charge and Spin Order in $PrNiO_3$ Thin Films and Superlattices," *Phys. Rev. Lett.*, vol. 113, p. 227206, 2014.

[146] M. Wu, E. Benckiser, P. Audehm, E. Goering, P. Wochner, G. Christiani, G. Logvenov, H.-U. Habermeier, and B. Keimer, "Orbital reflectometry of $PrNiO_3/PrAlO_3$ superlattices," *Phys. Rev. B*, vol. 91, p. 195130, 2015.

[147] T. Mizokawa, D. I. Khomskii, and G. A. Sawatzky, "Spin and charge ordering in self-doped Mott insulators," *Phys. Rev. B*, vol. 61, pp. 11 263–11 266, 2000.

[148] S. Yamamoto and T. Fujiwara, "Charge and Spin Order in $RNiO_3$ (R=Nd, Y) by LSDA+U Method," *Journal of the Physical Society of Japan*, vol. 71, no. 5, pp. 1226–1229, 2002.

[149] S. Prosandeev, L. Bellaiche, and J. Íñiguez, "*Ab initio* study of the factors affecting the ground state of rare-earth nickelates," *Phys. Rev. B*, vol. 85, p. 214431, 2012.

[150] U. Staub, V. Scagnoli, A. M. Mulders, K. Katsumata, Z. Honda, H. Grimmer, M. Horisberger, and J. M. Tonnerre, "Orbital and magnetic ordering in $La_{0.5}Sr_{1.5}MnO_4$ studied by soft x-ray resonant scattering," *Phys. Rev. B*, vol. 71, p. 214421, 2005.

[151] Joaqun García and M Concepcin Sánchez and Gloria Subías and Javier Blasco, "High resolution x-ray absorption near edge structure at the Mn K edge of manganites," *Journal of Physics: Condensed Matter*, vol. 13, no. 14, p. 3229, 2001.

[152] P. Limelette, A. Georges, D. Jrome, P. Wzietek, P. Metcalf, and J. M. Honig, "Universality and Critical Behavior at the Mott Transition," *Science*, vol. 302, no. 5642, pp. 89–92, 2003.

[153] A. Haghiri-Gosnet and J. Renard, "CMR manganites: physics, thin films and devices," *Journal of Physics D: Applied Physics*, vol. 36, no. 8, p. R127, 2003.

[154] C. Ahn, J.-M. Triscone, and J. Mannhart, "Electric field effect in correlated oxide systems," *Nature*, vol. 424, no. 6952, pp. 1015–1018, 2003.

[155] S. Lee, A. Fursina, J. T. Mayo, C. T. Yavuz, V. L. Colvin, R. S. Sofin, I. V. Shvets, and D. Natelson, "Electrically driven phase transition in magnetite nanostructures," *Nature materials*, vol. 7, no. 2, pp. 130–133, 2008.

[156] K. Fujiwara, T. Hori, and H. Tanaka, "Electric-field breakdown of the insulating charge-ordered state in $LuFe_2O_4$ thin films," *Journal of Physics D: Applied Physics*, vol. 46, no. 15, p. 155108, 2013.

[157] H.-C. Wu, O. N. Mryasov, M. Abid, K. Radican, and I. V. Shvets, "Magnetization States of All-Oxide Spin Valves Controlled by Charge-orbital Ordering of Coupled Ferromagnets," *Scientific reports*, vol. 3, 2013.

[158] T. Sarkar, B. Ghosh, A. Raychaudhuri, and T. Chatterji, "Crystal structure and physical properties of half-doped manganite nanocrystals of less than 100-nm size," *Physical Review B*, vol. 77, no. 23, p. 235112, 2008.

[159] D. Kozlenko, Z. Jirak, I. Goncharenko, and B. Savenko, "Suppression of the charge ordered state in $Pr_{0.75}Na_{0.25}MnO_3$ at high pressure," *Journal of Physics: Condensed Matter*, vol. 16, no. 32, p. 5883, 2004.

[160] M. Upton, Y. Choi, J. Liu, D. Meyers, S. Middey, J. Chakhalian, J.-W. Kim, and P. J. Ryan, "Novel electronic behavior driving $NdNiO_3$ metal-insulator transition," *arXiv preprint arXiv:1412.0676*, 2014.

[161] D. Meyers, J. Liu, J. Freeland, S. Middey, M. Kareev, J. Zuo, Y.-D. Chuang, J. W. Kim, P. Ryan, and J. Chakhalian, "Selective Interface Control of Order Parameters in Complex Oxides," *arXiv preprint arXiv:1505.07451*, 2015.

[162] J. Chakhalian, J. W. Freeland, A. J. Millis, C. Panagopoulos, and J. M. Rondinelli, "*Colloquium* : Emergent properties in plane view: Strong correlations at oxide interfaces," *Rev. Mod. Phys.*, vol. 86, pp. 1189–1202, 2014.

[163] H. Hwang, Y. Iwasa, M. Kawasaki, B. Keimer, N. Nagaosa, and Y. Tokura, "Emergent phenomena at oxide interfaces," *Nature materials*, vol. 11, no. 2, pp. 103–113, 2012.

[164] E. Moon, J. Rondinelli, N. Prasai, B. Gray, M. Kareev, J. Chakhalian, and J. Cohn, "Strain-controlled band engineering and self-doping in ultrathin $LaNiO_3$ films," *Physical Review B*, vol. 85, no. 12, p. 121106, 2012.

[165] H. K. Yoo, S. I. Hyun, L. Moreschini, H.-D. Kim, Y. J. Chang, C. H. Sohn, S. Sinn, Y. S. Kim, A. Bostwick, E. Rotenberg *et al.*, "Latent instabilities in metallic $LaNiO_3$ films by strain control of Fermi-surface topology," *Scientific reports*, vol. 5, 2015.